NRC·CNRC

NRC Publications Archive
Archives des publications du CNRC

Civil Aviation Alternate Fuels Contrails and Optical Measurements Research (CAAFCOMR) – particulate emissions and contrails analysis

Brown, A. P.; Bastian, M.; Canteenwalla, P.; National Research Council Canada. Aerospace

For the publisher's version, please access the DOI link below./ Pour consulter la version de l'éditeur, utilisez le lien DOI ci-dessous.

Publisher's version / Version de l'éditeur:
https://doi.org/10.4224/40002680

Laboratory Technical Report (National Research Council Canada. Flight Research Laboratory); no. LTR-FRL-2020-0002, 2020-01-01

NRC Publications Archive Record / Notice des Archives des publications du CNRC :
https://nrc-publications.canada.ca/eng/view/object/?id=7528d222-fb25-42f0-81b0-15edab8a206f
https://publications-cnrc.canada.ca/fra/voir/objet/?id=7528d222-fb25-42f0-81b0-15edab8a206f

Access and use of this website and the material on it are subject to the Terms and Conditions set forth at
https://nrc-publications.canada.ca/eng/copyright
READ THESE TERMS AND CONDITIONS CAREFULLY BEFORE USING THIS WEBSITE.

L'accès à ce site Web et l'utilisation de son contenu sont assujettis aux conditions présentées dans le site
https://publications-cnrc.canada.ca/fra/droits
LISEZ CES CONDITIONS ATTENTIVEMENT AVANT D'UTILISER CE SITE WEB.

Questions? Contact the NRC Publications Archive team at PublicationsArchive-ArchivesPublications@nrc-cnrc.gc.ca. If you wish to email the authors directly, please see the first page of the publication for their contact information.

Vous avez des questions? Nous pouvons vous aider. Pour communiquer directement avec un auteur, consultez la première page de la revue dans laquelle son article a été publié afin de trouver ses coordonnées. Si vous n'arrivez pas à les repérer, communiquez avec nous à PublicationsArchive-ArchivesPublications@nrc-cnrc.gc.ca.

National Research Council Canada | Conseil national de recherches Canada

Canada

NRC·CNRC Aerospace

Civil Aviation Alternate Fuels Contrails and Optical Measurements Research (CAAFCOMR) – Particulate Emissions and Contrails Analysis

LTR-FRL-2020-0002

A P Brown, M Bastian, P Canteenwalla

Flight Research Laboratory

January 2020

National Research Council Canada | Conseil national de recherches Canada

Canada

Table of Contents

Classification: Unclass
Distribution: UNLIMITED

EXECUTIVE SUMMARY

As part of project CAAFCOMR, sublimating and persistent contrails have been measured inflight for petroleum and biofuels, namely Jet A1 and 100% LTPNNL ATJ-derived SPK, respectively. Comparative persistent contrails were obtained from the NRC Falcon 20 research jet, with the engines operating at Long Range Cruise (LRC) and Maximum Continuous Thrust (MCT) settings. More applicable to jet transport aircraft operations, MCT thrust used 1500 lb/hr/eng of jet fuel, and maintained the aircraft at high Mach Number, 0.84.

Contrail characteristics, consisting of integrated measurements of ice particle size, number, mass, optical thickness enabled relevant characteristics to be expressed as apparent emission indices (*i.e.*, EIn, EIm, EIo), per unit mass of jet fuel consumed. Thus, the contrail characteristics were compared between Jet A1 and 100% LTPNNL, the latter without aromatics or sulphur, and with greatly lower carbon – total hydrogen mass content was raised from 13.7% to 15.3% in the biofuel. This was therefore, a unique contrail data-set.

A power-law model was developed, which linearized contrail characteristics, as functions of air temperature, relative humidity, engine thrust state and contrail age. The linearized data had negligible scatter for LTPNNL, but noticeable scatter for Jet A1. This could have related to the high fraction of volatile particle emitted from Jet A1, whereas negligible amounts were emitted from LTPNNL.

Comparing contrails for each fuel, at -50°C air temperature, relative humidity over ice ≈100%, MCT thrust: shortly (0.03-0.05 minutes) after generation, the 100% LTPNNL contrail exhibited substantially greater (45% to possibly several hundred %) EIn, EIm, ice particle median size (median MED), EIo and local obscurity, than the Jet A1 contrail. Ice particle number concentrations were calculated to be of the order of 2000 #/cc.

Thereafter, all persistent contrails grew with increasing age. Contrail parametric growth rates for 100% LTPNNL were significantly lower, while ice particle size reduced with contrail age. Within an uncertainty band, at 3 minutes age, the 100% LTPNNL contrail parameters were between 71-96% thinner than Jet A1, in ice particle number, mass and overall optical thickness (extinction). With similar uncertainty margining, overall particulate matter emissions from LTPNNL were 72-93% lower in number, soot mass was 37-93% lower, soot particle number a mean 35% lower and soot mean size approximately 50% lower.

100% ATJ SPK contrail during changeover from Jet A1, 12th February

Classification: Unclass
Distribution: UNLIMITED

ABSTRACT

Over the period August 2019 to March 2020, the project Civil Aviation Alternate Fuels Contrails Optical Measurements Research (CAAFCOMR) was undertaken by the NRC, under sponsorship of Environment & Climate Change Canada, Transport Canada, LanzaTech and the NRC. The NRC Falcon undertook flight operations on Jet A1 and unblended LTPNNL ATJ-derived SPK bio-jet fuels. High altitude cruising flight contrails at typical air transport cruise Mach Numbers of 0.75-0.84 were sought for each flight, with engines operating at maximum continuous thrust (MCT). In cruise, young contrails and emissions data was measured by the NRC CT-133 research aircraft, out to 1.2 minutes age. This was sufficient length to identify the state of contrails, persistent or sublimating, as dictated by background atmospheric conditions – both states were encountered upon CAAFCOMR flights. CT-133 measurements consisted of contrail optical thickness, ice particle size and number, particulate and gaseous emissions from the Falcon in cruise.

The project was a follow-on from project CAAFCEB, for which the jet fuels were Jet A1, JP-5 and 92% LTPNNL blended with 8% petroleum-derived aromatics. The objectives of CAAFCOMR were the measurement of contrails under a contemporary limit-state (100%, no sulphur nor aromatics and maximum hydrogen content, 15.3%) of biofuel technology and to obtain contrail optical thickness measurement comparisons.

All contrails were generated by the NRC Falcon, with the same engines. Individual engine emissions and ice particle formation were not measured. Rather, the wake and contrail cross-sections were measured holistically, over the full vertical and lateral extents. A number of lateral/vertical transects, typically nine, were concatenated in the line-of-flight (contrail axis) direction to form re-constructed contrails, integration of which enabled the autonomous derivation of contrail ice particle number Apparent Emission Indices (EIn). In addition and for the first time for NRC contrail flight research, CO_2 concentration was used as a species intermediary, for the derivation of contrail ice particle EIn. Thus, the cross-accuracy of the two methods were inter-compared. The mean difference between methods was approximately 20%.

Three ATJ SPK//Jet A1 flights were conducted, with one sublimating contrail and two persistent contrails achieved for each fuel.

The 100% ATJ SPK persistent contrails were generated at significantly greater initial growth rates than those for Jet A1, as sensed by the FSSP-100 for >0.5 μm ice particle sizes, in ice-mass EIm, overall optical depth EIo, zenithal optical obscurity, and median ice particle size, whilst ice particle number EIn, were similar, at a contrail age of approximately 0.05 minutes.

Thereafter the ATJ SPK >0.5 μm contrails grew at slow temporal rates, with the ice particle size reducing as EIn increased slowly. Jet A1 contrail >0.5 μm ice particle size, EIn, EIm, EIo, and zenithal obscurity all grew at greater rates, so that by an extrapolated contrail age of three minutes, the ATJ SPK contrails were 71-96% thinner in EIn and EIo, zenithal obscurity was 20-50% lower and median ice particle size 0-30% lower.

With similar uncertainty margining, overall PM emissions from ATJ SPK *c.f.* with Jet A1 were 72-93% lower in number. nvPM, *i.e.* soot, mass was 37-93% lower, soot particle number a mean 35% lower and soot mean size approximately 50% lower.

Classification: Unclass
Distribution: UNLIMITED

ABBREVIATIONS

AEC_{ZY}	Apparent emission index of the lateral integrand of contrail optical depth (OD), m/kg of fuel burned
AEIm	Apparent emission index of contrail ice particle mass (assuming sphericity), µg/kg of fuel burned
AEIn	Apparent emission index of contrail ice particle number, #/kg of fuel burned
ATJ	Alcohol-to-jet derived SPK biofuel
BC	Black carbon particles (soot)
CAAFCEB	ECCC/TC/NRC project Civil Aviation Alternate Fuel Contrails and Emissions at high-Blend Biofuel (present project)
CEP	Cloud Extinction Probe (providing a measurement of optical thickness)
c.f.	*conferatu*, Latin, meaning 'compared with'
CN	Condensation nuclei, >22 nm calibrated cut-off size
CO_2	Carbon dioxide – concentration has been used as an intermediary for derivation of localised Emission Indices of contrail characteristics
CPC	Condensation particle counter
Cs	Cirro-stratus, high altitude stratified cloud
DAS	Data acquisition system
EDR	Eddy dissipation rate, a representative integrand over spatial-frequency of the atmospheric turbulence power spectra
EGT	Exhaust gas temperature of the FA20 CF-700 engines
EIm	Emission Index by mass per kg fuel burned
EIn	Number Emission index by number per kg of fuel burned
EIo	Contrail optical thickness Emission Index, whereupon the extinction coefficient is integrated (per m in the x-dir) over the volume of the complete cross-section of the contrail, that has been re-constructed from eight lateral & vertical traverses
EPR	Engine pressure ratio (a measure of operating thrust)
FA20	NRC Falcon 20 research jet
FF	FA20 engine fuel-flow, lb/hr/eng, related to a fuel SG of 0.81.
FIRNS	FRL inertial reference and navigations system (integrated HG1700 IMU, Novatel GPS and DRP system)
FL	Flight level – pressure altitude, referenced to 1013.25 hPa.
FSSP-100	Forward scattering spectrometric probe, 100 series (minimum sensed particle size, > 0.5 µm)
GFS	Global Forecasting System NWP
GW	Global warming
HAARC	NRC High altitude atmospheric research capability
LoF	Line of flight direction (*i.e.*, parallel to the contrail axis)
LRC	Long range cruise engine thrust setting (EGT 680°C at high altitude), FA20/CF-700 Mach Number 0.72.
LTPNNL	LanzaTech ethanol-derived ATJ SPK
LVW	Lower viscous wake (wake regime below the TWV)
M	Mach Number
MCT	Maximum continuous thrust engine power (EGT 724°C at high altitude), FA20/CF-700, resultant Mach Number 0.84.

Classification: Unclass
Distribution: UNLIMITED

MED	Median effective diameter (50^{th} percentile of the cumulative volumetric spectrum) of each size-number ice particle spectrum of the FSSP-100 measurements, recorded at 10 spectra per second frequency.
NRC	National Research Council of Canada
N_1	Engine gas generator rotational speed (%)
nv	Non-volatile
nvPM	Non-volatile particulate matter (such as black carbon)
NWP	Numerical weather model
OD	Contrail optical thickness or depth, the vertical integrand of contrail extinction coefficients (km^{-1}); thus, OD is non-dimensional.
P_S	Atmospheric static air pressure
P_T	Atmospheric total air temperature
RF	Radiation forcing (by cloud processes)
RH	Relative humidity
RHi	RH over ice
SG	Specific gravity
SNR	Signal-to-noise ratio
TAS	True airspeed (m/s)
TAT	Total air temperature (sensing probe), (°C)
TKE	Turbulent kinetic energy, $\sqrt{(u'^2+v'^2+w'^2)}$
TOPC	Top of climb
T_S	Static air temperature (°C)
TWV	Trailing wake vortex
UJW	Upper jet wake; generally the UJW in cross-sectional shape is a '**T**', the lateral being the UJW crown, the vertical being the UJW stem, and the foot being the TWV region.
vPM	Volatile particulate matter
WVap	Water vapour
u'	Unsteady wind component (notably, trailing vortex-induced) in the x direction
v'	Unsteady wind component in the y direction
w'	Unsteady wind component in the z direction
[x]	Line-of-flight axis direction (upstream is positive)
[y]	Lateral direction (to the right is positive, looking upstream)
[z]	Normal direction (upwards is positive)
α_{DP}	α (incidence or angle-of-attack) probe differential pressure
β	Extinction coefficient (km^{-1}), a measure of the contrail optical thickness.

Classification: Unclass
Distribution: UNLIMITED

1. INTRODUCTION

1.1 Overview

1.1.1 The NRC has undertaken flight measurements of Heavy Category jet transport aircraft emissions, whilst cruising in the Upper Troposphere Lower Stratosphere (UTLS), since late 2012, covering a variety of older and contemporary aircraft types of >136 metric tonne in weight. The research has concentrated upon PM aerosol emissions from Jet A/A1 and a variety of biofuel types, blended at 50-100%, the latter burnt by the NRC Falcon research jet.

1.1.2 Since 2014, the NRC CT-133 HAARC has been conducted flight research into contrails generated by Heavy Category jets, including the B777, 763, A380 and NASA DC-8 **[1]**, and Medium Category jets, including Air Canada A320 jet contrails and those generated by Falcon 20 jets of the NRC, NASA and DLR. Of these, the NASA DC8, Air Canada A320 and NRC Falcon 20 (FA-20) emissions measurements have emphasised biofuel flight research. Emissions from biofuels of HEFA-blends (43%, 50% and 60% with Jet A1, 50% with Jet A), CHJ (100% ARA ReadiJet), HEFA SPK (Shell Virent), ATJ SPK (92% LTPNNL, 8% Solvesso 150 ND aromatics) and presently 100% ATJ SPK (no aromatics) have been measured.

1.1.3 Contrails generated by the NASA DC-8 on 50% HEFA-blend, Air Canada A320/321 on 43% HEFA-blend and the NRC Falcon on 60% HEFA-blend, HEFA SPK (Shell Virent with synthetic aromatics), ATJ (92% LTPNNL with 8% aromatics, 150 ND) and presently 100% LTPNNL (no aromatics) have been measured.

1.2 Background

1.2.1 For young contrails (herein defined as contrails of an age range of 0-5 minutes), covering the contrail states from generation to sublimation, or to persistence (defined as a non-negative lapse-rate of apparent EIn with contrail length), characteristics are dominated by trailing vortices, which induce extremely high magnitudes and gradients of vorticity, in comparison to any background atmospheric vorticity state **[2]**. These dominate cross-plane ([lateral vertical] plane) conditions, in studying the nature and characteristics of young contrails, as they transition to persistent, or sublimating, contrails.

1.2.2 Therefore, NRC data analysis of flight emissions and contrails has been centred upon the contrail and emissions cross-planes, by holistically re-constructing this cross-plane from a number (generally nine, occasionally reduced to six) of transects obtained in the line-of-flight direction **[3]**. This spatiotemporal analytical reduction methodology has the benefit of being autonomous, thereby obviating any dependency upon an intermediate species, nor upon similarity between plumes of different phase and species.

1.2.3 The NRC contrail data obtained by the NRC CT-133, from the NASA DC-8 contrail, in NASA ACCESS II, indicated **[1]** a reduction in contrail ice particle number production, using 50% HEFA-blend (with a low-sulphur Jet A fuel) *c.f.* low-sulphur Jet A. However, the DC-8 contrails were wake vortex type, dominated by the DC-8 trailing vortex core condensate. Little UJW condensate was present, although UJW contrails from the DC-8 have been previously observed by NASA. Thus, the NRC ACCESS II conclusion on the reduction of contrail ice particle number by HEFA-blend required extension to UJW contrails. In particular, the St Lawrence Seaway region of south-eastern Canada is dominated by the North American Jetstream. Within this area, UJW contrails are prevalent. The

Classification: Unclass
Distribution: UNLIMITED

GARDN CAAFCER project measured contrails from Air Canada A320/321 jets in commercial service, operating on Jet A1 and on 43% HEFA-blend. The contrails were dominated by vertical development, due to the strong entrainment effect from closely-spaced trailing vortices [4]. Persistent contrails on these flights included UJW-crown lateral spread, of cirro-cumuliform type by five minutes age. The project demonstrated a reduction in contrail ice particle number for these UJW contrails **[4]**.

1.2.4 The potentially-beneficial effects of reducing the thickness of contrails relate to solar radiation entrapment by persistent contrails, following their transformation to cirrus and lateral spread. The resultant radiation forcing is considered to be a global-warming contributor **[5]**. Assessment of the magnitude of this potential benefit requires the measurement of the optical effects of contrail spectra, through the full lifetime of formation and persistence, and the effects upon optical characteristics by the widest range of fuel properties, including new generation bio-jet fuels.

1.2.5 The CAAFCEB project was conducted to provide data for a wide range of hydrogen mass content in jet fuel – by using a JP-5 (low hydrogen content, conversely high carbon mass content) Jet A1 and LTPNNL ethanol-based ATJ SPK bio-jet (of high hydrogen content). Contrail ice particle data was further analysed **[5]**, in CAAFCEB, to include contrail optical parameters, in accordance with ECCC methodology [6]. Like ice particle AEIn and nvPM EIn, contrail optical thickness reduced substantially with high-blend ATJ SPK.

1.2.6 Against this background, CAAFCOMR was undertaken to research contrail properties from biofuel of the highest hydrogen content range under contemporary biofuel technology, including optical properties. For this, 100% LTPNNL fuel with neither aromatics nor sulphur content (<1 ppm), was used to power the NRC FA20 engines in normal-rated thrust high altitude cruise, for the generation of emissions and contrails. Measurements were undertaken on a back-to-back basis, using JetA1 in both engines and then transferring to 100% LTPNNL in both engines. It has been assumed that contrail formation was not dependent to any significant effect, upon the sequence of fuel burn, i.e. Jet A1 then LTPNNL, or *vice versa*, although lower-order effects were likely, such as scrubbing of pre-deposited wall particulates, during burn of the cleaner LTPNNL fuel (a conservative, or pessimistic, effect, when comparing the particulate matter emission differences). Rather the sequence was chosen, in order to verify the contrail extent using Jet A1, before switching to the burn-time-limited bio-jet fuel.

2. EXPERIMENTAL DETAILS

2.1 CT-133 Aircraft and sensor details

2.1.1 The NRC CT-133 is shown with sensors, in the HAARC CAAFCOMR configuration, in Figure 1. The aircraft sensor fit has been progressively upgraded since initial commissioning of the CT-133 as HAARC, in late 2011.

2.1.2 For CAAFCOMR, *c.f.* the previous contrail project, CAAFCEB, the following instrumentation changes were made:

- a Picarro fast response CO_2 and water vapour sensor was installed in the starboard pod; the Thermo 42I NOx analyser was removed;

Classification: Unclass
Distribution: UNLIMITED

- the 3776 CPC was replaced by the TSI 3790 CPC of calibrated cur-off size 19nm (*i.e.* reliably sensing particles of size ≥19 nm), **[19]**, and counting efficiency 0.855; the volatile denuder was retained (calibrated cut-off size 17 nm and through-flow counting efficiency 0.588); the 3790 CPC installation suffered excessive loss of counting sensitivity at high altitude, that was not resolved successfully during the project, for which unit disassembly was needed;
- the ECCC Cloud Extinction Probe (CEP) **[6]** was installed in the tailcone of the starboard pod, with a retro-reflector installed in the starboard wingtip fuel tank attachment plenum; thus the optical path was from the red-light transmitter lens, through a cut-out in the tailcone skin, to the retro-reflector at the tiptank and return; the CEP output signal was 0-6 Vdc analogue, which was converted and sampled digitally at 600 Hz, the same rate as the inertial and air data; and
- an ice denuder was added to the LII300 air sampling line, in order to vaporize ice particles prior to the optical measurement chamber.

2.1.3 At high altitude, the Picarro water vapour (WVap) measurement sensitivity reduced. The Licor 840A WVap signal remained viable, correlated with the Picarro measurement at low altitude and with Maniwaki weather balloon soundings at high altitude, in order to correct for the combination of 840A zero-uncertainty (the uncertainty was associated with sampling air temperature, which reduced through the 840A at high altitude; sensor repeatability accuracy was ±2%).

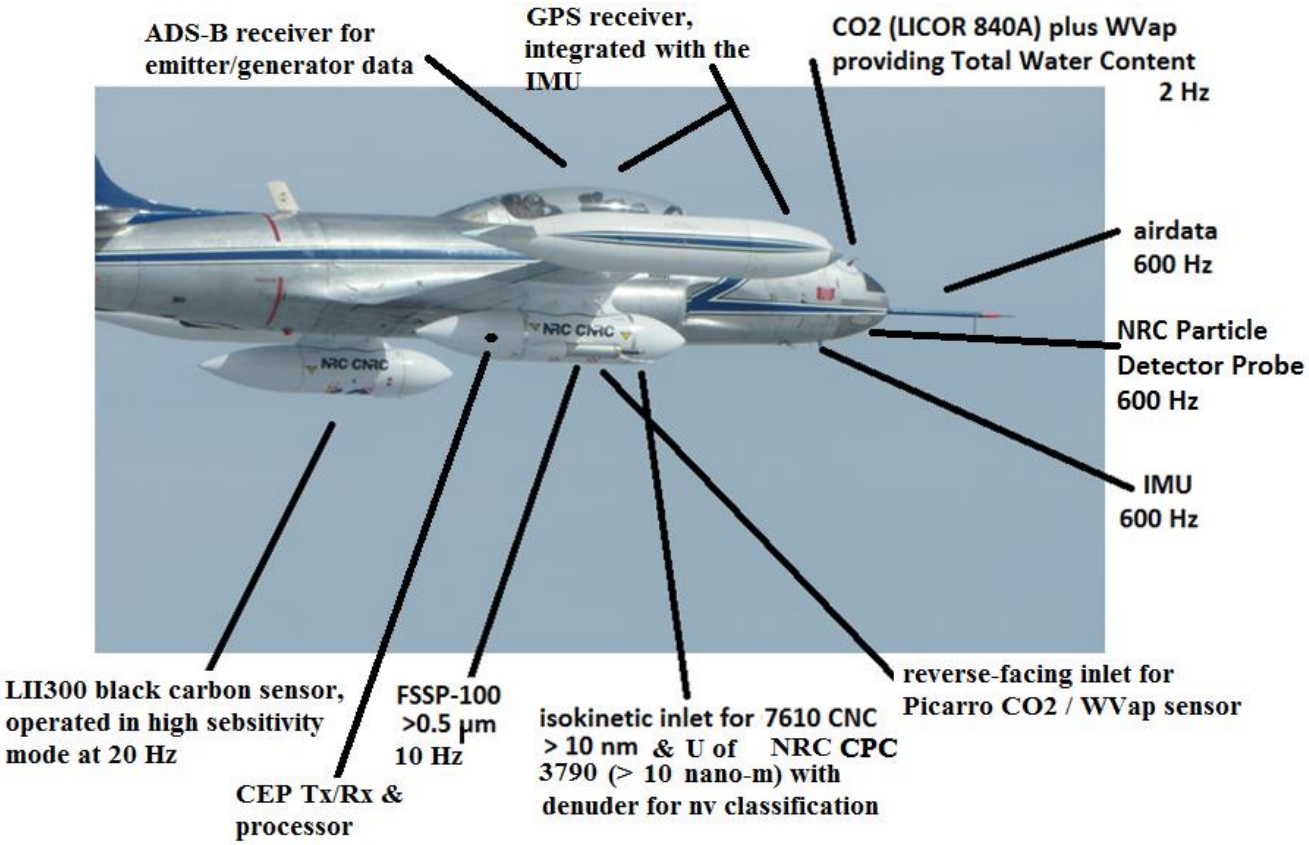

Figure 1 NRC CT-133 research jet, equipped with contrail and emissions measurement sensors for the CAAFCOMR project configuration.

Classification: Unclass
Distribution: UNLIMITED

2.1.4 The ECCC FSSP-100 ice particle sensor was mounted on the starboard underwing pod, and co-located with the isokinetic probe supplying the CN and CPC sensors. The FSSP-100 optical path arms were equipped with Korolev Tips, deflecting shattered ice particles outside the laser-sensing volume of the open-flow path. It was calibrated to sense accurately in the first bin size, ≥0.5µm. Nevertheless, residual uncertainty related principally to measurement sensitivity in the lowest size bin.

2.1.5 As noted above, for CAAFCOMR the LII300, used for the measurement of BC, had been modified by the addition of an ice denuder, for the following reason. In contrails on project CAAFCEB, the LII300 appeared to be at times, sensitive to the presence of ice particles. This effect has been observed as an apparent reduction in BC mass concentration and loss of spatial coherence. A possible physical mechanism could be reflective scattering of incident laser energy, to the point of inhibiting atomic resonance of carbon atoms and thus inhibiting incandescence and vaporization. The ice denuder heated the sampled air to 80°C, upstream of the LII300 optical chamber, thereby vaporizing contrail ice particles at high altitude (contrail formation occurred at air pressures of <30 kPa), so that all nucleating BC particles would be vaporized, thereby contributing to the bulk measurement of BC.

2.1.6 Sensors are described in Table 1. The CPC was coupled with a denuder for non-volatile classification of ultrafine particles. By valve switching, the denuder could be bypassed (providing a measure of total ultra-fines) or it could be switched in-line, upstream of the CPC and thus enabling a measure of non-volatiles. Typically, the denuder was sequentially operated in bypass for two minutes, thence in-line for approximately the same period.

Table 1 – NRC CT-133 emissions and contrails measurement instrumentation

Sensor location	Sensor	Description and sensor performance	Acquisition rate
Port wing			
Wing surface, outboard	Wing glove, 24 surface pressure sensors	Measures high-rate unsteady aerodynamic forces, for example, during the penetration of trailing vortex cores	600 Hz or 1200 Hz
Under-wing HAARC pod	LII 300 BC sensor with ice denuder	Measuring BC volumetric concentration of mass; the ice denuder operated at all times	20 Hz
Starboard wing			
Under-wing HAARC pod	CN 7610 aerosol counter	condensation nuclei counter, calibrated cut-off size 22 nm and sea-level counting efficiency 0.931 **[19]** (for consistency with *a priori* data, **[1]-[4]**, the possible 7% under-read at high altitude was not corrected for inter-comparative fuel data, but remained an uncertainty in absolute values, for each fuel type.	10 Hz
	CPC 3790 aerosol counter	aerosol counter, of calibrated cut-off size 19 nm and sea level counting efficiency 0.855 **[19]**; sensor worked accurately at low altitude, but de-sensitised at high altitude by 2 orders of magnitude,	10 Hz

Classification: Unclass
Distribution: UNLIMITED

	Denuder	non-volatile (*nv*) particle path for CPC 3790 (vaporized volatile particles), for which the sea-level calibrated cut-off size was 17 nm, with counting efficiency 0.588 **[19]**, – with the denuder bypassed, the CPC 3790 counted volatile and *nv* particles.	N/A
	Picarro	CO_2 and WVap analyser; 45 minutes ground operating time was required for stabilisation and locked P,T functioning throughout high altitude ops.	2 Hz
	FSSP-100	Forward-scattering spectrometric probe, measuring particles > 0.5 μm in size – in the contrail environment, ice particles; bin counts were corrected for coincidence using the probe Activity Count.	10 Hz
	CEP	Light-path was from pod to tip-tank, a distance of 8 feet, and return. Operated continuously, measuring the optical thickness of contrails, which varied predominantly with ice particle and BC particle light absorption, scattering and reflection. Retro-reflecting mirror potentially suffered frosting in contrail flight, degrading independent, optical thickness readings.	600 Hz
Nose			
Upper nose	Licor 840A	CO_2 and water vapour measurement	2 Hz
Left side	TAT probe	TAT, responsive to an upper cut-off of approx. 5 Hz	600 Hz
Nose tip	Air data boom	Atmospheric pressure and temperature, pitot pressure; incidence and sideslip angles.	600 Hz
Internal	FIRNS	Inertial reference & navigation system, based upon the HG1700 IMU, Kalman-filter blended with GPS	600 Hz
Left side	Particle detector probe (PDP)	Measuring ice particle concentration, non-operational for 12th February flight	20 Hz
Cockpit			
Canopy-bow mount	Novatel DGPS receiver	GPS	600 Hz
	Stratux ADS-B receiver	ADS-B IN from target aircraft	ADS-B rate
	Rasp Pi computer	Processing NRC Wake Turbulence display	2 Hz
	Monitoring & controlling computer	Data acquisition control; pod mass-flow control.	600 Hz
	DAS	Central data acquisition system for all state & sensor parameters	600 Hz
Forward windscreen	Line-of-flight video camera	Recording line of flight view (visual spectrum), in particular the existence & optical nature of contrail conditions, in the visible spectrum.	60 frames per second

Classification: Unclass
Distribution: UNLIMITED

2.2 Falcon aircraft and sensor details

2.2.1 The NRC Falcon was instrumented for acquiring inertia, air and engine data, the details of which are presented in Table 2.

Table 2 – NRC Falcon, emitting and contrail generating research jet.

Parameter group	Sensor description	Parameters	Acquisition rate
Inertial data	IMU located underfloor, mid-cabin	LAT, LON, GPS HGT, inertial velocities, Euler angles & angular rates, linear accelerations	60 Hz
Airdata	Pitot tube, static ports & TAT probe on aircraft fore-fuselage sides; FADS 4-hole surface pressure sensor system on aircraft nose	Ps, Pt, TAT, air velocity magnitude & direction; pressure altitude; pressure altitude. Derived parameters of TAS, Ts and M.	60 Hz
Engine data	High impedance pick-off circuits on aircraft engine thrust state sensors, both engines	Fuel-flow (in lb/hr, referred to Jet A1 fuel density) N1, fan speed N2, EPR, EGT	

2.3 Flight details summary

2.3.1 Flight details are contained in Table 3. It is seen that the flight sequence was divided between airworthiness flight test (AWFT) for the new CEP installation, CEP functionality and biofuel-contrail flights.

2.3.2 The developmental flight effort was protracted, due to loss of CEP functionality caused by starboard HAARC pod rotation (combined sway and roll) inflight. This resulted in a significant ground test and investigation, followed by several proofing flight tests.

2.3.3 This development included ground measurement of pod sway-brace set loads, using compression pads. This measurement validated structural design loads invoked for the HAARC pod installations. The testing also determined a reliable sway-brace torqueing procedure, whereby the sway-braces were to be incrementally torqued in 5 lbf steps from surface contact through to final torque values of 50 lbf. This procedure was thereafter promulgated in the Continued Airworthiness Instructions for the HAARC pods.

2.3.4 Thereafter, a series of low and high altitude CEP functionality flights were conducted, to validate CEP performance in light to moderate optical thickness cloud and in a ground vegetation burn-off smoke plume. 100 % biofuel, no-aromatics contrail flights were conducted on the 20th and 29th August 2019, in sublimating and persistent contrail conditions, respectively. The CEP processor circuit breaker failed during the start-up sequence of the 29th August flight, such that no CEP data was obtained on this flight. On the other contrail flights, CEP signal unsteadiness was large. It is considered probable that the retro-reflector mirror suffered frosting in the thick contrail environment (which had localised temperature elevations of several degrees, frost-inducing), so that it would benefit from a mirror heater installation, to eliminate the occurrence, for future flights, in order to obtain additional optical thickness data to that derived from FSSP ice particle size and number density spectral data.

Classification: Unclass
Distribution: UNLIMITED

Table 3 – CAAFCOMR flight details

Date	Flight Sequence	Comments
25 Jun 19	CEP airworthiness flight test (AWFT)	Partial clearance to 200 KIAS; HAARC pod movement occurred, with loss of alignment
26 Jun 19		300 KIAS and M0.7 expansion completed, after CEP re-alignment; HAARC pod movement re-occurred.
29 Jun 19	CEP functionality	HAARC pod movement re-occurred; this flight was followed by an extensive 3 week period of ground testing to validate pod sway-brace functioning; finally, sway-brace loads were measured using compression pads; a new incremental torqueing procedure was established (torque incremented diagonally, in 5 lbf steps from contact to 50 lbf); this method resulted in the retention of torque without any HAARC pod shifting inflight.
17 Jul 19		Low-altitude functionality stratocumulus cloud
22 Jul 19		Low-altitude functionality stratocumulus & cumulus cloud; burn-off smoke plume CEP characterisation
25 Jul 19		High altitude background (thin) cirrus cloud characterisation
30 Jul 19		As above

Date	Fuel sequence & contrail conditions			Background atmosphere
20 Aug 19	(1) Jet Al	M 0.6	Dry air climb; TOPC contrail measured at a length of <3 km	Intermediate RHi, c.60%, air temperature -48°C.
	(2) Jet A1	M 0.72	Accelerating & operating near MCT; sublimating contrail, length 8 km;	
	(3) LTPNNL 100%	M 0.72	Contrail visibly sublimated.	
29 Aug 19	(1) JetA1	M 0.75	MCT engine thrust; persistent contrail	A 40 km pool of high RHi, c.80%; air temperature similar, -48°C. No cloud at the start of contrails; wide area contrail cirrus at the completion
	(2) LTPNNL	M 0.75	MCT; persistent contrail.	
Annual maintenance period, September 2019 – January 2020 incl.				
Date	**Fuel sequence & contrail conditions (continued)**			**Background atmosphere**
04 Feb 20	NA	NA	Post-maintenance flight	Sampled Anthropogenic cirrus at 32-34,000 ft, from previous enroute jet transits.
12 Feb 20	(1) Jet A1	M0.7 to M0.82	MCT, Jet A1initially sublimated, then re-generated to a persistent contrail	Poor NWP forecast; localized, sub-regional high RH pooling.
	(2) LTPNNL	M0.84	MCT, growing persistent contrail	RH higher for the LTPNNL contrail.

Classification: Unclass
Distribution: UNLIMITED

2.3.5 On the 29th August and 12th February flights, engine fuel-flow oscillation occurred at lower thrust settings, whilst operating on 100% ATJ SPK LTPNNL biofuel, together with low fuel-pressure fluctuations. Oscillations were more noticeable on the 29th August flight, whereupon the SPK feed to the engines was discontinued, the SPK quarantined and off-loaded post-flight.

2.3.6 Such fuel-flow and fuel pressure instability constituted a flight hazard. Ground investigation and testing confirmed ATJ SPK specification compliance, without any change in fuel properties **[11]** but revealed the presence of free water in the starboard feeder tank of the Falcon and in one of the partially-used fuel drums. The drums were constructed of stainless steel. It was determined that a sealing failure of the bottom rim had occurred (from which fuel weeping was witnessed) with the likely consequence that water ingress had occurred at some point during shipment. However, subsequent throttle sweeps executed at the end of LTPNNL contrail generation resulted in similar low fuel pressure instability, seemingly exhibiting the characteristics, as before, possibly of cavitation or pump vane stall type of behaviour.

2.4 Weather forecasting

2.4.1 Numerical weather model predictions (NWP) of UTLS air temperature and WVap mass fraction were used for flight decision making. NWP accuracy was assessed by inflight occurrences of cirrus cloud and contrails. In this regard, the GFS NWP has been observed to be accurate in spring and summertime conditions, but over-predicted WVap content in winter, 2-300 km to the north of Ottawa, Ontario. On the other hand the regional RAP NWP under-predicted WVap content in this area.

2.4.2 Contrail conditions were neither predictable nor consistent in this region over the summertime months. Thus, this time of year was generally to be avoided for such flight research; however, project constraints necessitated summertime execution.

2.5 Flight and atmospheric details

2.5.1 Table 3 includes a summary of encountered atmospheric conditions and generated contrails. For each of the two August flights, the NWP forecast of contrails were unpredictable. The RHi conditions of the 20th August were over-predicted, whilst for the 29th August they were under-predicted. This resulted in the occurrence of sublimating and persistent contrails, respectively.

2.6 Flight profile descriptions

2.6.1 The CAAFCOMR flight profile flown by the FA20 / CT-133 pair of aircraft, generally consisted of line-astern operation. During climb, the CT-133 flew behind the FA20, on the same heading; low amplitude weaving was conducted, to cross the emissions plume (in clear air) or the contrail (once contrail conditions were encountered) in a continuous series of lateral and vertical traverses, the extremities of each traverse were in background atmospheric conditions.

2.6.2 When the optimum contrail formation altitude was determined, the FA20 accelerated to the M0.72-0.85 range (the Mach Number used depended upon the lateral extent of the high RHi region), using nominally MCT. Racetrack patterns were flown.

2.6.3 The lateral extents of the racetracks were relatively small, sized for the following reasons: (a) approximately 20 Nm long on the 20th August flight, due to a relatively-small

high RHi region, in sublimating contrail conditions, and (b) approximately 30 Nm long on the 29th August flight, due to the rapid transformation and spread of contrail cirrus, obscuring the Falcon aircraft and interfering with the operational efficiency of racetrack re-join procedures.

2.6.4 Contrail lengths varied from 500 to 4,500 m, as depicted in the LAT-LON plan-form and in-trail distance plots of Figure 2, for the 20th August flight. At FA20 flight speed, this was a contrail age range from 2.5 to 22 seconds.

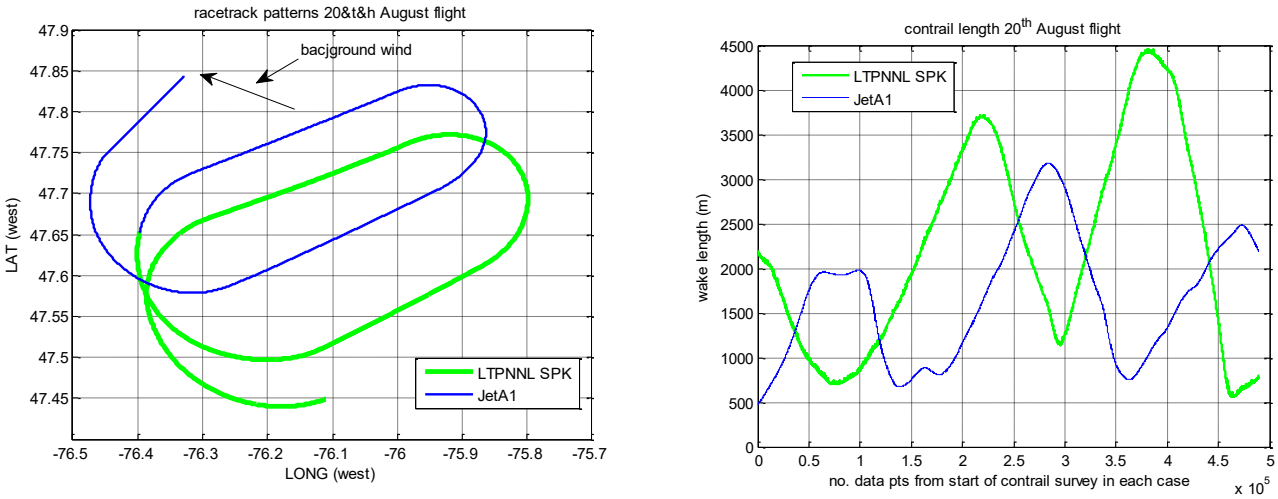

Figure 2 CAAFCOMR flight, 20th August 2019: *left*, plan-form profile of racetrack; *right*, contrail lengths for each fuel, JetA1 and LTPNNL SPK.

2.7 Methods of analyses

2.7.1 Two methods of contrail data analysis were used for the CAAFCOMR data analysis. In addition to the holistic plume cross-sectional re-construction methodology employed since initial NRC CT-133 emissions measurements (an autonomous method that does not use an intermediate species concentration, such as that of CO_2) **[2]**, the CO_2-comparison method was used for the derivation of contrail ice particle number EIn, whereby inter-comparison between ice particle number density and CO_2 concentration was used to derive EIn for the former. Employment of the additional method was largely driven by the failure of CN sensor recordings on the flight of the 20th August, induced by an inflight pneumatic leak). The CO_2 sensors had repeatability tolerances of $\pm$2%, equivalent to an elevated concentration of approximately 8-10 ppm. In the emission plumes, CO_2 concentration lessened rapidly, depleting to these values by wake lengths of approximately 3 nautical miles. Accordingly the accuracy of EIn derivation could be expected to reduce significantly with increasing wake length.

3. FLIGHT RESULTS & DISCUSSION

3.1 Falcon engine operating conditions, Jet A1 and SPK

3.1.1 The Falcon was essentially operated in two experimental conditions, one relating to in-trail climb (M0.4-0.6, FL050-320), and the other relating to high-speed cruise (M0.6-0.84) within the altitude FL300-340). Once established in contrail-height cruise conditions, the throttles were set to the MCT position, for Mach acceleration. Once the CT-133 had encountered visible contrail sublimation conditions, the CT-133 commanded a race-track turn

Classification: Unclass
Distribution: UNLIMITED

reversal. During the turns, throttle level angle (TLA) was reduced somewhat, to reduce SPK fuel-burn (no contrail measurements were taken during the turns, rather the CT-133 undertook a rejoin to the close in-trail position), then on a straight track MCT was re-established and maintained.

3.1.2 Maps of engine thrust (represented by the EPR parameter) and fuel-flow (FF) (for Jet A1 density, hence a volumetric flow-rate comparison) against varying TLA whilst conducting the above flight patterns (at 37,000 feet height and 220 K air temperature) on the 20th August 2019 flight, are shown in Figure 3. It is seen that the steady-state MCT EPR and FF are similar between Jet A1 and LTPNNL fuels, implying similar engine thrusts at the same steady-state volumetric flow-rates of fuel.

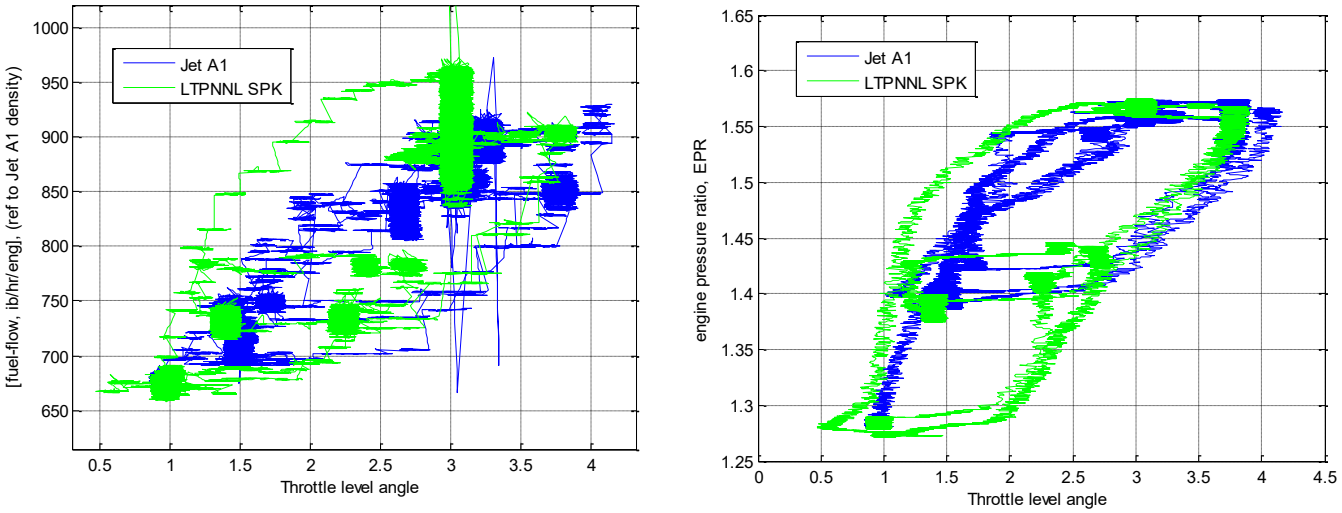

Figure 3 – 20th August 2019 flight, 37,000 feet height and 220 K air temperature: plotted against throttle level angle, Falcon engine data for Jet A1 (*blue*) and LTPNNL ATJ SPK (*green*): *left*, fuel-flow, ref. Jet A1 density (hence, a volumetric flow comparison), *right*, EPR.

3.1.3 The EPR~TLA plots highlight the significant mechanical hysteresis of the engine throttling system (*i.e.*, cables connected from the throttles to the engine fuel control units (FCU) at the engines).The hysteresis is broadened 10-20% for the LTPNNL fuel. However, the FCU had gradated controls, which should be reset to actual fuel density. This could not be done inflight, and it was possible that the difference in dynamic effects was related to the non-correspondence of FCU fuel density and that of the fuel used at any particular time (in particular LTPNNL fuel). In summary, whilst Figure 3 illustrates acceptable engine behaviour during TLA changes, the flight technique is not suitable for quantifying any differences in dynamics because of the FCU density re-set requirement, which was not possible to undertake within the scope of this experiment.

3.1.4 Engine gas generator performances and resultant aircraft cruise Mach Number performances between Jet A1 and 100% LTPNNL SPK are compared in Figure 4 (Long Range Cruise, LRC) and Figure 5 (Max Mach Cruise with MCT thrust, EGT 724 °C). For LRC, EPR values at stable Mach Number, for an EGT of 700°C, were 1.64 and 1.65 for Jet A1 and LTPNNL, respectively; Mach Numbers were similar between fuels, 0.73 (not fully stabilised for LTPNNL).

Classification: Unclass
Distribution: UNLIMITED

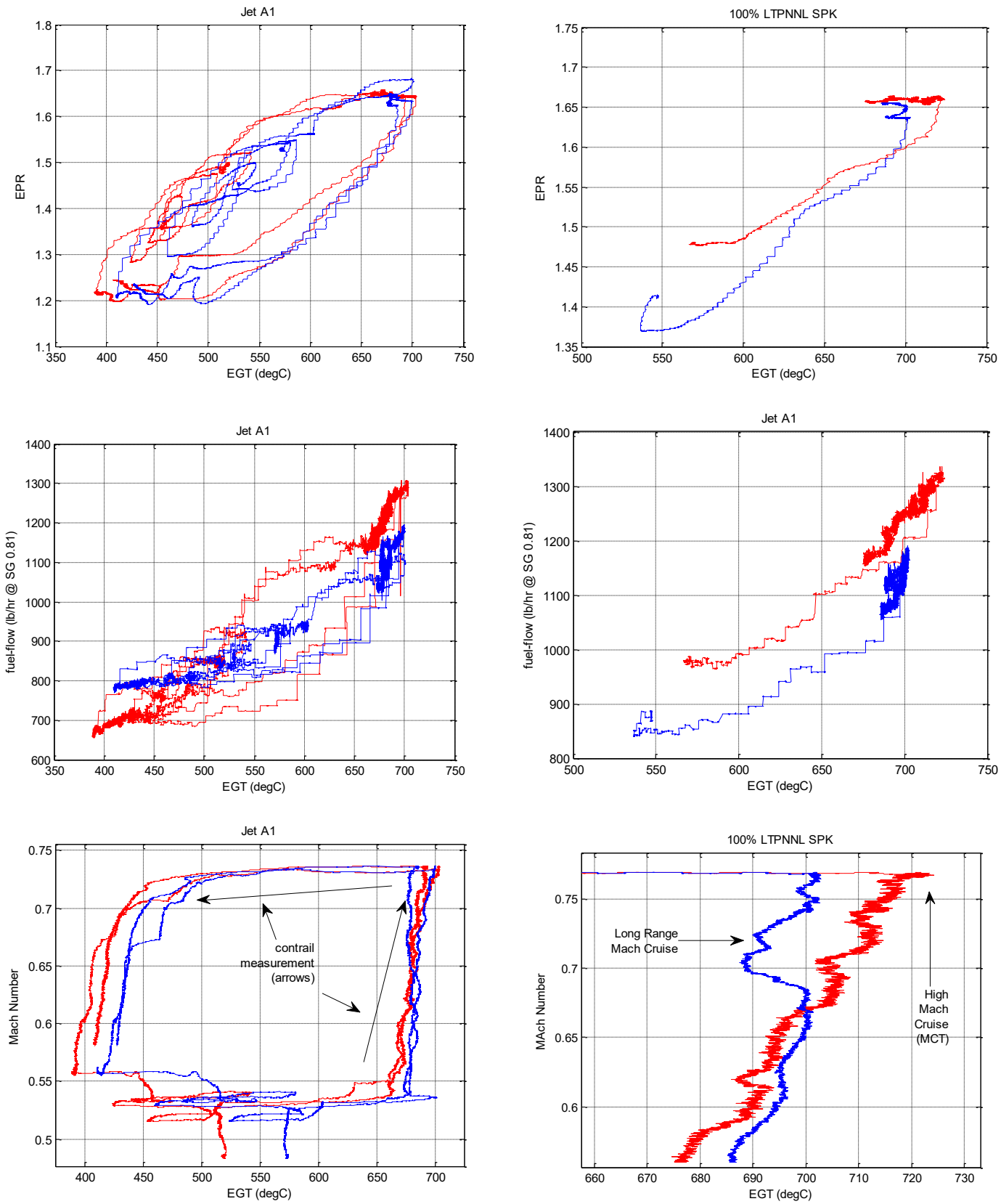

Figure 4 – 29th August 2019 flight, Long Range Cruise, *red* is port engine, *blue* is starboard engine: (*top*) engine gas generator performance, EPR ~ EGT (°C), (*middle*) fuel-flow (lb/hr/engine) ~ EGT (°C), (*bottom*) resultant aircraft Mach Number performance; (*left*) Jet A1; (*right*) 100% LTPNNL SPK.

Classification: Unclass
Distribution: UNLIMITED

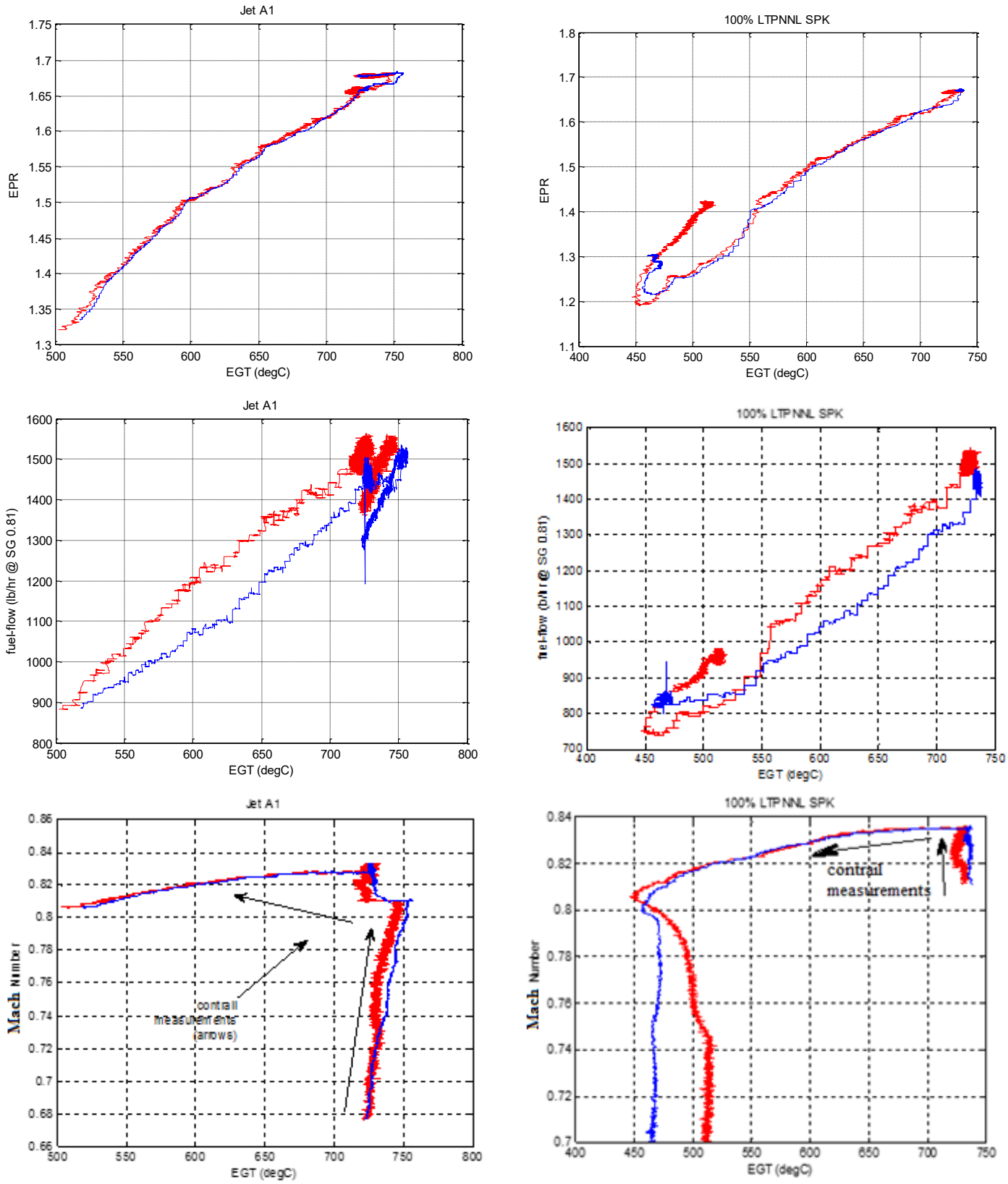

Figure 5 – 12th February 2020 flight, MCT Max Mach Cruise, *red* is port engine, *blue* is starboard engine: (*top*) engine gas generator performance, EPR ~ EGT (°C), (*middle*) fuel-flow (lb/hr/engine) ~ EGT (°C), (*bottom*) resultant aircraft Mach Number performance; (*left*) Jet A1; (*right*) 100% LTPNNL SPK.

Classification: Unclass
Distribution: UNLIMITED

3.1.5 Fuel-flows (measured as volumetric flow rate, using in-flow impellers, then calibrated to standard Jet A1 specific gravity, in order to indicate mass flow-rate) appeared to exhibit a slight difference between fuels, namely 1245 lb/hr/eng for Jet A1 and for LTPNNL, 1215 equivalent volumetric flow-rate to Jet A1 lb/hr/eng (*i.e.*, the mass-flow rate is referenced to an SG of 0.81 for both fuels, although the SG for LTPNNL was lower, 0.76), a volumetric flow-rate reduction of 2.4%. These flow-rate figures implied that, with the fuel tank volume the same regardless of whether Jet A1 or LTPNNL was burned, the overall range performance of the aircraft might be slightly improved in the case of LTPNNL.

3.1.6 For MCT (EGT 724°C), Jet A1 usage resulted in an EPR of 1.66 and a Mach Number of 0.831. 100% LTPNNL SPK resulted in slightly higher gas generator performance (an EPR of 1.67 and slightly improved aircraft performance, a cruise Mach Number of 0.835. Fuel-flows at equivalent lb/hr/eng as discussed above, were 1527 and 1502 for Jet A1 and LTPNNL, respectively, a volumetric flow-rate reduction of 1.6% for the latter.

3.1.7 With reference to the heats of combustion for the Jet A1 and LTPNNL, 43.0 and 43.9 MJ/kg, respectively, and the SG of 0.803 and 0.761, respectively, the volumetric heats of combustion were 34.5 MJ/L and 33.4 MJ/L, a reduction of 3.2%. Therefore the observed reduction in volumetric flow-rates at the same EGT values for LTPNNL would appear to have been associated with a higher order combustion effect, such as an increase in combustion-induced pressure, possibly due to a greater amount of gaseous products, in the form of greater water vapour from the increased hydrogen content of the LTPNNL. The increased EPR for LTPNNL at the same EGT values could have been significant in this regard.

3.1.8 The contrails were all obtained at high altitude (31-33,000 feet pressure altitude), such that the engine thrust range for the contrail measurements varied little, from 18-36% of engine rated thrust, 4501 lbf. Conversely, as seen in Figures 4 and 5, the thermofluid state range of engine operation varied widely, a gas generator thermodynamic range equivalent to 400-730 °C EGT range, and an airflow state range represented by 1.3-1.7 EPR range. This is to be borne in mind, when later considering potential variations of the production of emitted particulate matter particles.

3.1.9 When the LTPNNL fuel in the starboard feeder tank (Figure 6) approached depletion, the throttles (TLA) were reduced prior to transferring back to Jet A1 operation (*via* the port feeder tank, continually maintained full from the wing tanks *via* the low pressure, 15-25 psig nominally, port transfer pump). As shown in Figure 4 and Figure 5, reducing TLAs also reduced EGT, EPR and FF immediately (as regulated by the engine Fuel Control Units, which included high pressure engine-driven fuel pumps), followed by a decay in aircraft Mach Number. Not shown is the delivery fuel pressure, sensed prior to fuel entry into the FCUs. In the case of Jet A1, at low TLA, EGT, EPR and FF, a singular booster pump (whether the port or starboard), in crossfeed operation was sufficient for the fuel pressure to be maintained. However, in two-engine LTPNNL operation (as shown in the set-up of Figure 6), when the TLA was reduced significantly from that corresponding to MCT, fuel pressure fluctuations in the range of 0-20 psig occurred in the fuel feed to both engines. Transfer back to Jet A1, by turning the port booster pump ON and then the starboard booster pump OFF eliminated the fuel pressure fluctuations.

3.1.10 The booster pumps were electrically driven, a motor on each, driving a centrifugal in-line impellor. Outlet pressure generally dropped with increasing aircraft altitude, from nominally 25 psig at sea-level to 15-18 psig at high altitude. Absolute inlet pressure dropped

Classification: Unclass
Distribution: UNLIMITED

also, of course (the feeder tanks were lightly pressurised by engine bleed air, at nominally 2 psig). The 0-20 psig fuel pressure fluctuations had the characteristics possibly symptomatic of vane stall (*i.e.*, flow separation on the surfaces of the vanes) and cavitation.

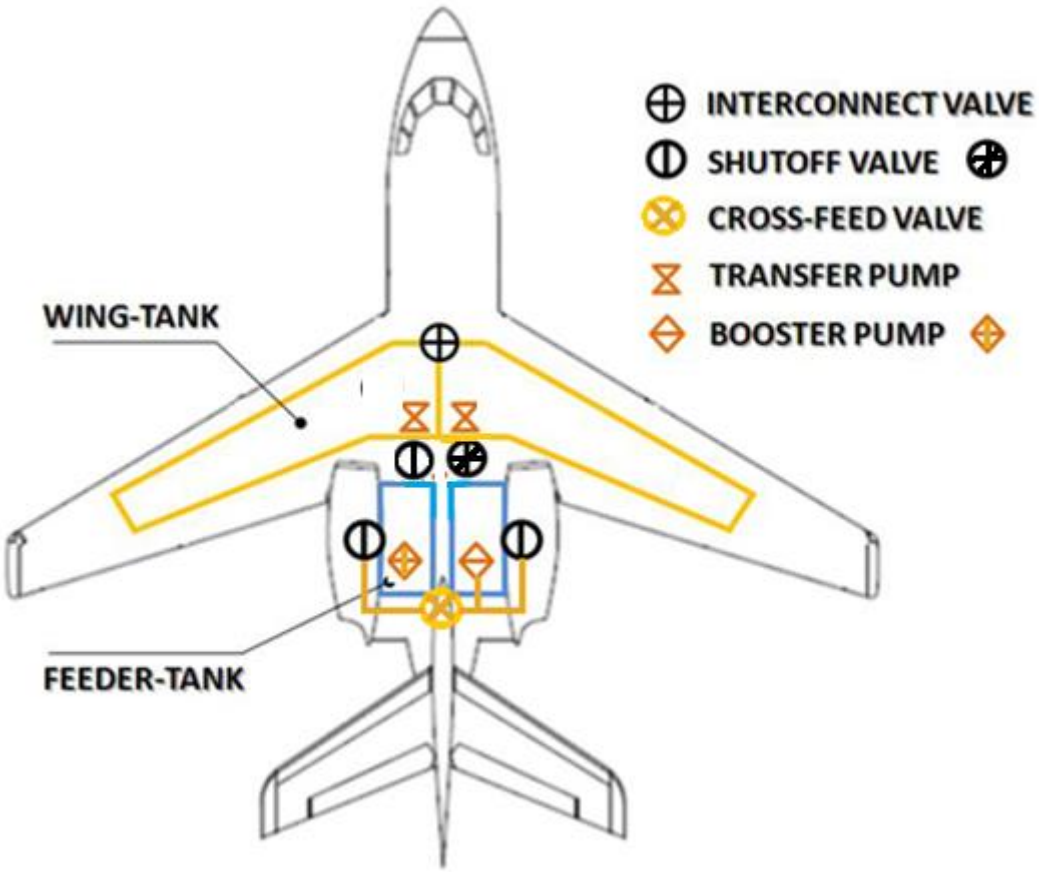

Figure 6 – NRC Falcon 20 fuel system schematic – in two-engine biofuel operation, the isolated Biofuel in the starboard feeder tank is fed via the starboard booster pump and the crossfeed valve, to both engines simultaneously.

3.2 Atmospheric conditions

3.2.1 For the 20th August 2019 flight, UTLS atmospheric conditions were non-saturated with respect to relative humidity over ice, RHi, whilst for the 29th August and 12th February flights, they were lightly super-saturated without visible cirrus, such that the initiation of contrail conditions, resulted in rapid development and spread of light cirrus.

3.2.2 Plot of the various background atmospheric conditions of air temperature, T_S, relative humidity, RH, relative humidity over ice, RHi, and RH lapse rate, $\partial RH/\partial z$, for each contrail plume cross-sectional data point, are presented in Figure 7. On present and previous flights, the derived ice particle FSSP-100 EIn delineation between sublimating and persistent contrails was approximately 10^{13} per kg jet fuel burned, highlighted in **[3]**.

Classification: Unclass
Distribution: UNLIMITED

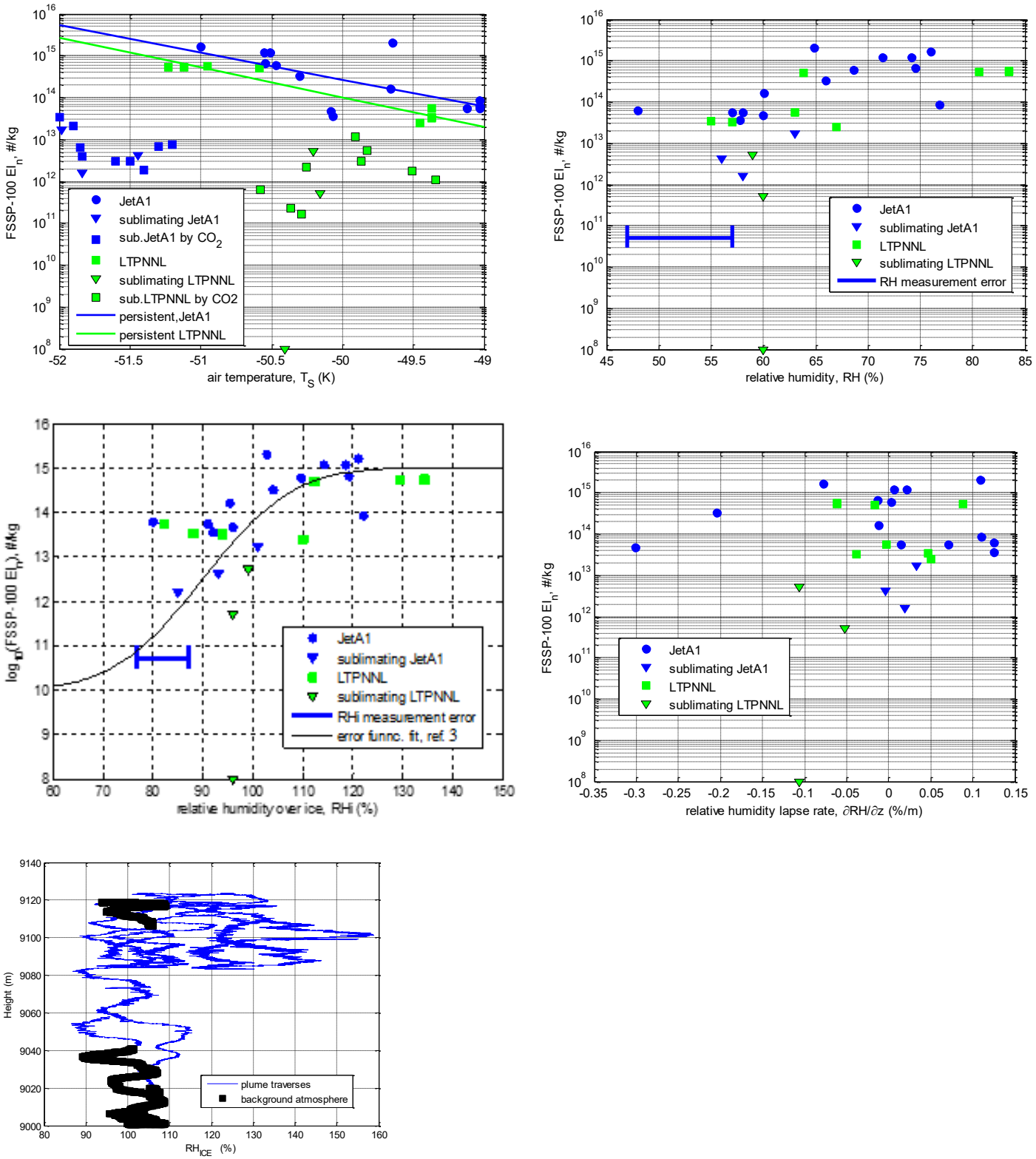

Figure 7– contrail ice particle EIn cross-plots with flight atmospheric conditions of: (*top left*) air temperature Ts, with regression lines included for each jet fuel, (*top right*) RH, (*middle left*) RHi, with an error function regressive fit to combined fuel data, (*middle right*) RH lapse rate, and (*bottom*) an example of the depth of a high RH pool.

Classification: Unclass
Distribution: UNLIMITED

3.2.3 RH inflight was derived from water vapour (WVap) mass fraction measurement by the LiCor 840A sensor. In previous recent projects, WVap measurements were calibrated by a combination of met balloon and numerical model (NWP) output data. The current project flights were obtained during atmospheric conditions of greater UTLS circulation, for which WVap pooling (e.g., 29th August 2019) or drying (e.g., 20th August 2019) occurred at sub-regional scales, and hence was poorly predicted in both cases by both NWP and met balloon data. Furthermore, in the high ice particle number concentrations encountered, it is possible that, in spite of the Licor probe inlet particle separator, some ice ingestion occurred, resulting in water molecule registration as apparent water vapour rather than ice. Thus, as shown in Figure 7, the RH derivation error was significant.

3.2.4 The same applied to RHi derivation. The highest ambient RHi occurred during the 100% LTPNNL contrail of the 12th February flight. The sub-regional scale of RH pooling was illustrated by the depiction in Figure 7 that RHi was lower during the Jet A1 contrail on the same flight. The Falcon flew eastwards during the Jet A1 contrail, then reversed direction in a left-hand turn, to fly westwards (offset approximately fifteen miles to the North) during the LTPNNL contrail. Included in the plot of RHi is the error function used to model [4] the effect of RHi, on earlier wide-ranging RHi flight data. RH lapse rate $\partial RH/\partial z$, was near-zero for the persistent contrails, meaning that such contrails were formed in atmospheric air-mass, with a relatively deep layer of pooled RH, an example of which is included in Figure 7.

3.2.5 Apart from the prime variable for the formation of contrails (*i.e.*, RHi), persistent contrails exhibited a dependency upon air temperature T_S, as indicated by the lines of regression in Figure 7, showing an increase in contrail ice particle number concentration with reducing Ts, for each fuel. This was consistent with earlier NRC biofuel contrail projects **[3][4]**. Amidst other atmospheric, engine state and contrail age variations, the LTPNNL fuel had lower FSSP EIn, *c.f.* Jet A1 by a factor of approximately 50%, a constant differential with reducing Ts.

3.3 Contrail type and variability

3.3.1 Whether sublimating or persistent, NRC Falcon 20 (FA20) contrails were generally UJW type. The trailing vortices were typically warmer than ambient air temperature. Temperatures elevations of 1 to $\geq$6°C above ambient (the latter in slender vortex filaments) have been measured using an over-damped TAT probe during the course of contrail flights, which would result in an under-estimation of the temperature elevations. Consequently there was little defined vortex core condensate. At air transport representative Mach (>0.7), wing circulation was relatively low magnitude, so the vortex descent rate was likewise low and the downward dynamic effect upon contrail development quite limited. Rather, the contrails remained concentrated at the flight level of the generator, in the slight depression of the viscous wake. The 20th August contrails were sublimating, with a background RHi of approximately 60%. The 29th August and 12th February contrails were persistent, background RHi approximately 90% - 95%, and tended to rapidly induce cirrus formation in the surrounding air. The 12th February 2020 contrails were more persistent and the highest background RH of all contrails occurred on the 100% LTPNNL contrail.

3.4 CN concentration during clear sky to contrail transition

3.4.1 The climb and level-off on the 12th February flight were analysed for the effects upon measured CN (CN 7610 sensing of combined volatile and non-volatile PM) of the

Classification: Unclass
Distribution: UNLIMITED

absence or presence of contrail. The climb was conducted with the CT-133 in-trail of the Falcon 20 (operating on Jet A1 petroleum fuel), at an in-trail separation distance of 200-2000 m. The CT-133 conducted full emission plume sampling during the climb, which involved lateral and vertical traverses through and outside the lateral and vertical extent of emissions. Traverses resulted in unsteadily higher aerodynamic drag, which was the cause of the varying in-trail separation (lower aerodynamic drag was achieved by the CT-133 operating on trailing vortex-surfing).The climb and level-off height, CO_2, CN and FSSP activity parameters are presented as Figure 8.

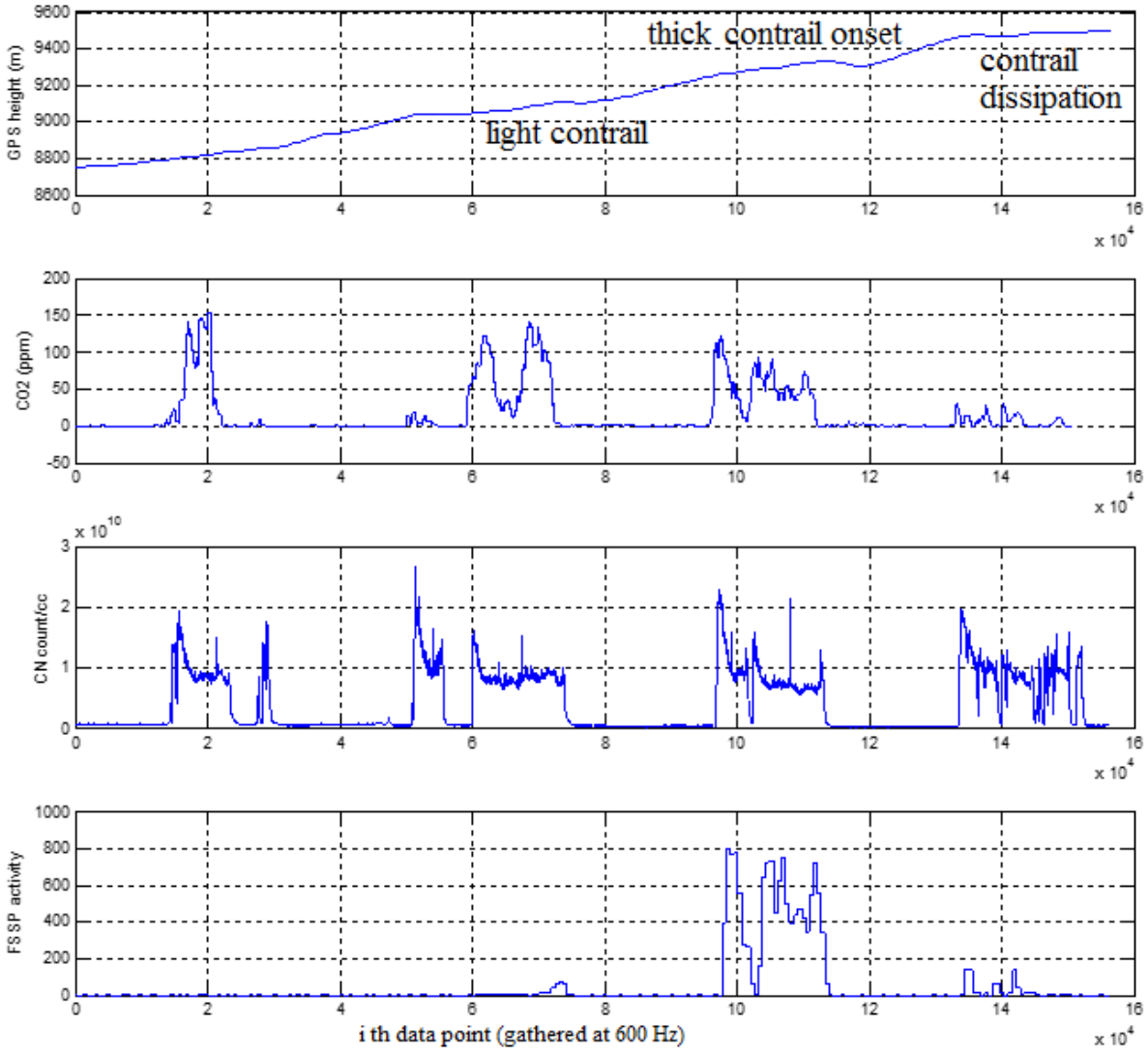

Figure 8 – Top-of-climb segment for the CT-133 emissions/contrail sampling aircraft: *(top)* **aircraft height (m),** *(second from top)* **Picarro elevated CO_2 concentration (ppm), collocated with CN 7610,** *(third from top)* **CN concentration (#/cc),** *(bottom)* **FSSP-100 activity factor (1000 represents probe saturation).**

3.4.2 Over 8800-9300 m height, there was no change in engine power or the Mach Number of the Falcon, so that the emissions could be reasonably considered to be 'frozen' over the height sub-range. For the first two residence/traverse groups represented by the species elevations, there was negligible contrail (slightly at the75000th point), thence thick

Classification: Unclass
Distribution: UNLIMITED

contrail (212 x the number concentration of ice particles). Two plume/contrail species cross-sections were re-constructed, presented in Figure 9 and Figure 10, for faint contrail conditions, <80,000th, and thick contrail conditions, 95,000-120,000th points, respectively.

3.4.3 The cross-sections for faint contrail conditions appeared to be fully covered. Area integration of the Picarro CO_2 plume in Figure 9, divided by fuel burn, kg, per metre line-of-flight, resulted in an EIm of 3.15 kg/kg, indicating that the plume was covered adequately. Similar integration of the CN plume resulted in CN EIn =1.08e15 #/kg Jet A1 burned. Peak CN concentrations approached 18,000 /cc. Note that for the NRC CT-133 CN 7610 installation, it was operated in high-speed, analogue acquisition mode, **[7]** (for which the saturation cut-off was determined by initial flights to be approximately 25,000 #/cc, [2]**[8]**). FSSP ice particle EIn was derived to be $4.33_{10}{}^{11}$, confirming faint contrail conditions **[3]**, whilst peak ice particle concentration approached 200 /cc.

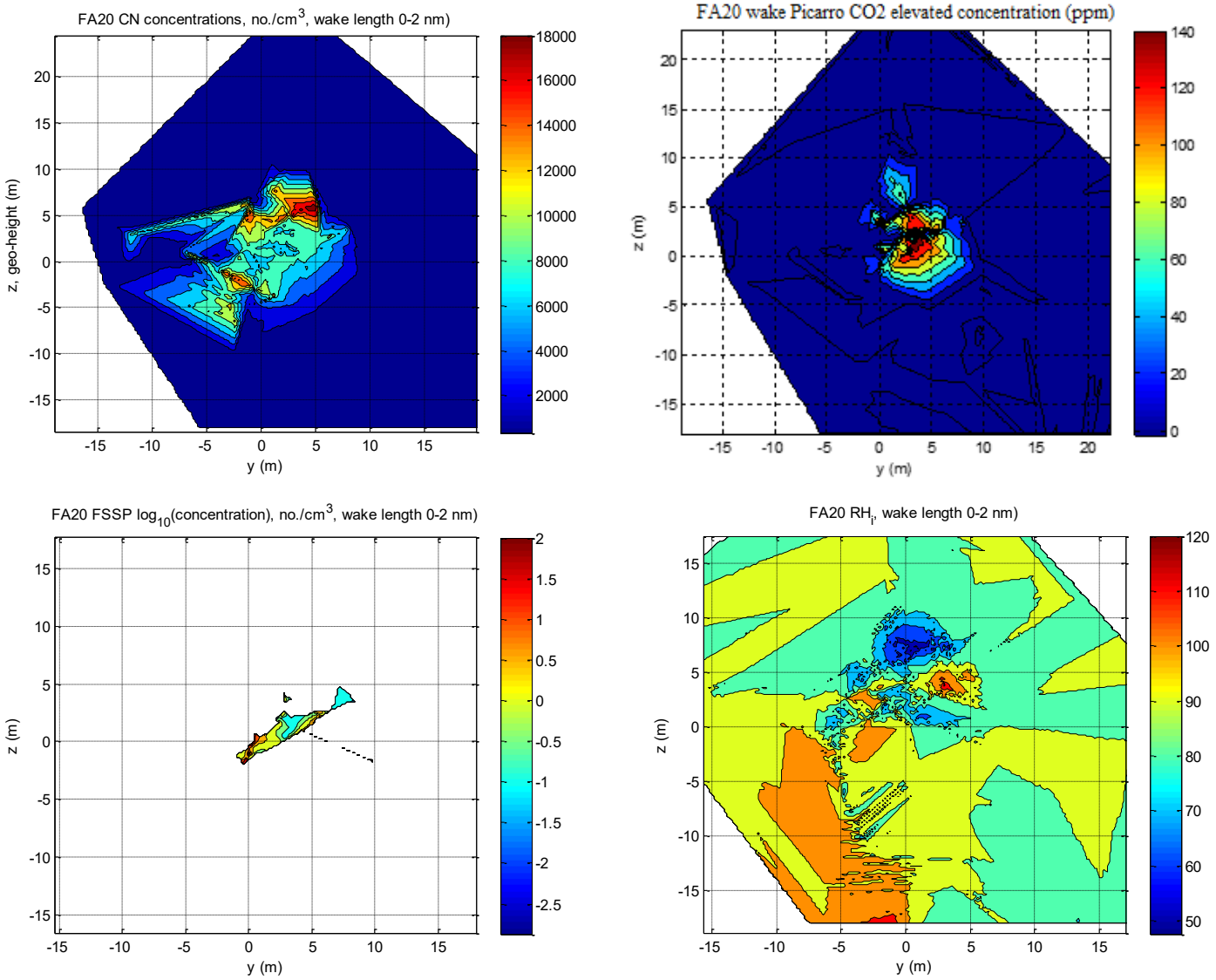

Figure 9 – plume/contrail re-constructed cross-section near top-of-climb, for light contrail conditions, <80000th points: *(top left)* CN (#/cc), *(top right)* Picarro elevated CO_2 (ppm), *(bottom left)* FSSP ice particle (#/cc), *(bottom right)* approximate RH_i (RH over ice).

Classification: Unclass
Distribution: UNLIMITED

3.4.4 Compared to the faint contrail, it is seen there was no increase in CN EIn, hence no particular evidence of ice particle shattering on the opening of the isokinetic inlet. On the contrary, CN EIn in clear air was greater, which could have been evidence of either aerosol agglomeration in the contrail ice nucleation process, or (less likely) isokinetic inlet shattering of particles in the non-contrail atmospheric condition. In the thick contrail case, peak CN concentrations approached 20,000 /cc, similar but 10% higher than the faint contrail case. Comparing spatially-correlated CN, FSSP (starboard underwing pod) and RHi (from the nose-mounted Licor 840A, spatial translation corrections applied) parameters, it was seen (Figure 9) that the CN peak concentration (≈20,000 #/cc) occurred outside the contrail in the locality of lowest RHi, but were spatially coincident with peak CO_2 concentration. This might support either of the above-stated implications, namely PM agglomeration in the contrail ice nucleation process or possible PM shattering in the non-contrail case.

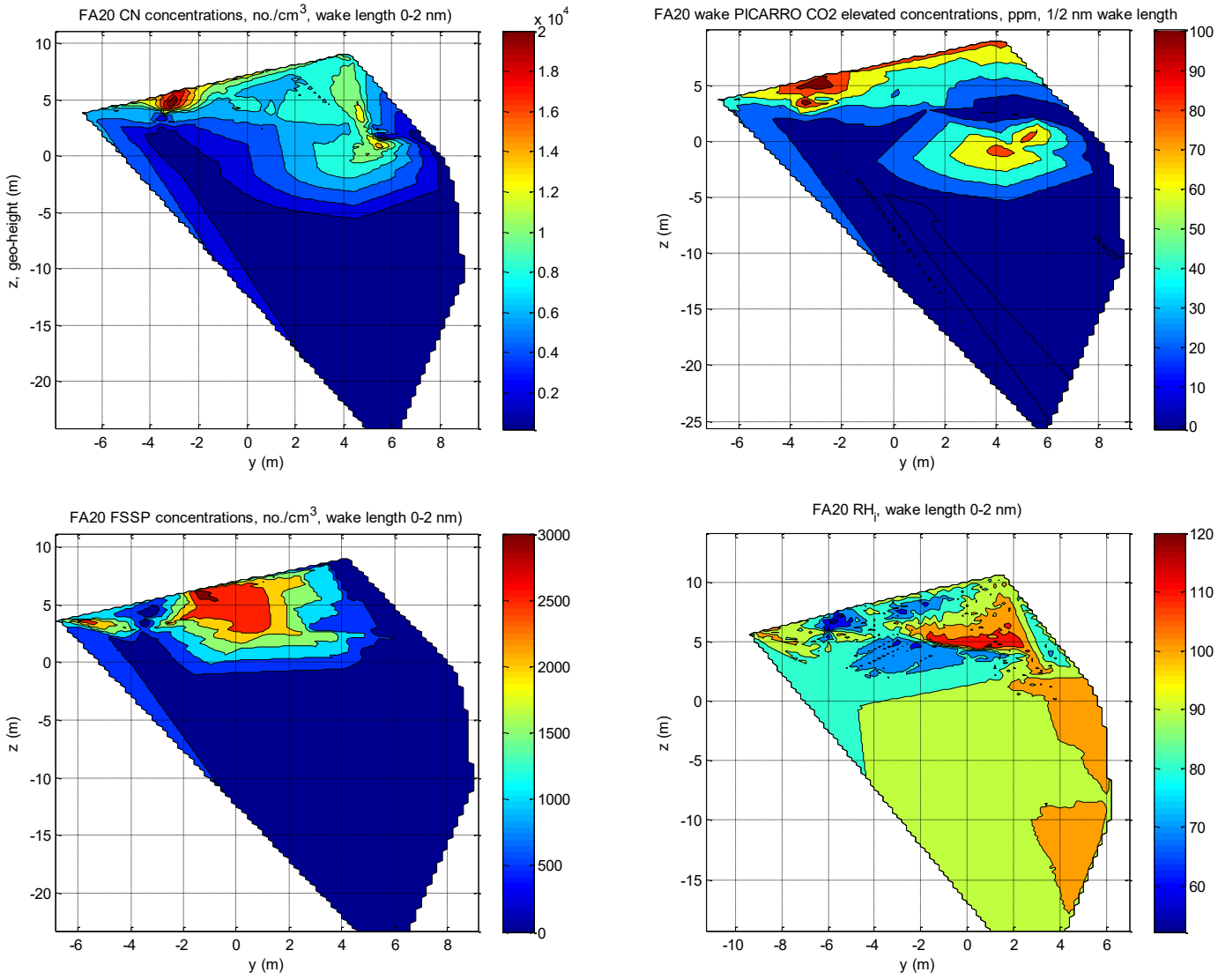

Figure 10 – plume/contrail re-constructed cross-section at top-of-climb, for thick contrail conditions, 95000-120000th points: *(top left)* **CN (#/cc),** *(top right)* **Picarro elevated CO_2 (ppm),** *(bottom left)* **FSSP ice particle (#/cc),** *(bottom right)* **approximate RH_i, RH over ice.**

Classification: Unclass
Distribution: UNLIMITED

3.5 CN emissions measurements in contrail conditions

3.5.1 The starboard and port pods suffered internal plumbing leaks during the 20th August flight. The starboard pod leak resulted in loss of particulate registration above 7 km, whilst the port pod leaked resulted in loss of spatiotemporal coherence of LII300 data, preventing the re-construction of BC plume cross-sections (discussed in the next section).

3.5.2 As discussed earlier, the lack of CN data prompted an effort to compare EIn derivations using CO_2 concentration as the intermediary. Previously, **[1,2,3,4]**, NRC CT133 aerosol and ice particle EIn values were derived autonomously, by the integration of the re-constructed species cross-sectional plume per metre of flight-path length, divided by the fuel-burn per metre. This was similarly conducted for CAAFCOMR contrail data. In addition, EIn values were derived from CO_2 molar mass concentration above background, per unit-volume and compared to EIn derived by the autonomous method.

3.5.3 To illustrate the temporal comparison between Jet A1 PM emissions and LTPNNL PM emissions, a time-trace (*albeit* non-spatially correlated) of the CN concentration during the latter stages of fuel changeover is presented in Figure 11. The changeover consisted of transferral of the right engine from Jet A1 to LTPNNL, a delay of one-minute to assess stable operation, followed by transferral of the left engine from Jet A1 to LTPNNL. Full removal of Jet A1 from the engine fuel supply plumbing and engine fuel control units (FCU) would appear to have taken 1-2 minutes in this case, based upon the high-rate fall of CN concentration, followed by the slower fall-rate, the latter associated with the progressive increase in wake/contrail length and hence, age.

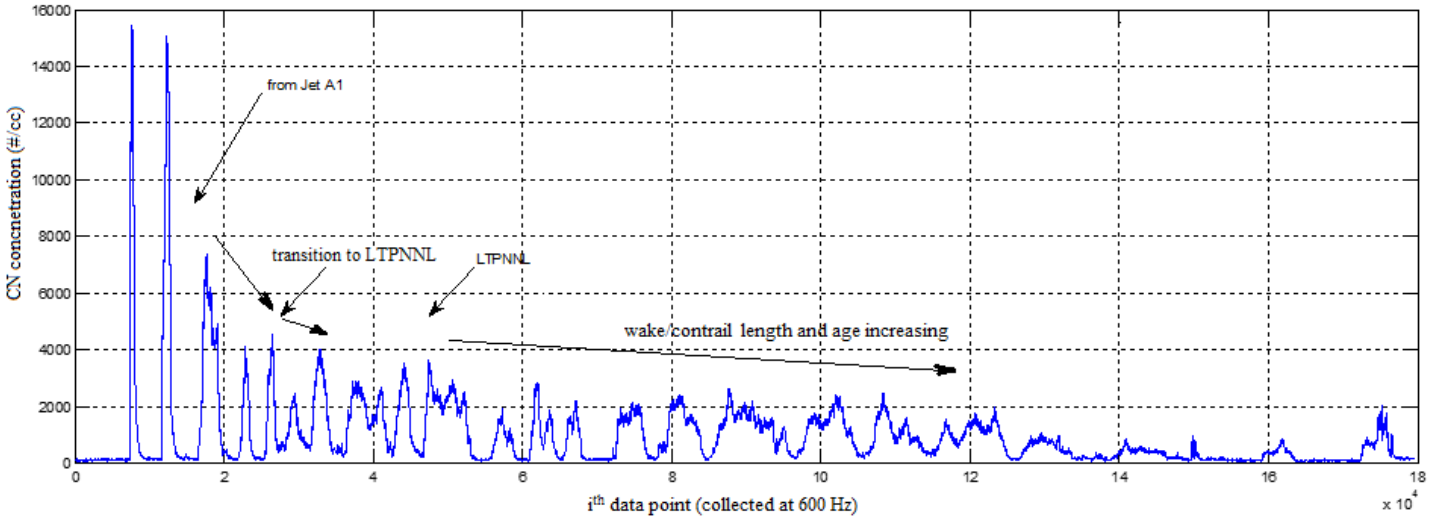

Figure 11 – 12th February 2020 flight: non-spatially correlated time-trace of CN concentration (#/cc) measurements within the FA20 contrail, during latter stages of transition from Jet A1 to 100% LTPNNL, both engines.

3.5.4 Unlike CO_2 (wherefore, the concentration fall-rate is associated with molecular diffusion), the CN fall-rate is relatively slow, under the influence of containment aerodynamic forces, produced by wake pressure-deficit cross-plane and axial gradients. Whereas CO_2 concentration typically reduced to background levels by several nautical miles, e.g. **[3]**, early NRC cruise emissions measurements demonstrated the longevity of elevated CN concentrations, for example **[9]**, peaks of ≈4,000 #/cc after one-hour wake age from a

Classification: Unclass
Distribution: UNLIMITED

B777 on Jet A. Peak CN concentrations were of the order of 16,000 #/cc on Jet A1, diminishing to 2-4,000 #/cc, when fully transferred to LTPNNL.

3.5.5 Re-constructed plume cross-sectional CN 7610 data for the 29th August flight are presented in Figure 12, (a) for Jet A1 and (b) for 100% LTPNNL. It is seen that peak CN concentrations were within the range of 11-25,000 #/cc for Jet A1, *c.f.* 8-16,000 #/cc for 100% LTPNNL, in other words approximately ½ that of Jet A1. Note that wake pressure-gradient induced aerodynamic forces could result in differing concentrations for CN plumes of differing size distributions. Particle size information was not available from the CN7610 counter.

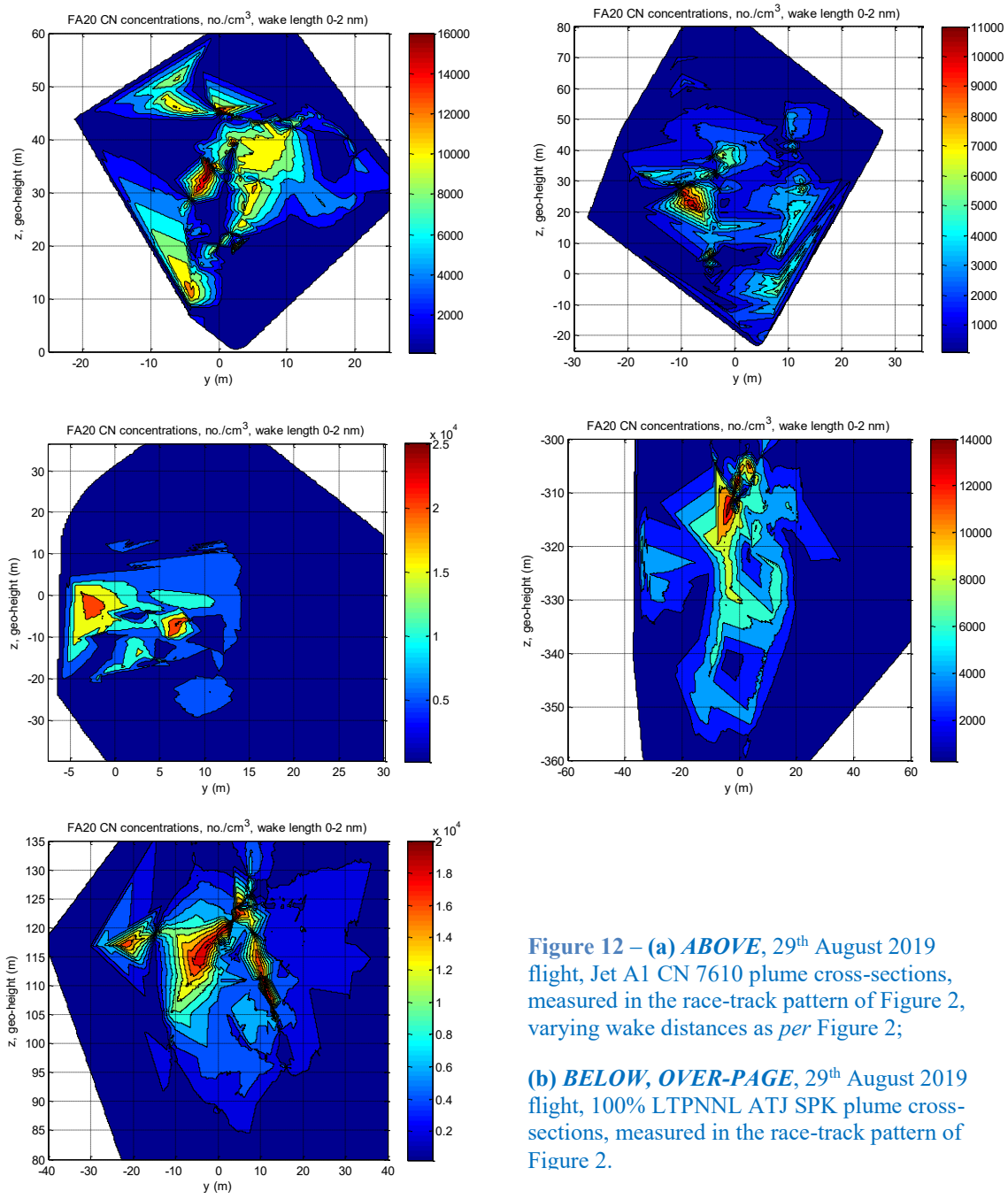

Figure 12 – (a) *ABOVE*, 29th August 2019 flight, Jet A1 CN 7610 plume cross-sections, measured in the race-track pattern of Figure 2, varying wake distances as *per* Figure 2;

(b) *BELOW, OVER-PAGE*, 29th August 2019 flight, 100% LTPNNL ATJ SPK plume cross-sections, measured in the race-track pattern of Figure 2.

Classification: Unclass
Distribution: UNLIMITED

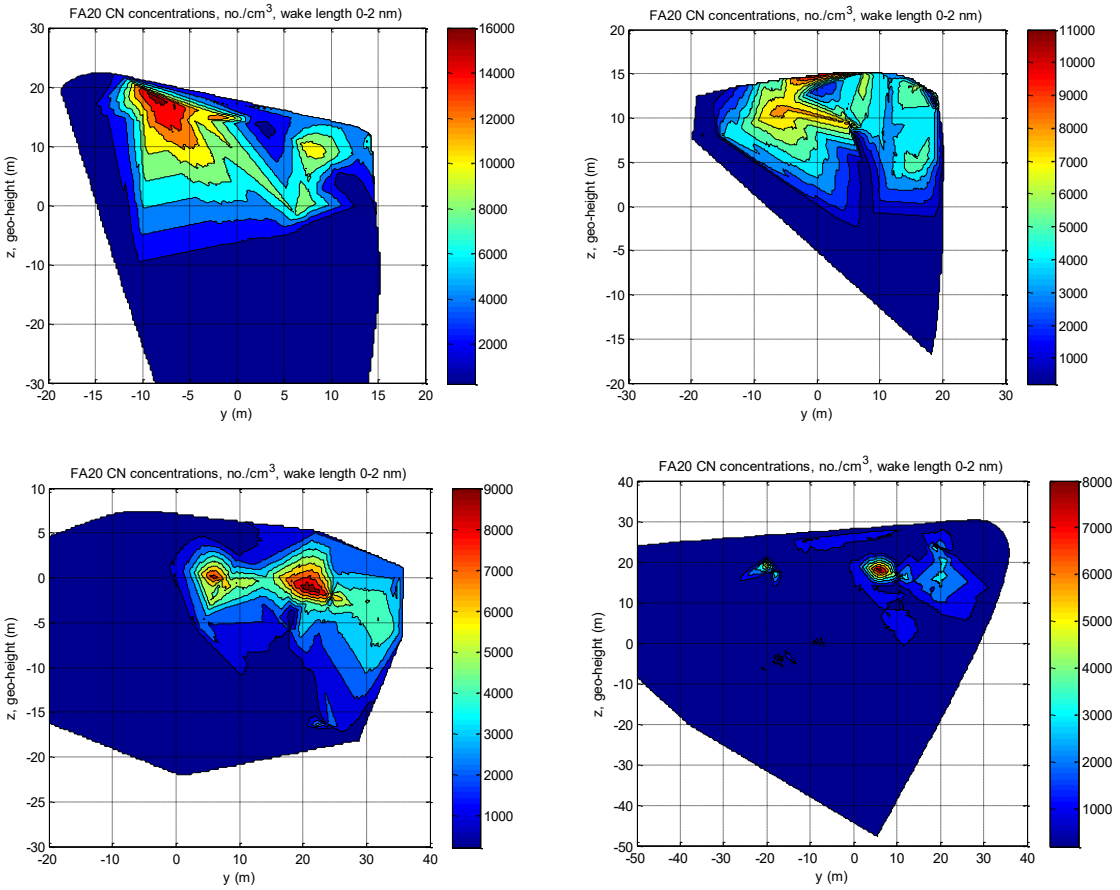

3.6 CN evolution

3.6.1 CN EIn values derived by volume integration of plume cross-sections were plotted against emission plume age, in Figure 13 for the two methods, (i) the autonomous method of holistic plume cross-section integration, and (ii) the intermediary method of using CO_2 concentration as the species-comparator.

3.6.2 Considering the variations of CN EIn with contrail (wake) age, first-order regressive fits have been added to the plots. The Jet A1 CN EIn data points formed a line of regression which showed a slight increase in apparent EIn with wake/contrail age, with considerable oscillatory scattering above and below the regression line – but no apparent dependency upon method of derivation, other than to say that as the contrail age increased, CO_2 concentration reduced towards sensor resolution and repeatability limits, increasing CN EIn uncertainty *via* low CO_2 concentration. (The seemingly inaccurate 10^{17} EIn value at an age of 0.6 minutes is discussed below.)

3.6.3 On the other hand, the LTPNNL regression line showed a less gradual reduction in apparent EIn with emissions age, with low scatter for the autonomous-method derived EIn and moderate scatter for CO_2-derived EIn.

Classification: Unclass
Distribution: UNLIMITED

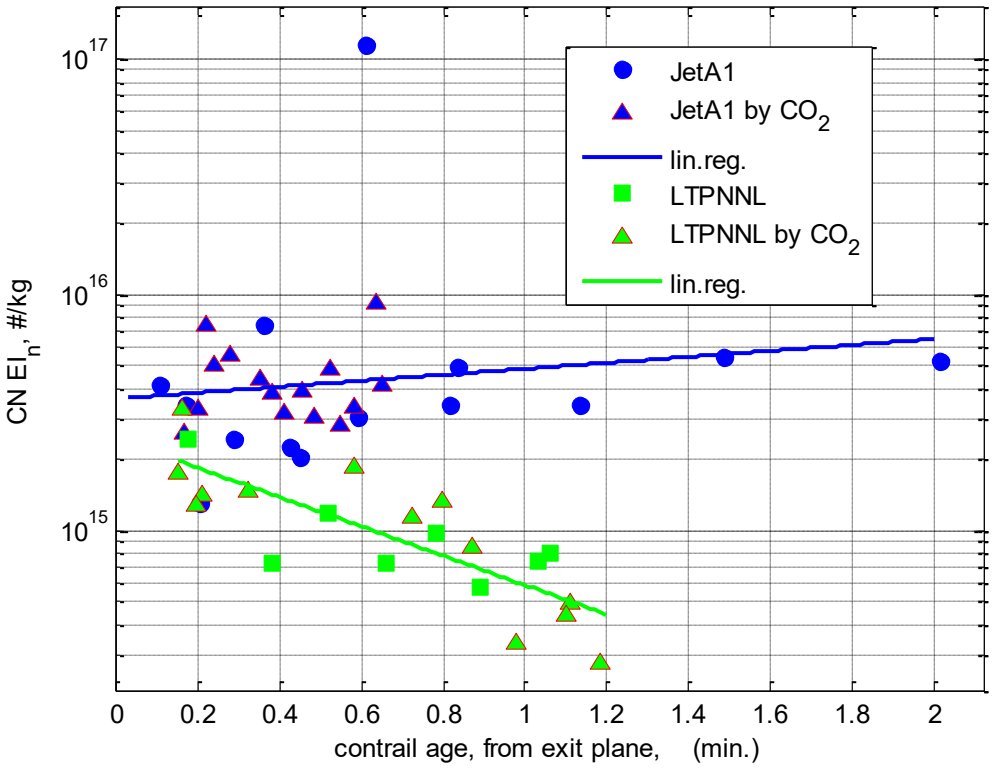

Figure 13– 29th August 2019 & 12th Feb 2020 flights, Jet A1 and 100% LTPNNL CN EIn, derived by holistic plume integration, and derived by CO2-intermediary method – all plotted against emissions age.

3.6.4 In rationalising the differences, from earlier data **[3,4]** it could be expected that the majority of Jet A1 CN particles would be volatile, whereas essentially all the CN for 100% LTPNNL would be non-volatile (BC) particles. Hence, the majority of Jet A1 CN, as sensed by the CN 7610 would be likely formed by solidification and subsequent deposition of mostly gaseous compounds (significantly sulphates), a progressive size expansion process to and beyond the size threshold for CN 7610 sensing. Brown *et al* **[1]** reported increases in B772 CN EIn until 12 minutes wake/contrail wage, followed by relatively sharp reductions in EIn values. On the other hand, 100% LTPNNL CN, being BC, could be expected to have minimal size and number growth after being emitted. A reduction in EIn with age in the presence of contrail conditions would imply a possible process of particle conglomeration, possibly aided by the ice nucleation process.

3.7 CN production

3.7.1 As mentioned above, a high Jet A1 CN EIn value of approximately 10^{17} was derived at an age of 0.6 minutes. Although it appears like an outlier, a review of engine thermodynamic state at this spatiotemporal location would appear to suggest the value might be correct. This cross-sectional re-construction related to the end of a straight flight leg, with a significant reduction of TLA as the NRC Falcon undertook a base turn. As discussed earlier, engine thrust did not vary greatly at high altitude, from 18-36% sea-level rated thrust. On the other hand, the variation in thermodynamic state at high altitude was greater, a range from 64% to 98% rated EGT. The production of emitted CN would likely be related to engine thermodynamic state, and could expectedly have greater variation amidst a greater

Classification: Unclass
Distribution: UNLIMITED

range of the latter. Thus, a plot of derived EIn against engine thermodynamic state is shown in Figure 14.

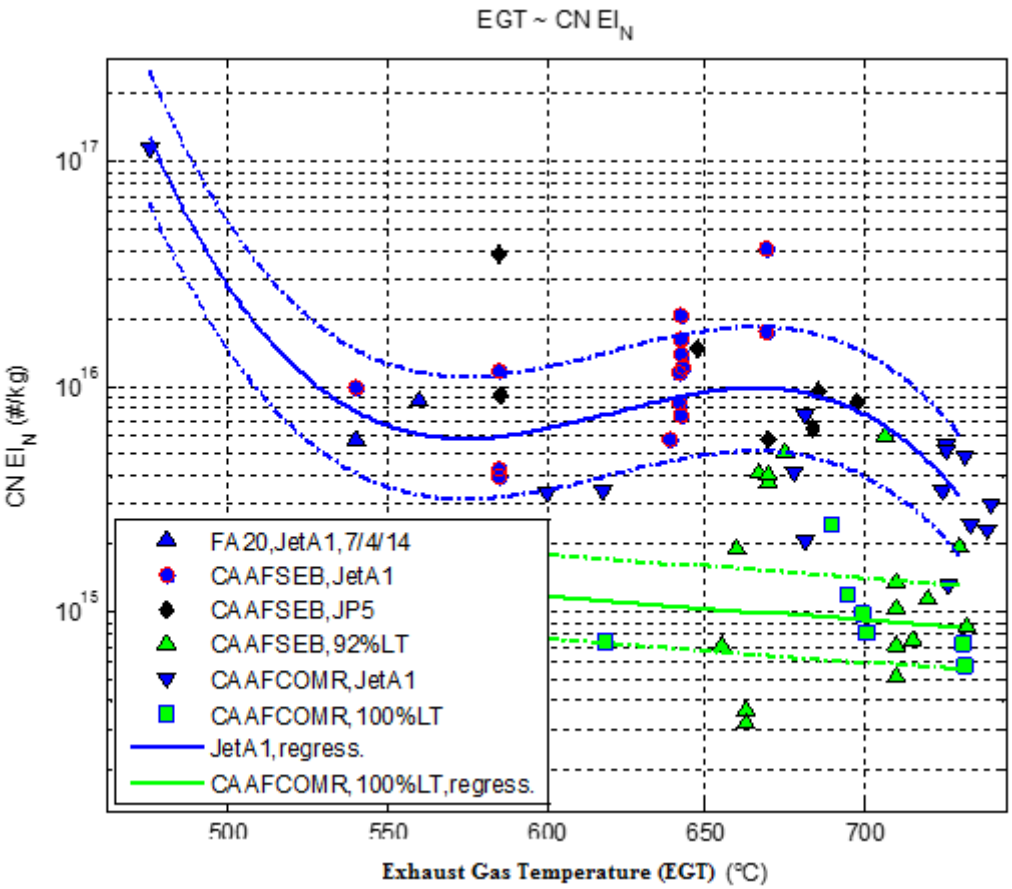

Figure 14 – plot of CN EIn ~ engine thermodynamic state, represented by EGT, for both CAAFCOMR data and earlier [4] CAAFCEB (92% LTPNNL, Jet A1, 'A-5'JP-5) data; dotted curves are ±1σ standard deviations for lines of regression of JetA1 (third order, CAAFCOMR & CAAFCEB combined) and 100% LTPNNL (CAAFCOMR) fuels (NOTE: no data is blocked by the legend).

3.7.2 It is seen that a third-order line of regression to the Jet A1 CN EIn values (CAAFCOMR and CAAFCEB combined) has the shape of a rise at low EGT, a plateau at intermediate EGT and a fall towards maximum EGT. A first-order regressive fit to 100% LTPNNL data exhibited only a low-rate of fall towards maximum EGT (almost a flat-line). Also shown are ±1σ standard deviation margins to the regressive fits. The σ for the Jet A1 data is greater than for the 100% LTPNNL data, for which σ was approximately 30%, with only 1 data point >1σ removed. The 92% LTPNNL data thermodynamic scatter was greater than for 100% LTPNNL.

3.7.3 That 100% LTPNNL CN EIn exhibited no significant correlation with engine thermodynamic state emphasised the likelihood that the wake age effect was dominant.

3.7.4 Conversely the 10^{17} value of CN EIn at low EGT emphasised the correlation with CN production, due to engine thermodynamic state. Nevertheless, there appeared to be a Jet A1 wake-age correlation of increasing CN EIn, an opposite trend to 100% LTPNNL, wherefore the wake-age effect was to reduce CN EIn.

Classification: Unclass
Distribution: UNLIMITED

3.8 Atmospheric state effects upon CN EIn

3.8.1 In the above sections, potential correlations were considered for Jet A1 and 100% LTPNNL emitted PM (CN number count EIn), against evolution (wake/contrail age) and production (engine thermodynamic state) effects. There were potentially other experimental effects, in particular atmospheric conditions, which like engine state, cannot be fully controlled parameters of the experiment. For example, pooling of RH and Ts in the UTLS atmosphere was a prevalent occurrence generally.

3.8.2 Potential relations between CN EIn and background atmospheric parameters are considered in the cross-plots of Figure 15, for Ts (°C), pressure ALTitude (feet), RHi (%) and RH lapse rate (∂RH/∂z, %/m) in contrail conditions, for the two fuels, Jet A1 and 100% LTPNNL SPK. Drawn in the four plots are first-order regressive fits for the cases where correlation appeared to have potentially existed, namely (i) LTPNNL with air temperature, a reduction in EIn with colder air, (ii) an increase in EIn with RHi for Jet A1, (iii) a slight reduction of EIn with RHi for LTPNNL, (iv) an increase in EIn with ∂RH/∂z for Jet A1 and (v) an increase in EIn with ∂RH/∂z for LTPNNL.

3.8.3 All five potential correlations related to atmospheric parametric associations of first order significance in the formation of contrails, although possibly opposite in effect upon ice particle generation **[1,3,4]**, such as the reduction in LTPNNL CN EIn with reducing air temperature, or the increases in CN EIn with ∂RH/∂z. In the latter case, the contrails of **[1]** were DC-8 Trailing Wake Vortex type, wherefore the ice EIn effect with ∂RH/∂z was negative due to vortex descent, whereas presently NRC Falcon 20 contrails had no TWV component (due to warm vortex cores) – rather they were all Upper Jet Wake type, for which a positive ice EIn effect of ∂RH/∂z could be expected.

3.8.4 With the above observations in mind, it could be concluded that sensed CN EIn wake/contrail age effects correlations existed in the data, and could be associated with dynamic effects of the physical/chemical processes of contrail formation and persistence, although potentially markedly different for the two fuels, because of the prevalence of volatile CN PM for Jet A1 and the absence of volatile CN PM for LTPNNL (with no sulphur nor aromatics content).

3.9 Fuel CN comparison

3.9.1 The 100% LTPNNL CN EIn data was obtained mostly at 97-102% MCT, whilst the majority of 92% LTPNNL/8% 150ND (CAAFCEB, **[4]**) data was obtained at 90-98% MCT, wherefore Jet A1 resulted in a greater engine production of emitted CN.

3.9.2 Combustion efficiency of Jet A1 could be reasonably expected to be most efficient at maximum-rated EGT (highest limit temperature by design). Conversely, off-design lower EGT could be expected to be of reduced combustion efficiency to some extent (*i.e.,* incomplete combustion), with resultant increased production of emitted PM.

3.9.3 The different Jet A1 CN EIn reflected these slight but significant differences in engine operation. Table 4 contains the petroleum and biofuel CN EIn for each experiment, CAAFCEB (92%) and CAAFCOMR (100%). The ratios between biofuel and petroleum fuel CN EIn showed some percentage reduction in PM due to the presence of sulphur and aromatics in 92% LTPNNL, compared to their complete absence in 100% LTPNNL, namely PM lessened from 18% to 13% that of Jet A1, respectively.

Classification: Unclass
Distribution: UNLIMITED

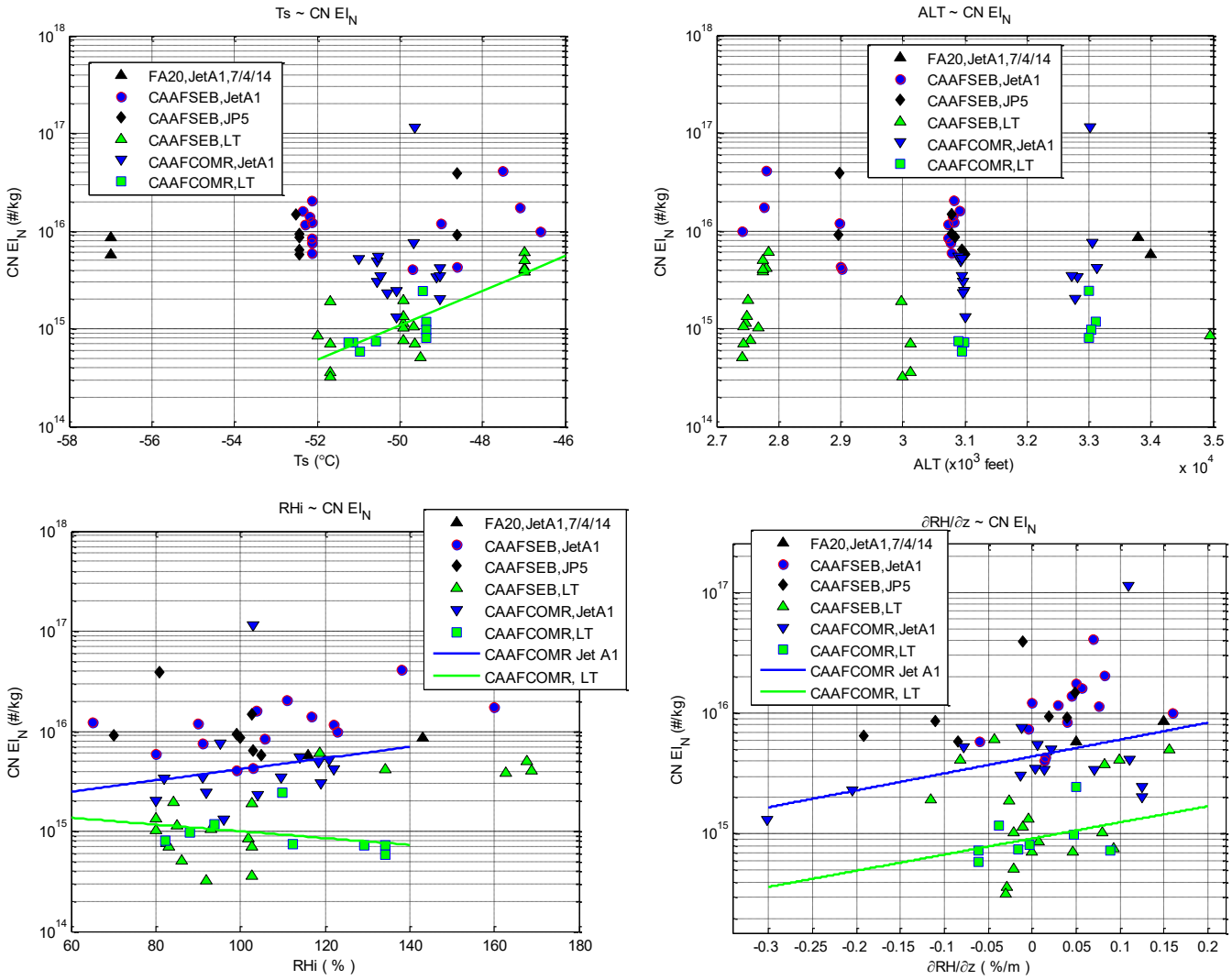

Figure 15 – CN EIn cross-plots of Falcon data,, 2014, CAAFCEB and CAAFCOMR: CN EIn (derived by re-constructed plume cross-sectional integration) against various background atmospheric parameters: (*top left*) air temperature (°C), (*top right*) height (feet), (*bottom left*) RHi (%), and (*bottom right*) RH lapse rate (%/m). Lines of regression are shown for some parameters, for CAAFCOMR data only.

Table 4 – (*below*) CN 29th August data, Jet A1 and LTPNNL statistical comparison of standard deviations (as % of the mean values of the lines of regression) from regressive data lines, for each EIn derivation method (ref. Figure 6 CN EIn data-sets).

FUEL	**σ / mean[CN EIn] , for differing derivation methodologies, CAAFCOMR**		**Mean[CN EIn], #/kg**	
	Autonomous – holistic plume cross-section integration	**Comparative – using CO_2 concentration as the intermediary**	**CAAFCOMR 29th Aug 2019 & 12th Feb 2020 flights (avg)**	**CAAFCEB flights (avg)**
Jet Al	42%	46%	$7.2 \pm 3.2_{10}{}^{15}$	$1.13_{10}{}^{16}$
100% LTPNNL	15%	39%	$0.92 \pm 0.2_{10}{}^{15}$	$1.99_{10}{}^{15}$ (92% SPK)
		Ratio to JetA1	**0.13** (-0.06/+0.15)	**0.18**

Classification: Unclass
Distribution: UNLIMITED

3.10 BC mass emissions

3.10.1 BC mass was measured by the LII300 sensor in the port underwing pod, for which an evaporative ice-removing in-line heater was installed. Flight data from the 20th August 2019, prompted investigation of the LII300 performance. The investigation revealed that the pod plumbing configuration was sensitive to one or more flight-induced plumbing leaks (possibly vibration-induced, or temperature-cycling induced), the effects of which were to de-synchronise and de-sensitise BC data, such that spatial re-construction was not possible. The leaks were eliminated for the 29th August flight, providing good BC data. In spite of plumbing condition monitoring, the data of the 12th February 2020 flight appeared to indicate return of one or more plumbing leaks.

3.10.2 Nevertheless, the airflow heater would appear to have been successful in evaporating contrail ice, such that re-constructed BC cross-sectional plumes was possible.

3.10.3 Comparative black carbon (BC) plume re-constructed cross-sections are presented in Figure 16 for Jet A1 and LTPNNL, for the 29th August 2019 flight. Peak BC concentrations depicted in Figure 16 generally corresponded spatially to peak contrail ice particle number concentrations (presented in the following section).

3.10.4 The spatial form of the BC plume cross-section corresponded reasonably with that of the contrail for Jet A1. However, the LII300 was operating close to a resolution limit, more so for LTPNNL (which has less BC emissions than Jet A1, **[4]**), so that the LTPNNL BC re-constructions of Figure 16 were of poor spatial definition (although cross-sectional integrations were still possible and conducted).

3.10.5 The volume (per metre flight-track) integrand derivations of BC EIm are plotted in Figure 17, as functions of wake/contrail age and engine thermodynamic state, as represented by EGT, respectively. The high BC EIm point is seen to correspond to low EGT and therefore corresponds with the high CN EIn in the same thermodynamic engine operating state, discussed previously.

3.10.6 Concerning the potential correlation of BC EIm with wake/contrail age, conservation of mass should be expected, as emitted BC would be non-reactive. For Jet A1, conservation is apparent for similar engine EGT states, *albeit* with a relatively large standard deviation, 80 mg/kg, and a mean value of 198 mg/kg.

3.10.7 The scatter for 100% LTPNNL was lower, σ = 27 mg/kg; however, a non-conservative trend of increasing BC EIm was indicated. With respect to LTPNNL CN EIn (≈BC EIn), a trend of decreasing EIn occurred with age (Figure 13), for which ice nucleation-induced agglomeration was hypothesised. Such a process would increase BC particle size, making it more visible to the sensing BC-emitted incandescence threshold of the LII300, whilst operating within the low BC concentration environment of high altitude flight. The ratio of BC EIm for LTPNNL (46$\pm$27 mg/kg, using all data points), *c.f.* Jet A1 at the same EGT state, was estimated to be 0.17(-0.10/+0.46), including the uncertainty of 1σ for both fuels.

Classification: Unclass
Distribution: UNLIMITED

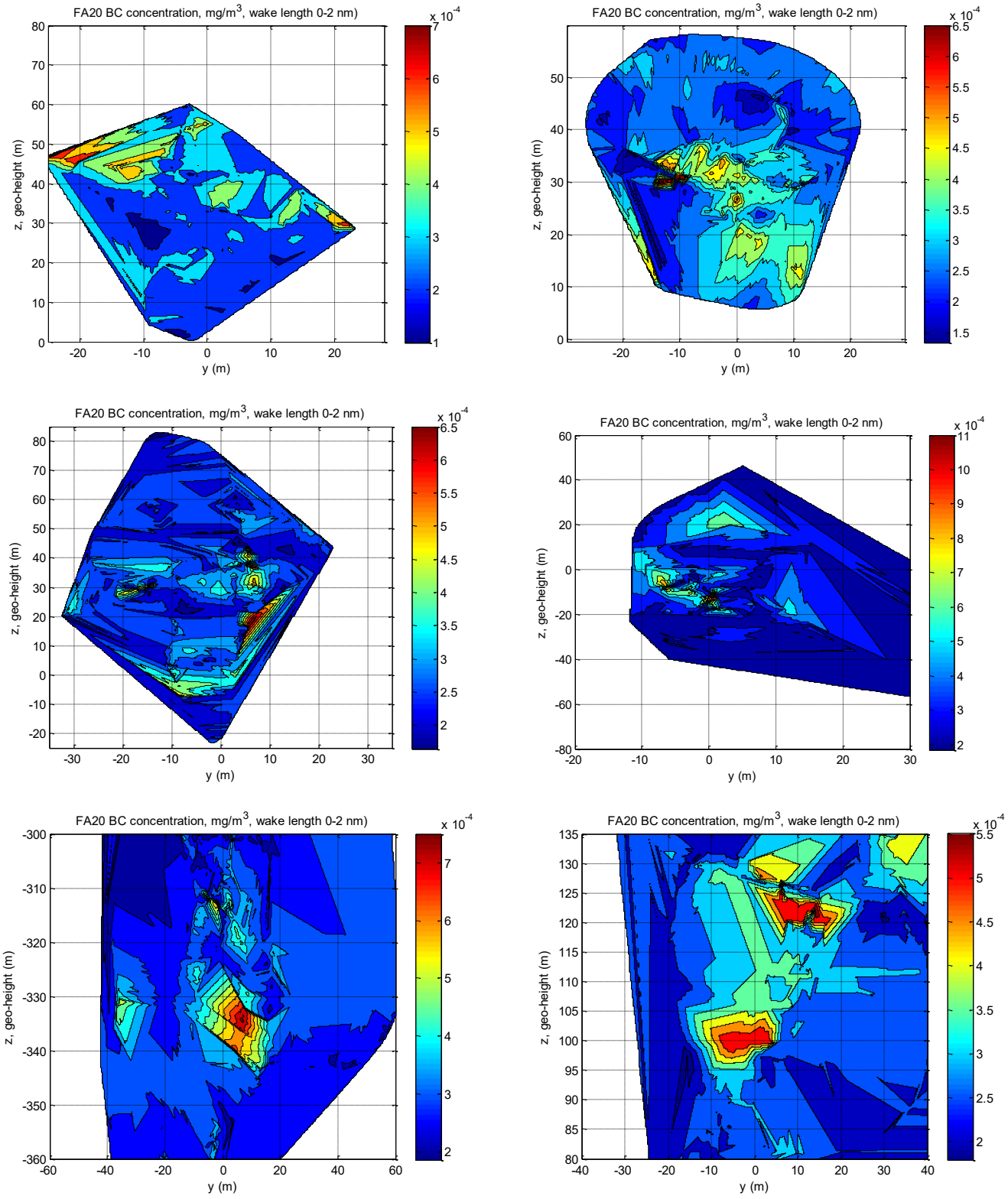

Figure 16 – 29th August 2019 flight, BC plume cross-sections, measured in the race-track pattern of Figure 2, varying wake distances as *per* Figure 2, for Jet A1 (*ABOVE*), and for 100% LTPNNL (*BELOW, OVERPAGE*).

Classification: Unclass
Distribution: UNLIMITED

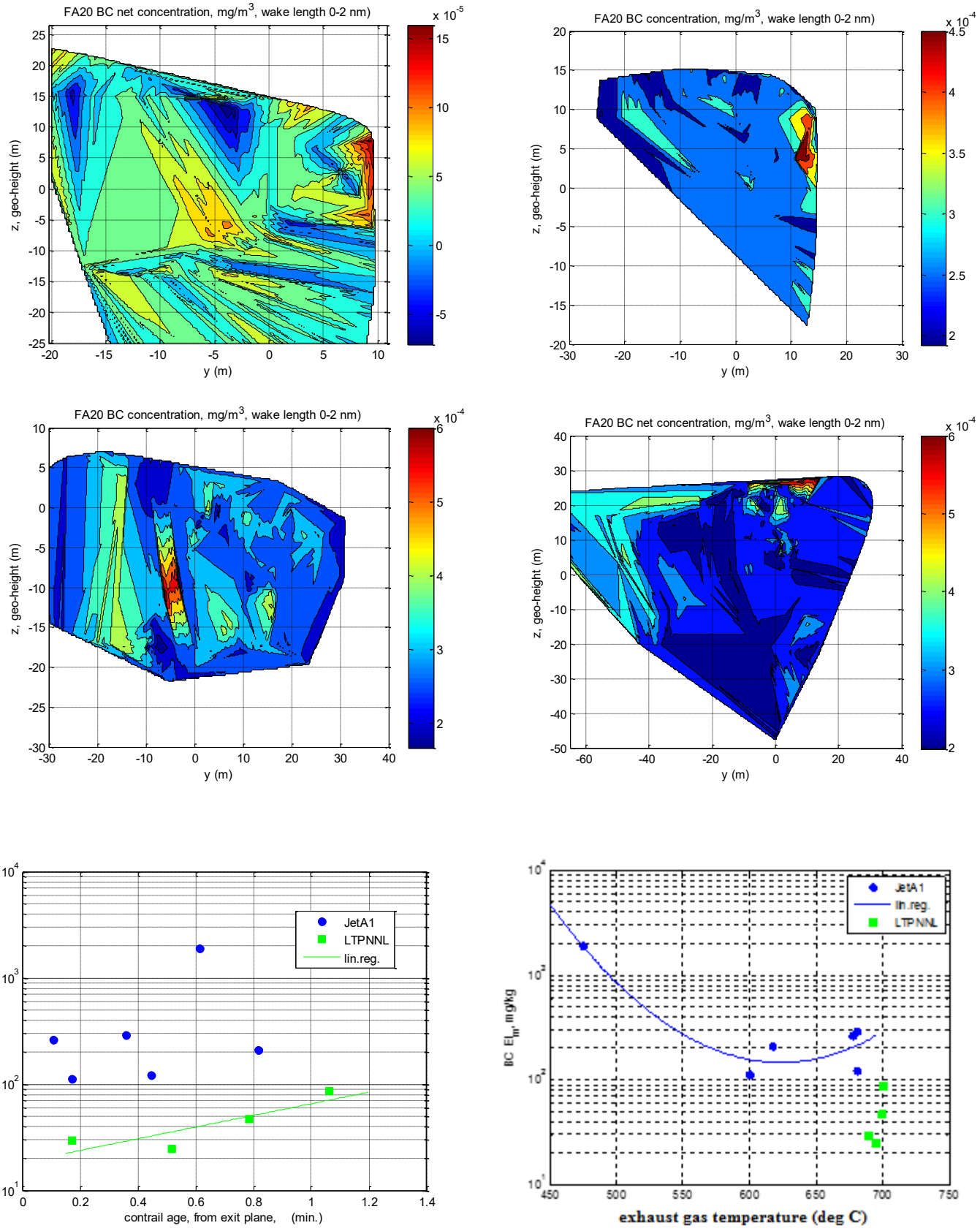

Figure 17 – 29th August 2019 flight, BC EIm plotted against wake/contrail age (*left*), and against engine thermodynamic operating state (*right*).

Classification: Unclass
Distribution: UNLIMITED

4. CONTRAIL ANALYSIS & DISCUSSION

4.1 Fuel properties

4.1.1 Test fuel properties for Jet A1 and LTPNNL, as used on the project, are summarised in Table 5. The LTPNNL fuel was from the same production batch as that used on the earlier CAAFCEB project **[4]** using 92% LTPNNL.

4.1.2 On the 29th August 2019, free water was discovered post-flight, in the Falcon starboard feeder fuel tank and in one of the stainless steel LTPNNL drums. The entry point appeared to a rim-retainer failure on the bottom rim of the drum. The dissolved water was negligible, and in agreement with ref. **[11].** The free water is not represented in the tabulation of properties, Table 5.

Table 5 – Fuel properties, NOTE: total hydrogen content is presented for NMR test values.

Fuel [reference]	Total hydrogen content (%m), mean±1σ	Sulphur content (%m)	Aromatics content (% vol)	Naphthalene (% vol)	Net heat of combustion (MJ/kg)	Density at 15°C (gm/l)
a priori Jet A1 **[3]**	13.74	0.058	18.3	0.9	43.2	808
a priori JP-5 ('A-3') **[12][18]**	13.7	0.02	18.3	0.9	43.0	827
Jet A1 **[10]**	13.85±0.04	0.05	18.5	0.7	43.0	803
LTPNNL ATJ SPK **[11]**	15.33	0.000096	0	-	43.9	761

4.2 Contrail overall characteristics

4.2.1 The contrails on the 20th August 2019 flight were sublimating-type. On the 29th August 2019 flight, they were persistent-type. These two flights used engine thrust settings applicable to Long Range Cruise (M≈0.73), due to relatively small scale-size of contrail conditions. Contrails were persistent on the flight of the 12th February 2020, which used MCT Maximum Rated Cruise (M≈0.83), because the lateral extent of contrail conditions was large (initially the Jet A1 contrail was sublimating, before the wide-area high RHi was entered). All contrails from the NRC Falcon 20 were Upper Jet Wake type. Trailing vortices were warm (+1 to +6 °C above Ts), with negligible trailing vortex condensate.

Typical contrail cross-sectional properties are illustrated in

4.2.2 Figure 18 for the 20th August, Figure 19, 29th August 2019 and Figure 21/21, 12th February 2020. FSSP ice particle number concentrations tended to be slightly lower and more localised, in the case of LTPNNL fuel, with particle size somewhat smaller, for the 29th August flight. At higher engine thrust, 12th February 2020, initial growth rates would appear to have been greater for the LTPNNL fuel, and extinction coefficient cross-sectional maxima likewise greater. In the example given, the LTPNNL contrail would appear to have been in a homogenous median size state of ice particle spectra

Classification: Unclass
Distribution: UNLIMITED

4.2.3 For all the spatiotemporal examples of Figures 18-21, it is seen that the contrail ice particle number density peaks were lower for LTPNNL *c.f.* Jet A1.

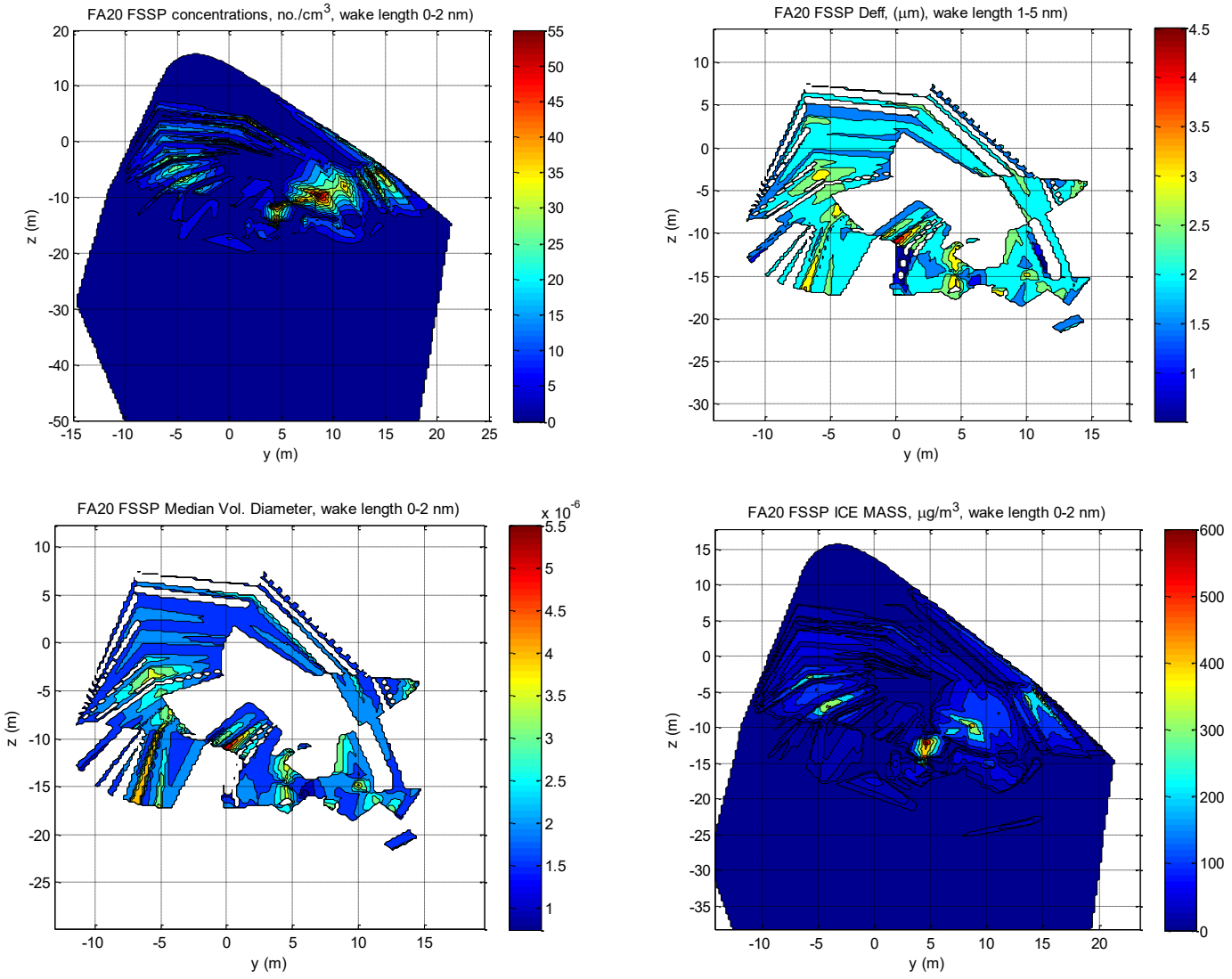

Figure 18 – 20th August 2019 flight: (*ABOVE*) Jet A1 contrail plume cross-sections, (*top left*) ice particle number concentration (#/cc), (*top right*) effective optical size (µm), (*bottom left*), MVD (µm), (*bottom right*), ice mass concentration (µg/m^3); (*BELOW, OVER-PAGE, FIGURE & KEY CONTINUED).*

Classification: Unclass
Distribution: UNLIMITED

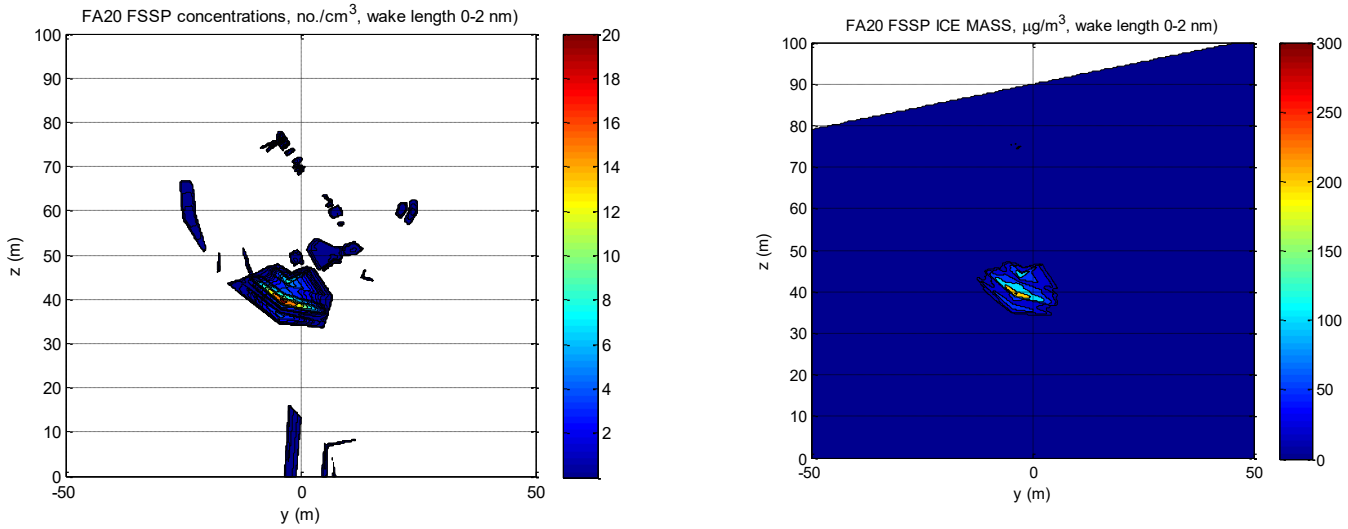

Figure 18 CONCLUDED (*ABOVE*) – 100% LTPNNL 20th August 2019, sublimating contrail cross-sections, (*above left*) ice particle number concentration (#/cc), (*above right*), ice mass concentration (µg/m^3); due to low ice particle, there were only a few resolved spectral median values, ≈2.3 µm.

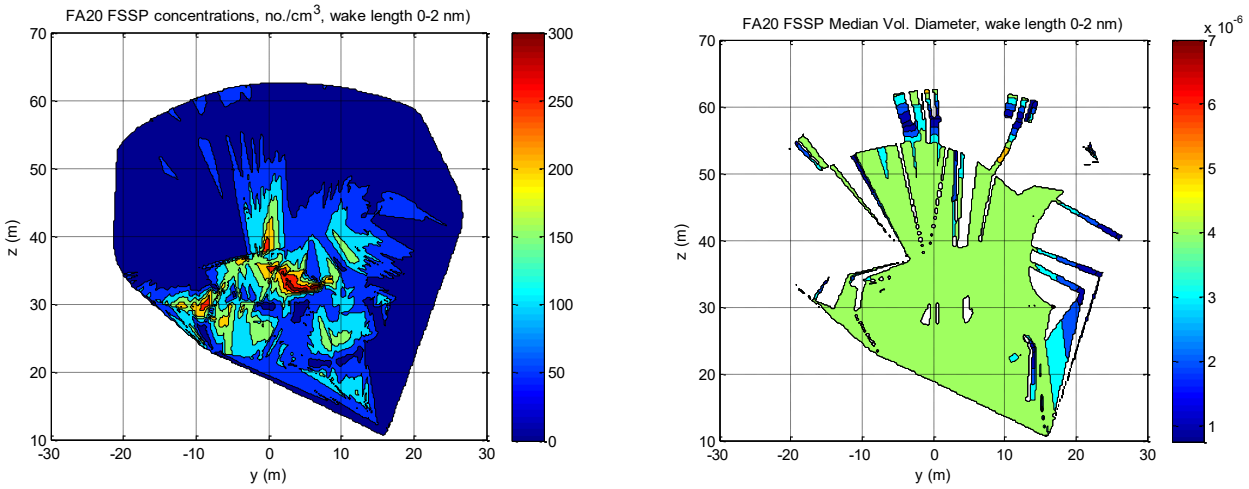

Figure 19 – 29th August 2019 flight, persistent contrail re-constructed cross-sections: (*ABOVE AND BELOW, OVER-PAGE*) Jet A1 example of contrail plume cross-sections, (*above left*) ice particle number concentration (#/cc), (*above right*) MED (µm);

Classification: Unclass
Distribution: UNLIMITED

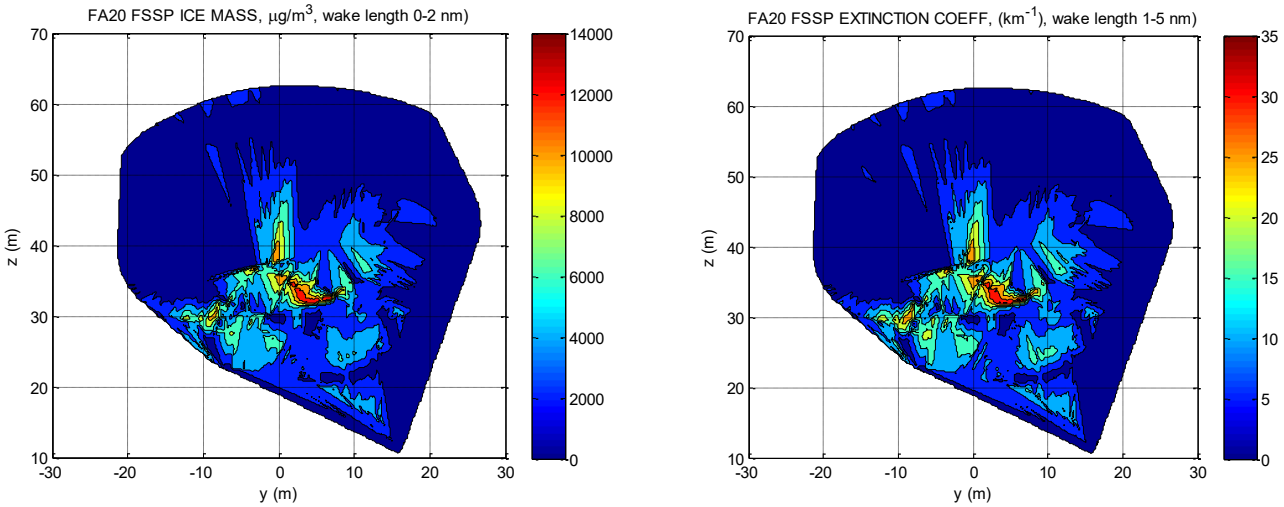

Figure 20 *CONTINUED* – Jet A1 example, continued, (*above left*), ice mass concentration (µg/m^3), (*above right*) extinction coefficient (km^{-1});

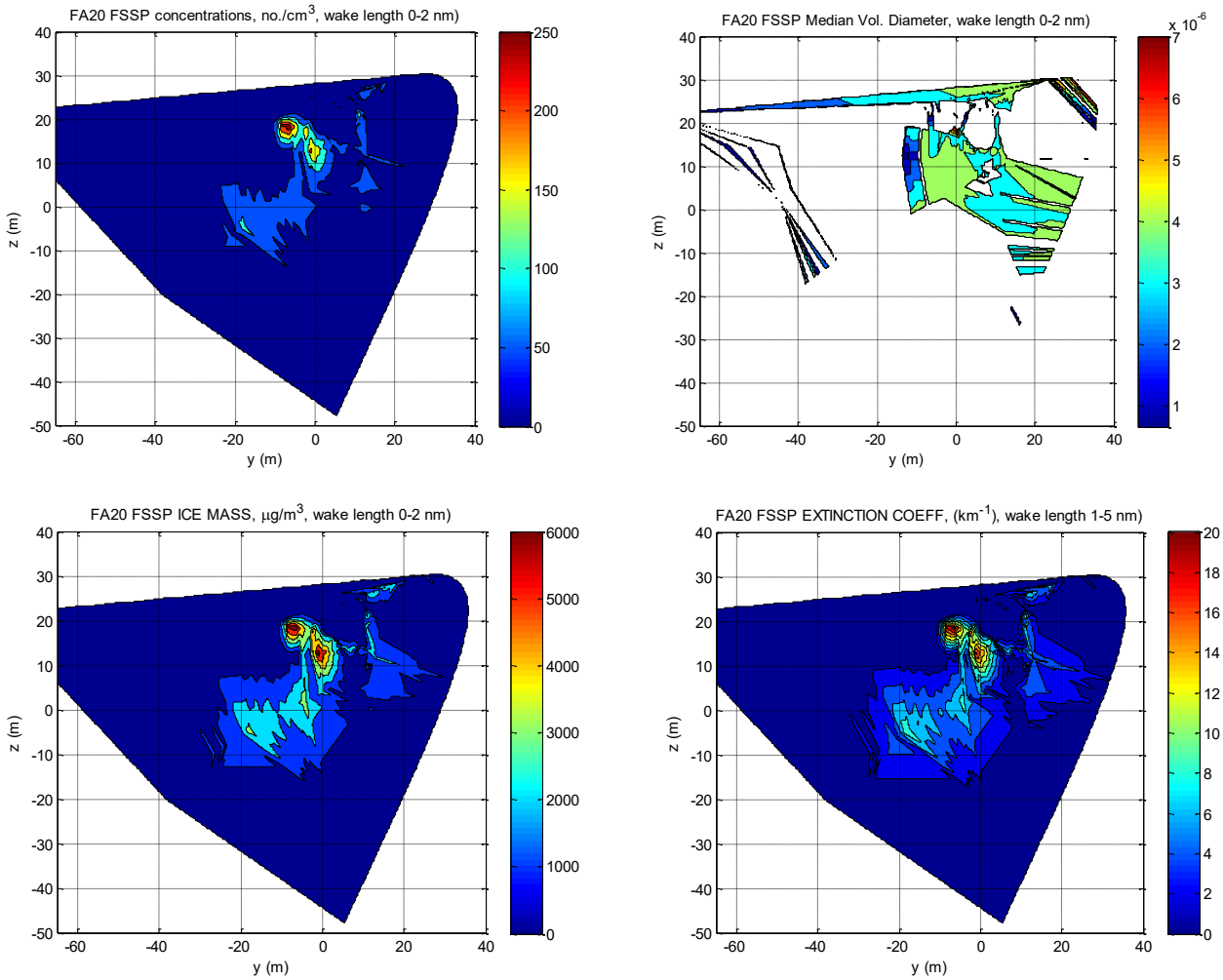

Figure 19 *CONTINUED* (*ABOVE*) – 100% LTPNNL example of contrail cross-sections, (*upper left*) ice particle number concentration (#/cc), (*upper right*), ice particle MVD (µm); (*lower left*), ice mass concentration (µg/m^3), (*lower right*), optical extinction (km^{-1}).

Classification: Unclass
Distribution: UNLIMITED

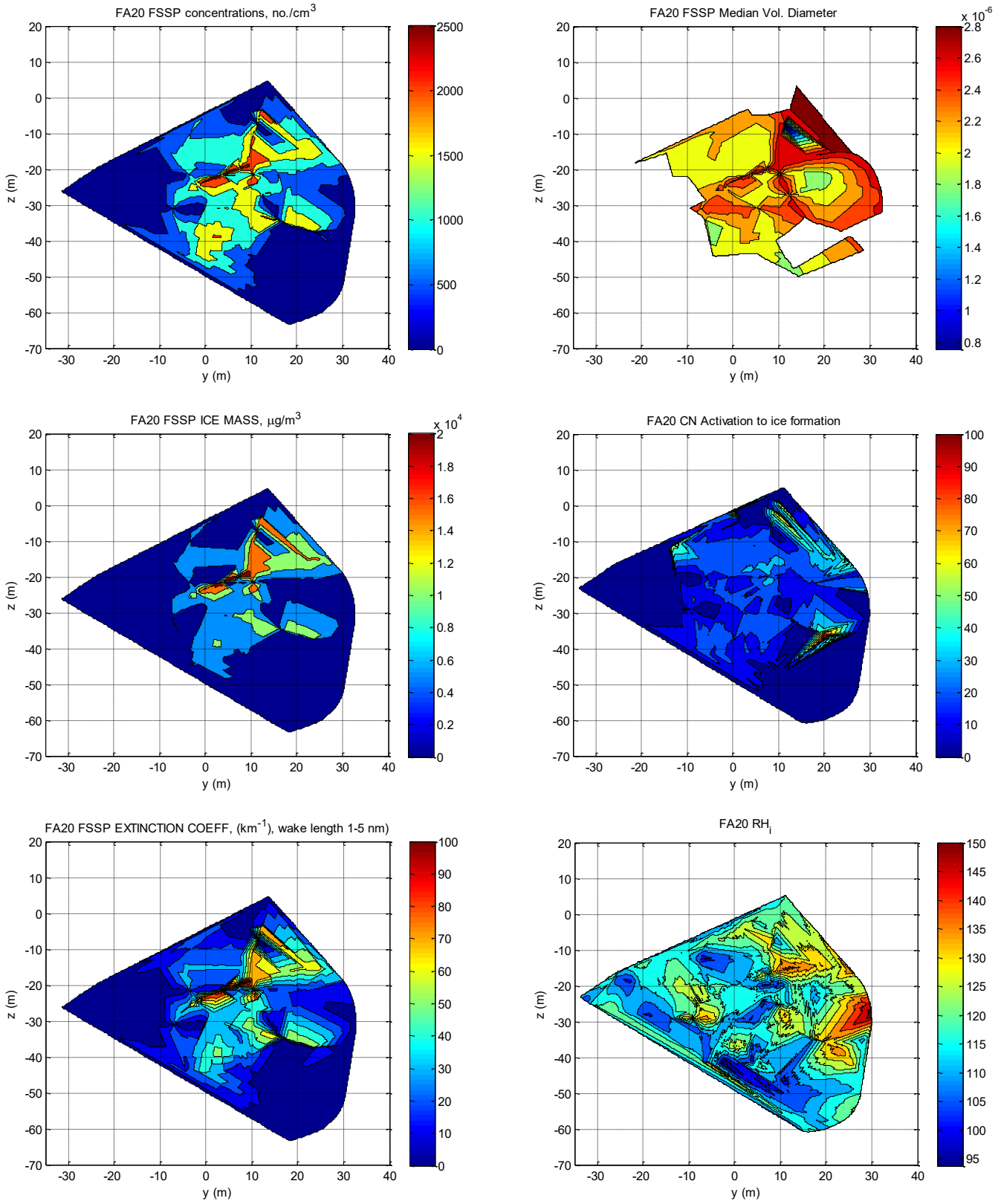

Figure 21 – 12th February flight, Jet A1 re-constructed contrail cross-sectional characteristics, c.8 nautical miles length (1.0 min. age): (*top left*) FSSP-100 ice particle number concentration (#/cc), (*top right*) ice MED (µm), (*middle left*) ice mass concentration (µg/m^3), (*middle right*), (*bottom left*), FSSP extinction coefficient (km^{-1}), (*bottom right*), approximate RHi (%).

Classification: Unclass
Distribution: UNLIMITED

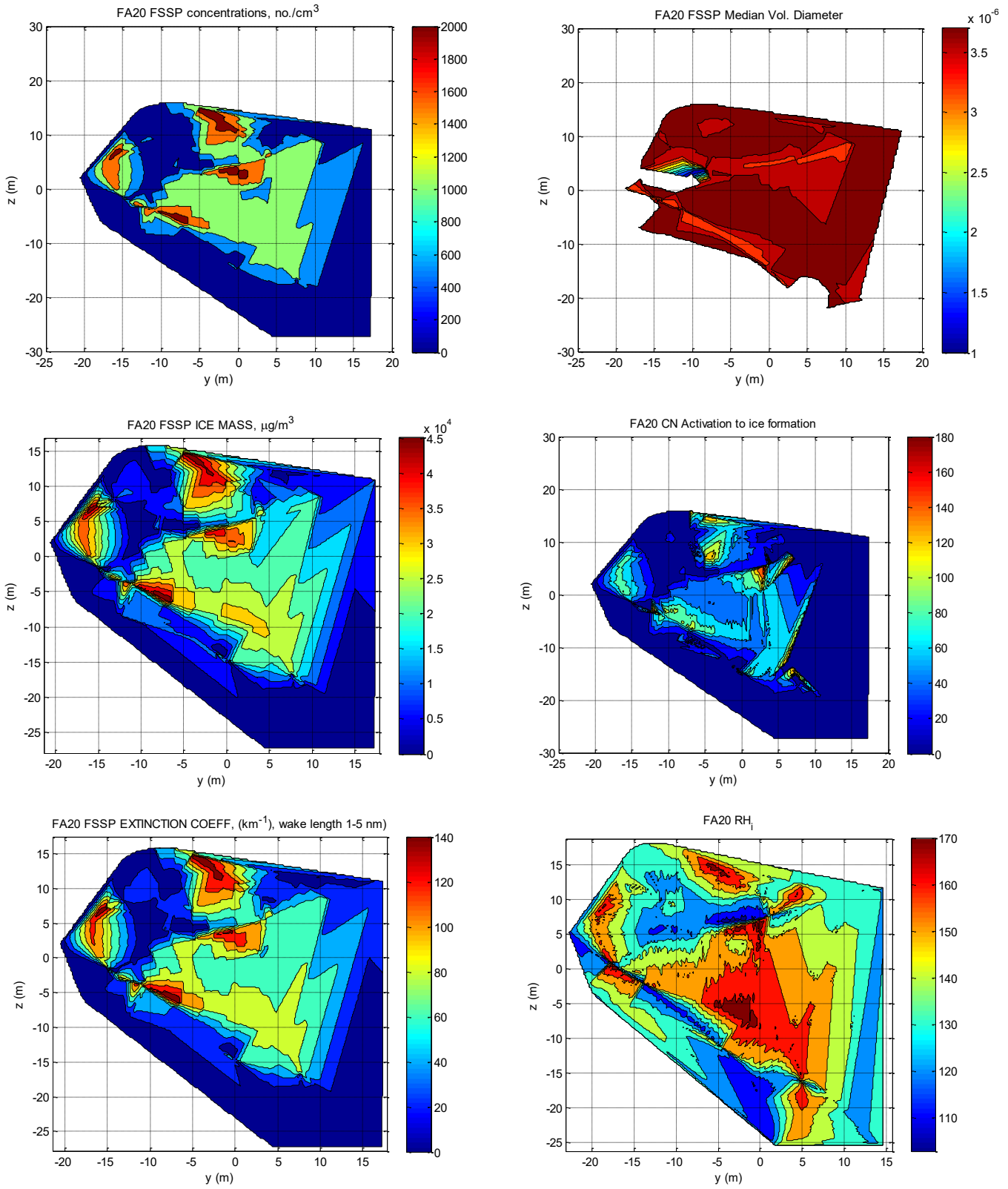

Figure 22– 12th February flight, 100% LTPNNL, re-constructed contrail cross-sectional characteristics, c.3 nautical miles length (0.4 min. age): (*top left*) FSSP-100 ice particle number concentration (#/cc), (*top right*) ice MED (µm), (*middle left*) ice mass concentration (µg/m^3), (*middle right*), apparent activation (for >0.5µm), FSSP#/cc / CM #/cc; (*bottom left*), FSSP extinction coefficient (km^{-1}), (*bottom right*), approximate RHi (%).

Classification: Unclass
Distribution: UNLIMITED

4.2.4 Contrail properties of apparent emissions indices of ice particle number, mass, the cross-sectional spectral-size median MED and integrated optical thickness over the whole contrail cross-section, for ice particles of >0.5 μm as sensed by the FSSP-100, are discussed in the following sections. CN activation data and distributions are presented and rationalised. Additional ice particle size and optical property information has been assembled and discussed.

4.2.5 Generally, the data is presented and discussed in terms of contrail age dependence. As discussed earlier (in relation to Figure 7), the atmospheric dependency is not quantified, rather only qualified by the categorisations of sublimating or persistent. Without atmospheric parametric corrections (*e.g.*, applied in **[3]** and **[4]**, due to the significant flight altitude/area differences in them between fuels), there can be expected to be some atmospheric-induced data scatter in contrail emission index ~ age plots.

4.3 Ice particle number FSSP-100 EIn

4.3.1 FSSP-100 EIn is presented in Figure 23. For the youngest cross-sections for each fuel (t ≈ 0.06 minutes, a contrail length of approximately 800 m, 48 wingspans), the mean EIn for sublimating and persistent contrails were similar, approximately $3_{10}{}^{13}$ for Jet A1 and $5_{10}{}^{12}$ for 100% LTPNNL. Sublimating and persistent contrail data subsets have been 1st order log-log regressed, showing sharp contrail age-referenced decay and growth, respectively.

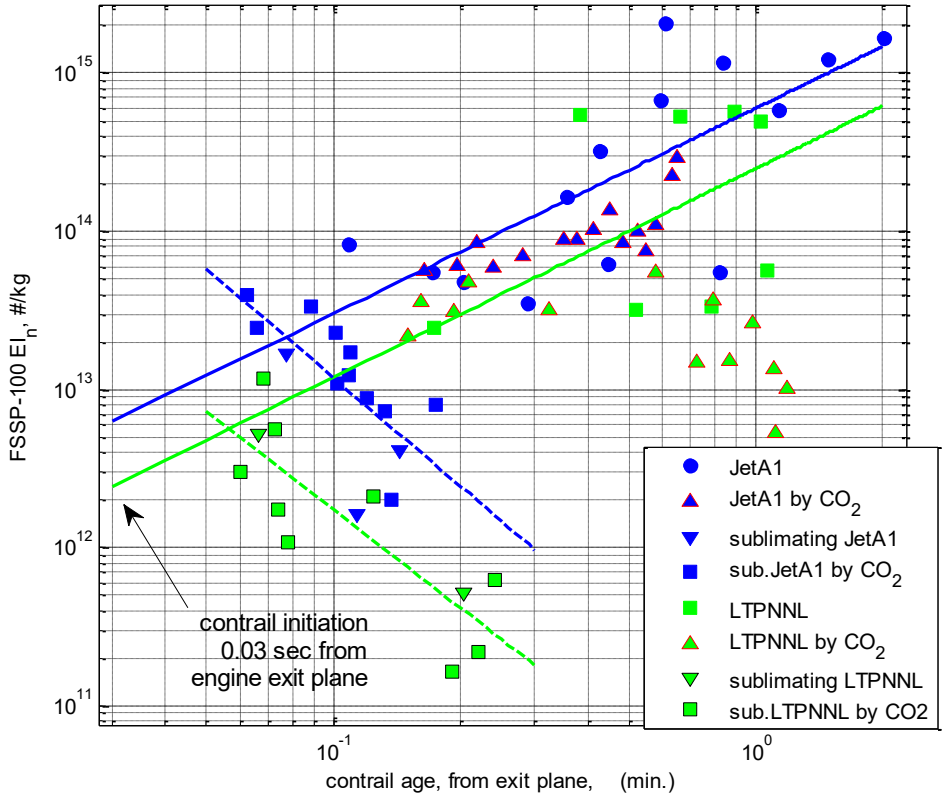

Figure 23 – contrail ice particle EIn characteristics with age, young contrails, for sublimating (dashed lines) and persistent (solid lines) contrails, Jet A1 & 100% LTPNNL fuels, wherefore EIn derived by cross-sectional plume re-construction & by CO_2 comparison; straight lines are log-log regressions to flight data points without corrections for variation in thrust & atmospheric parameters.

Classification: Unclass
Distribution: UNLIMITED

4.3.2 For persistent contrails, EIn growth rates were high, of log-log linear slope approximately 1.2 decades per time decade, similar for both fuels. However, the scatter around the log-log linear regression lines was significant. The atmospheric environmental differences between flights and spatiotemporal segments of each flight were introduced in Figure 7. It was observed that significant local variations were encountered, and that an apparent correlation between EIn and Ts was strong, especially for 100% LTPNNL. Data scatter for Jet A1 contrails generally was greater. Atmospheric parametric correlation also appeared to have been existent in the CN EIn data (Figure 15), notably in parameters affecting contrail growth, namely Ts, RHi and ∂RH/∂z (**[1][3][4]**). Furthermore, correlation between CN EIn and engine thermodynamic state (indicative of thrust, but much broader than the latter at high altitude). In order to reduce the persistent contrail data scatter of Figure 23, similar correlation and parametric influence identification was investigated for FSSP EIn. Due to lack of apparent correlation, with respect to Figure 7, ∂RH/∂z was not subsequently included as a parameter for FSSP EIn. This left the parameters of Ts, RHi, EGT and contrail age. Associations and suggested characteristic correlative functions are presented in Figure 24.

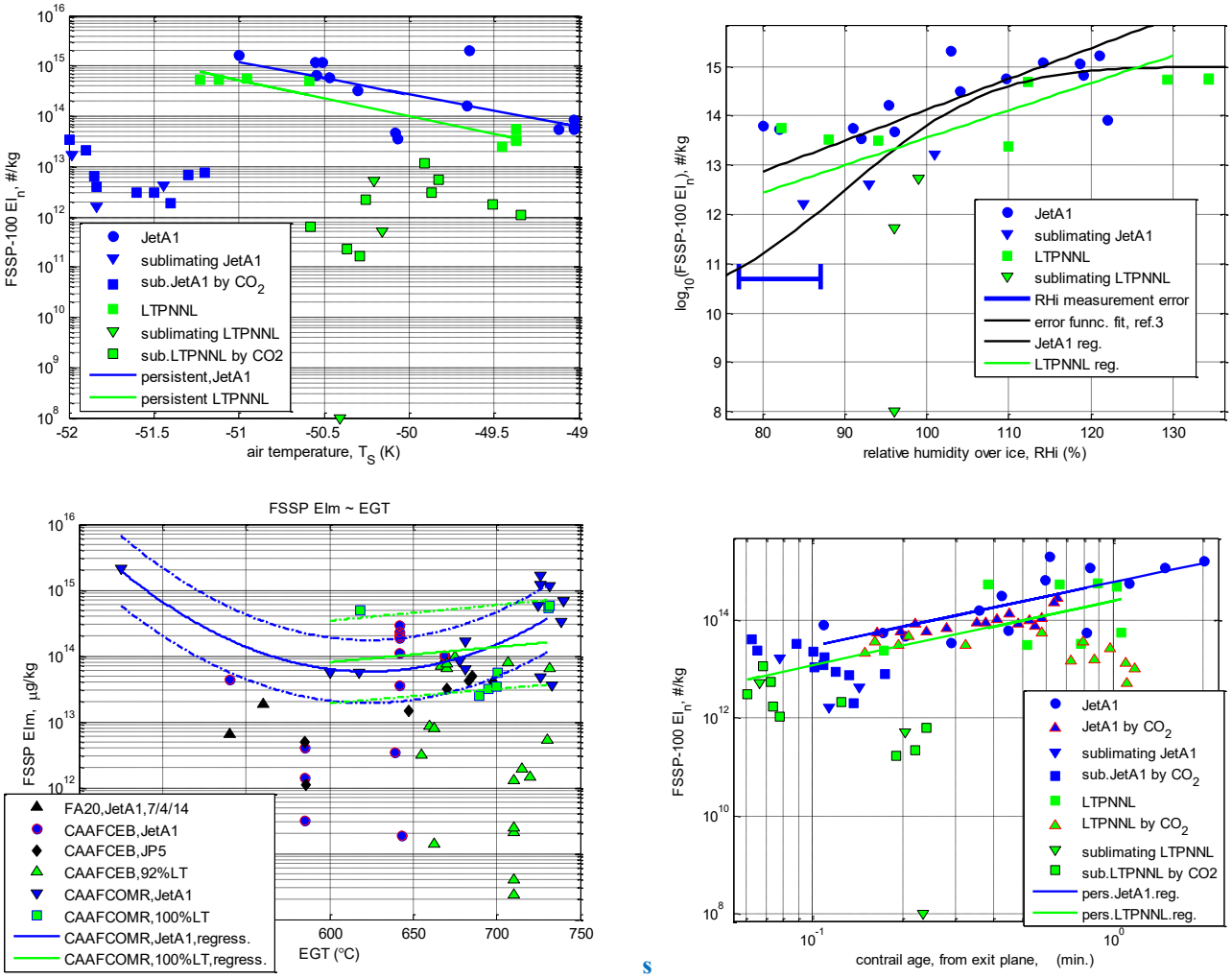

Figure 24 – multivariate analysis investigation for persistent contrail FSSP EIn, (*top left*) Ts, with log-linear regressive lines for each fuel, (*top right*) RHi, with earlier error-function and present linear regressive lines for each fuel, (*bottom left*) EGT, with wide-domain 2nd order regression ±σ for JetA1, 1st order ±σ for LTPNNL, (*bottom right*) contrail age with log-log 1st order regressions for each fuel.

Classification: Unclass
Distribution: UNLIMITED

4.3.3 Least squares (LS) multivariate regression fitting was then conducted for a characteristic-embodying, compound power-law model for each fuel

$$EIn = A\mathfrak{I}_1[Ts]^b\mathfrak{I}_2]RHi]^c\mathfrak{I}_3[EGT]^d\mathfrak{I}_4[age]^e,$$

wherefore the functional characteristic equations

$\mathfrak{I}_1[Ts] = m_1Ts + c_1$, for each fuel

$\mathfrak{I}_2]RHi] = m_2RHi + c_2$ for each fuel

$\mathfrak{I}_3[EGT] = m_3EGT^2 + n_3EGT + c_3$. for JetA1,

$\mathfrak{I}_3[EGT] = m_3EGT + c_3$, for 100% LTPNNL, and

$\mathfrak{I}_4[age] = m_4\,age + c_4$, for each fuel

are derived by univariate parametric regression as shown in Figure 24, and the unknown vector [A b c d e] then solved by LS residual identification, using the Matlab® '\' operand, of the logarithmic linearized matrix form of the compound power-law, for 'j' contrail plume cross-sectional data points:

$$log\begin{bmatrix} lEIn_1 \\ EIn_2 \\ : \\ : \\ EIn_j \end{bmatrix} = \log A\begin{bmatrix} 1 \\ 1 \\ : \\ : \\ 1_j \end{bmatrix} + b\left\{log\begin{bmatrix} Ts_1 \\ Ts_2 \\ : \\ : \\ Ts_j \end{bmatrix}\right\} + c\left\{log\begin{bmatrix} RHi_1 \\ RHi_2 \\ : \\ : \\ RHi_j \end{bmatrix}\right\} + d\left\{log\begin{bmatrix} EGTi_1 \\ EGTi_2 \\ : \\ : \\ EGTi_j \end{bmatrix}\right\} + e\left\{log\begin{bmatrix} age_1 \\ age_2 \\ : \\ : \\ age_j \end{bmatrix}\right\}$$

vectorised as

$$log\begin{bmatrix} lEIn_1 \\ EIn_2 \\ : \\ : \\ EIn_j \end{bmatrix} = [\ \log A\ b\ \ c\ \ d\ e\ ]\begin{bmatrix} 1 & 1 & \cdots & \cdots & 1_j \\ log(Ts_1) & log(Ts_1) & \cdots & \cdots & log(Ts_j) \\ \log(RHi_1) & \log(RHi_1) & \cdots & \cdots & \log(RHi_j) \\ log(EGT_1) & log(EGT_1) & \cdots & \cdots & log(EGT_j) \\ log(age_1) & log(age_1) & \cdots & \cdots & log(age_j) \end{bmatrix}$$

So that

$$[\ \log A\ b\ \ c\ \ d\ e\ ] = \begin{bmatrix} 1 & log\begin{bmatrix} Ts_1 \\ Ts_2 \\ : \\ : \\ Ts_j \end{bmatrix} & log\begin{bmatrix} RHi_1 \\ RHi_2 \\ : \\ : \\ RHi_j \end{bmatrix} & log\begin{bmatrix} EGTi_1 \\ EGTi_2 \\ : \\ : \\ EGTi_j \end{bmatrix} & log\begin{bmatrix} age_1 \\ age_2 \\ : \\ : \\ age_j \end{bmatrix} \\ 1 & & & & \\ : & & & & \\ : & & & & \\ 1_j & & & & \end{bmatrix} \backslash log\begin{bmatrix} lEIn_1 \\ EIn_2 \\ : \\ : \\ EIn_j \end{bmatrix}$$

The solved compound power-laws, for each of JetA1 and LTPNNL, have been applied to the data points in Figure 25, to derive two paired sets of corrected EIn for MCT and LRC engine thrust conditions, namely EGT, 724°C and 680°C, respectively. It is seen that the MCT and LRC reference thrust EIn points (for Ts = -50°C, RHi≈100% and t=1 min. age) were interpolated amidst the linearized data points.

4.3.4 As seen in Figure 25, the compound product power-law model was successful in linearizing the contrail cross-section EIn data sub-sets for each fuel, for local spatiotemporal

Classification: Unclass
Distribution: UNLIMITED

variations in atmospheric condition (Ts and RHi), in engine thermodynamic state (EGT) and contrail age, with log standard deviations σ of 1.8% for Jet A1 and 0.5% for LTPNNL.

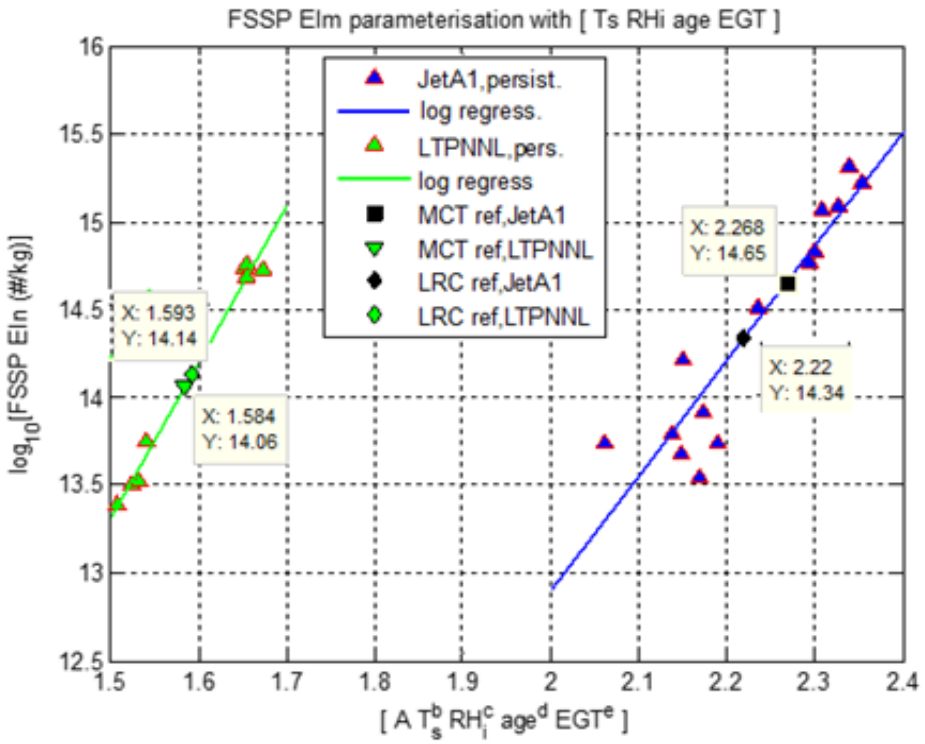

Figure 25 – identification of the compound product power-law of characteristic functions, for each of JetA1 and LTPNNL fuels, with 1st order log-linear fits to the power-law data sub-sets, thence corrected EIn values, for each of two reference condition vectors, Max Continuous Thrust and Long Range Cruise EGT, 724°C and 680°C respectively, for [Ts RHi age] = [-50°C 100% 1_minute], in each case.

4.3.5 For any state vector [Ts RHi EGT age]$_i$ the corrected EIn$_i$ could thus be calculated from the power-law linearization. Figure 26 includes the corrected EIn$_i$ for [Ts RHi EGT age]$_i$ = [-50°C ≈100% 724°C], *i.e.* MCT, for contrail ages of 0.05 to 3 minutes (although a time extrapolation from 2 to 3 min. age, comparison between Figure 25 and Figure 26 indicates that the points were product-power-law interpolation points). By comparing to Figure 23, it is seen that the corrected EIn$_i$ characteristics provided a different view to the raw data; namely, at generation the LTPNNL EIn$_i$ was greater than that for JetA1, but grew more slowly, to be less for contrail age > 0.1 min., as shown below, a mean value of 87% (uncertainty range 72%-94%) lower for LTPNNL *c.f.* JetA1, for a contrail age of 3 minutes (25 nautical mile long contrail).

Fuel	*contrail age for MCT engine operation, ±1σ for each fuel data-set*		
	contrail generation 0.06 minutes	*1 minute*	*3 minutes*
JetA1	$2.4_{10}{}^{13(1\pm0.018)}$	$4.47_{10}{}^{14(1\pm0.018)}$	$1.41_{10}{}^{15(1\pm0.018)}$
100% LTPNNL	$3.4_{10}{}^{13(1\pm0.005)}$	$1.14_{10}{}^{14(1\pm0.005)}$	$1.8_{10}{}^{14(1\pm0.005)}$
LTPNNL/JetA1	**1.45**(-0.71/+1.35)	**0.26**(-0.14/+0.27)	**0.13**(-0.07/+0.15)

Classification: Unclass
Distribution: UNLIMITED

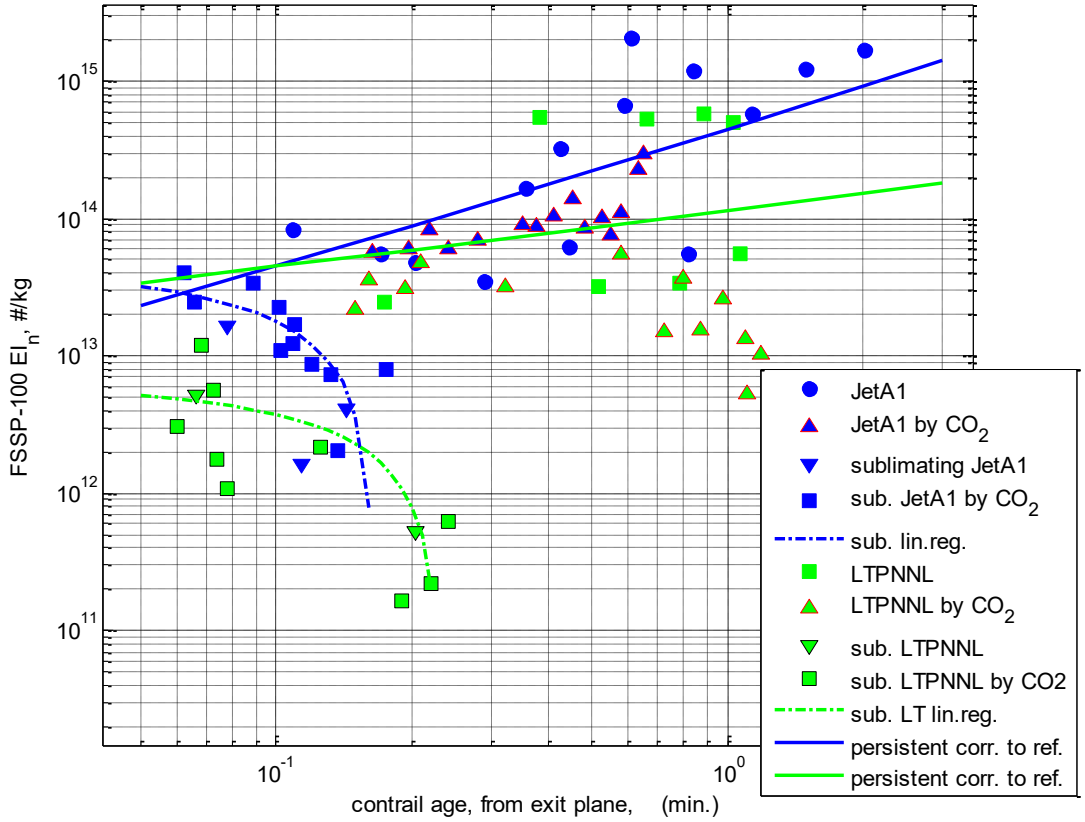

Figure 26 – plots of JetA1 (*sold-blue line*) and LTPNNL (*solid-green line*) EIn, corrected to [Ts RHi EGT] = [-50°C 100% 724°C], *i.e.* MCT, against contrail age.

4.4 Spherical ice mass EIm

4.4.1 Contrail spherical EIm is presented in Figure 27. For the sublimating contrails of the 20th August 2019, there was negligible difference in ice mass between fuels. For the persistent contrails of the 29th August 2019 and 12th February 2020, there appeared to be similar ice-mass growth rates for JetA1 and LTPNNL, with increasing contrail age, but as with EIn, considerable scatter is seen for both fuels, due to atmospheric and engine operation variations. An example to highlight in Figure 27 were the data points for LTPNNL, above and below the regression ('mean') line for contrail ages 0.5-1 minute.

4.4.2 Thus, to reduce data scatter, atmospheric, engine state and contrail age modelling was conducted in the same manner as for EIn. The correlative functional relationships between EIm and [Ts RHi EGT age] are illustrated in Figure 28, the power-law [A b c d e] identifications in Figure 29, and the [-50°C ≈100% MCT] referenced EIm ~ age data in Figure 30. Accurate linearization was obtained for LTPNNL, with a log standard deviation of 0.76%; a less accurate log σ of 4% for Jet A1.

4.4.3 Comparing the modelled reference EIm ~ age data of Figure 30 to the uncorrected flight data of Figure 27, it is seen that the age related trends and offsets near generation were changed significantly – the ice-mass for LTPNNL was increased somewhat and the trend with age reduced, whilst JetA1 EIm was reduced significantly and the trend with age increased. Opposed to this, in the uncorrected flight data (Figure 27) the extrapolated limits

Classification: Unclass
Distribution: UNLIMITED

of EIm at generation converged to similar values for persistent and sublimating contrails, within the range of 500-800 g/kg.

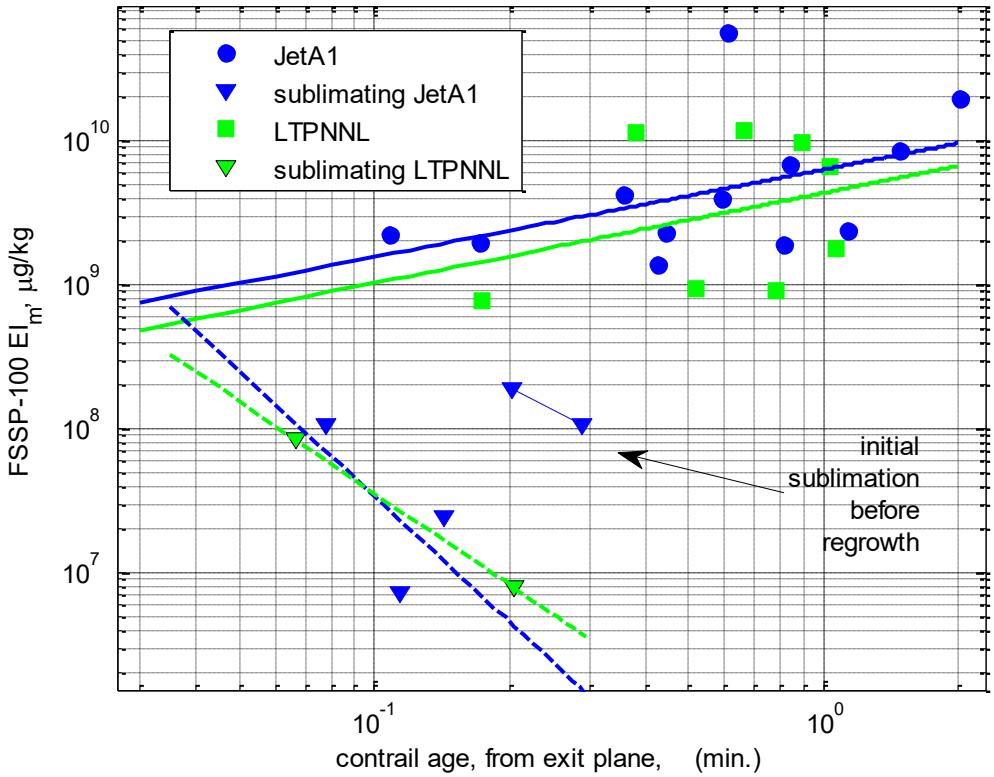

Figure 27 – contrail EIm, derived by spherical integration of ice particle size ~ concentration spectra, with 1st order log-log regressive fits to sublimating and persisting contrail data.

4.4.4 Of the changes to contrail ice particle growth, it is considered probable that JetA1 had the greater inaccuracy in EIm (but not necessarily EIn) because of contrail sublimation and re-growth dynamics. The modelling accuracy would have been reduced by such dynamics of the 12th February JetA1 contrail. For both fuels, the ice sphericity assumption introduced ice-mass error, for any crystallisation that occurred **[20]**. However, the uncertainty would appear to have been greater near generation, as discussed. The table below records the modelled EIm data for MCT, as well as uncorrected data at one minute age.

Fuel **EIm contrail values, µg/kg**	**Modelled contrail age, MCT engine operation in -50°, RHi≈100%**			
	contrail generation 0.05 min	**1 minute**		**3 minutes**
		modelled	**Non-corrected for atmos. variations**	
JetA1	$0.19_{10}{}^{9(1\pm0.04)}$	$7.77_{10}{}^{9(1\pm0.04)}$	$6.39_{10}{}^{9}$	$3.60_{10}{}^{10(1\pm0.04)}$
100% LTPNNL	$1.61_{10}{}^{9(1\pm0.0076)}$	$2.98_{10}{}^{9(1\pm0.0076)}$	$4.43_{10}{}^{9}$	$3.75_{10}{}^{9\ (1\pm0.0076)}$
LTPNNL/JetA1	**8.4**(-5.2/+14.2)	**0.38**(-0.24/+0.64)	**0.69**	**0.10**(-0.06/+0.18)

Classification: Unclass
Distribution: UNLIMITED

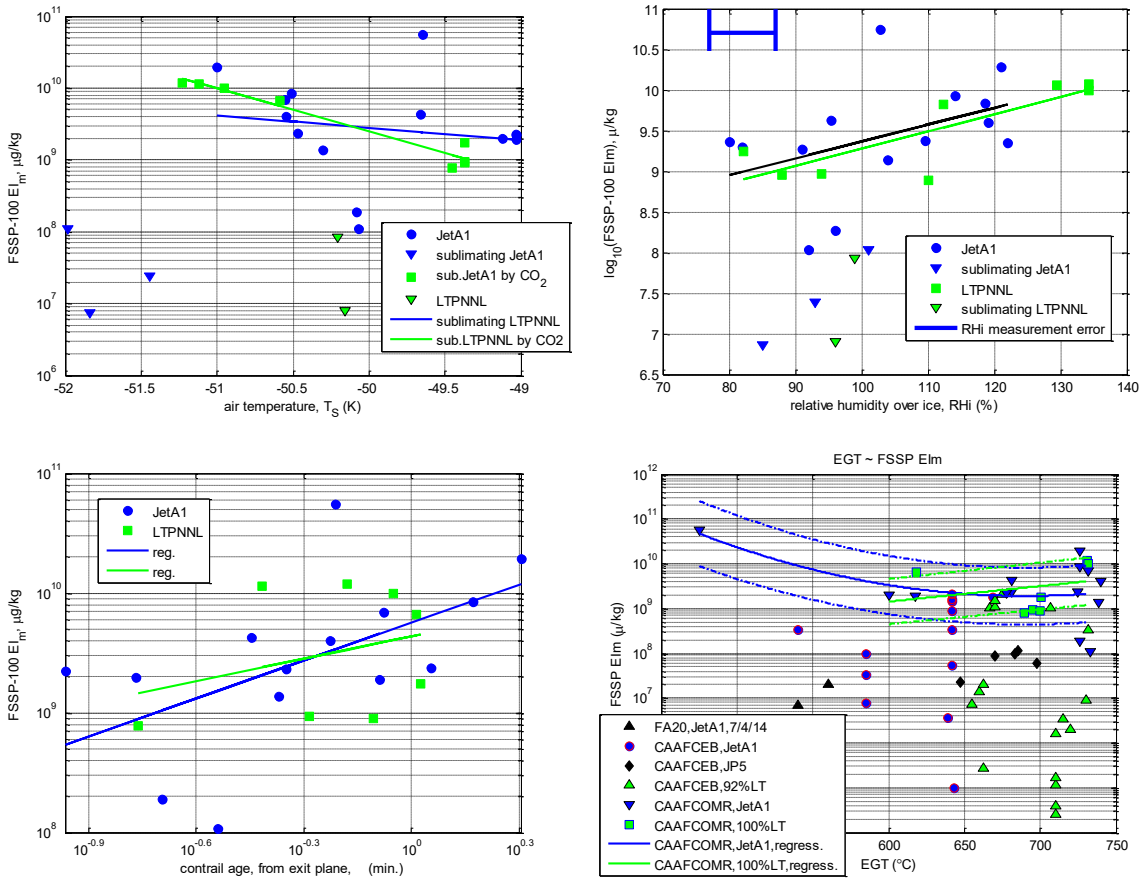

Figure 28 – identification of the correlative functional relationships, for each of JetA1 and LTPNNL fuels, with 1st order log-linear fits to the power-law data sub-sets, thence corrected EIn values, for each of two reference condition vectors, Max Continuous Thrust and Long Range Cruise EGT, 724°C and 680°C respectively, for [Ts RHi age] = [-50°C 100% 1_minute], in each case.

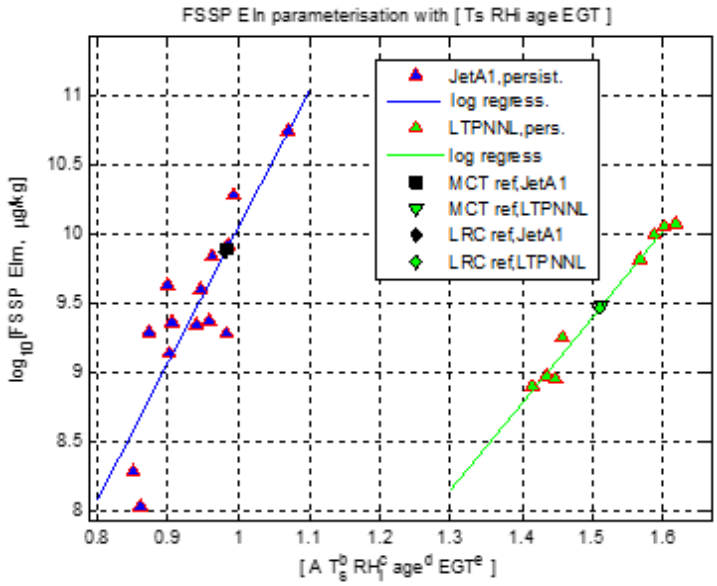

Figure 29 – identification of the EIm product power-law of characteristic functions, for each fuel, with 1st order log-linear fits to the power-law data sub-sets, thence corrected EIm values, for each of two reference condition vectors, MCT & LRC for [Ts RHi age] = [-50°C 100% 1_minute[.

Classification: Unclass
Distribution: UNLIMITED

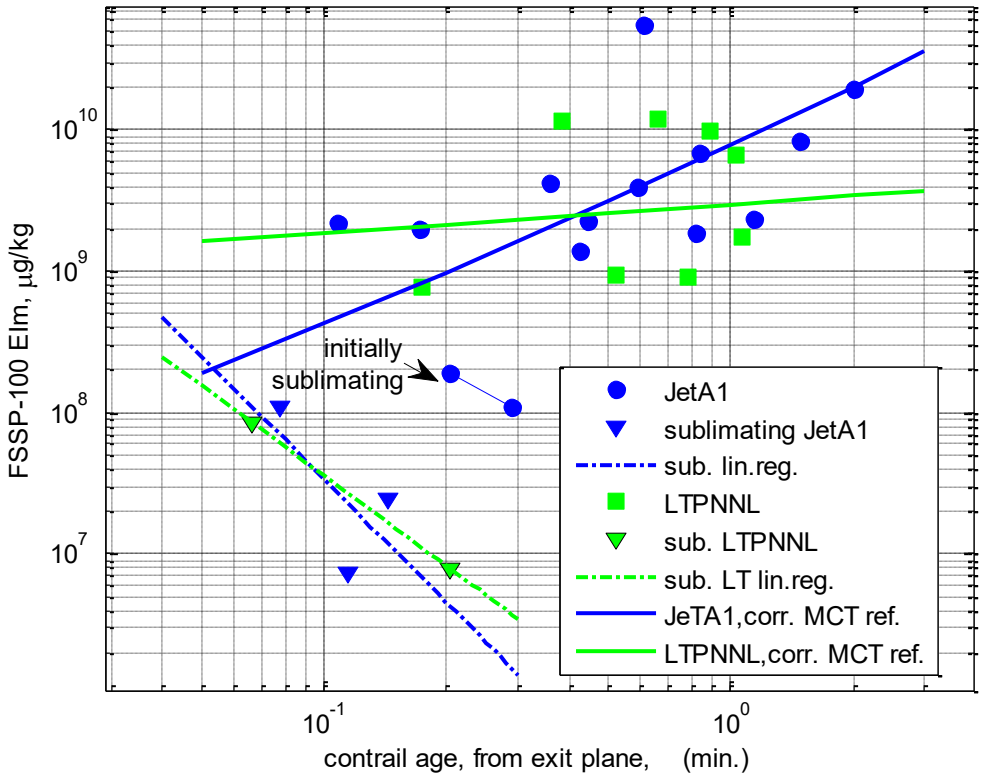

Figure 30 – plots of JetA1 (*sold-blue line*) and LTPNNL (*solid-green line*) EIm, corrected to [Ts RHi EGT] = [-50°C 100% 724°C], *i.e.* MCT, against contrail age.

4.5 Ice particle size, spectral MED

4.5.1 Concerning contrail ice particle size, plume cross-sectional median spectral MED (medMED) is presented in Figure 31. Annotations highlighted the association of differences between median values with air temperature – larger values for warmer air temperatures. This correlation is observed in the medMED ~ Ts plots of Figure 32.

4.5.2 By reference to Figure 31, it is seen that contrail sublimation was accompanied by rapid reductions in ice particle sizes. The JetA1 contrail of the 12th February experienced sublimation, followed by spatiotemporal re-growth. From generation to 0.3 minutes age, sublimation rapidly reduced median MED from ≈4 µm to ≈2 µm, with uneven size re-growth rates thereafter.

4.5.3 The rearwards-extrapolations to LTPNNL contrail origin match, for sublimating and persistent contrails, to a medMED value of 4.6 µm, greater than 3.8 µm for Jet A1. By one minute age, the sizes were reversed, for the two fuels, respectively. The overall mean values of the medMED data-sets were similar for the persistent contrails, 4.0 µm for Jet A1, 4.0 µm for LTPNNL.

4.5.4 1st order regression for the 29th August JetA1 contrail suggested non-monotonic size growth from generation. All LTPNNL contrails appeared to be accompanied by reductions in medMED with increasing age (although EIn increased with age, Figure 26).

Classification: Unclass
Distribution: UNLIMITED

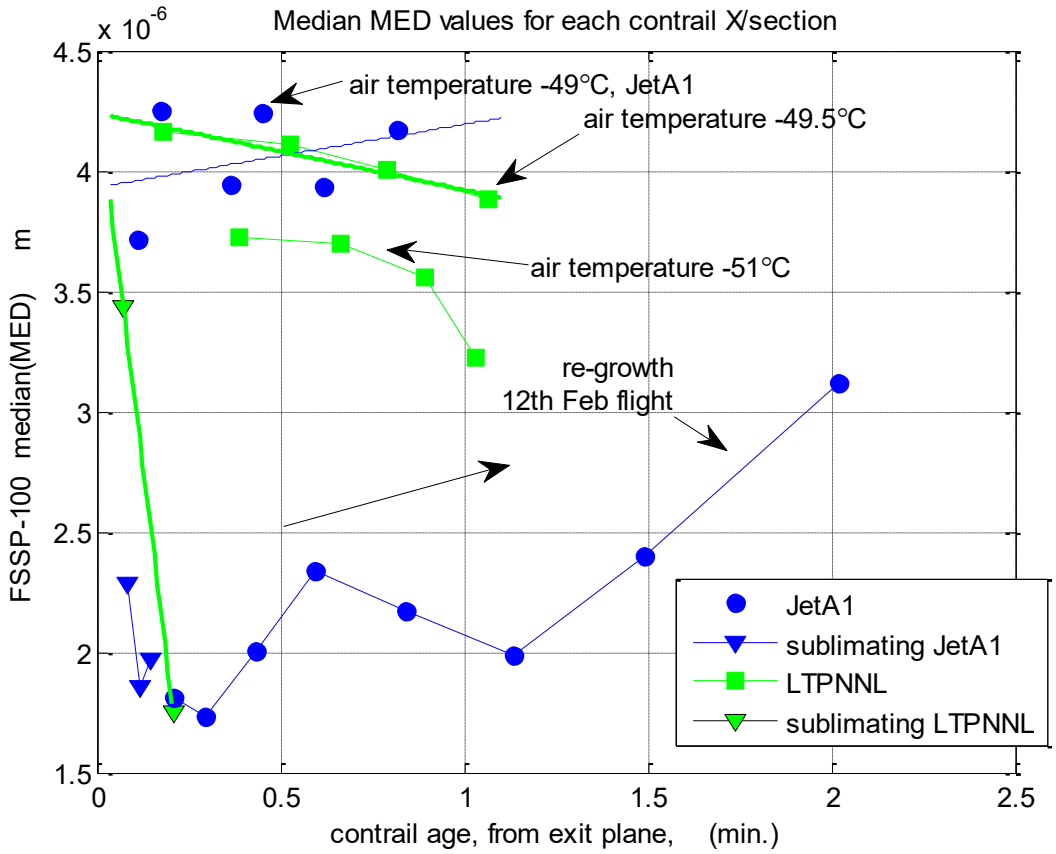

Figure 31 – contrail ice particle median sizes of spectral MED for each plume cross-section, annotated with air temperatures, & highlighting the spatiotemporal re-growth of the JetA1 contrail of the 12th February 2020 flight.

4.5.5 Parametric identification of power-law models for medMED were conducted in similar manner to that for EIn and EIm. The results are seen in Figure 32. The power-law linearization process was quite successful for LTPNNL (with a log σ of 1.4%), but unsuccessful for JetA1, requiring a 2nd order regression for the latter, with considerable residual scatter, a log σ of 17.2%. Complicating the identification process for JetA1 was the existence of non-monotonic contrail states, in particular the sublimating-then-regrowth contrail of the 12th February flight.

4.5.6 The corrected data (to -50°≈100%, MCT) is shown in Figure 33. It is seen that the identification process for JetA1 resulted in an estimate of size growth for the reference contrail medMED, which lay between the two persistent cases measured for JetA1, with a weighting towards the greater number of data points (*i.e.*, the 12th February 2020 flight case). On the other hand, the LTPNNL contrails were modelled accurately, and showed size contractions with ageing.

Classification: Unclass
Distribution: UNLIMITED

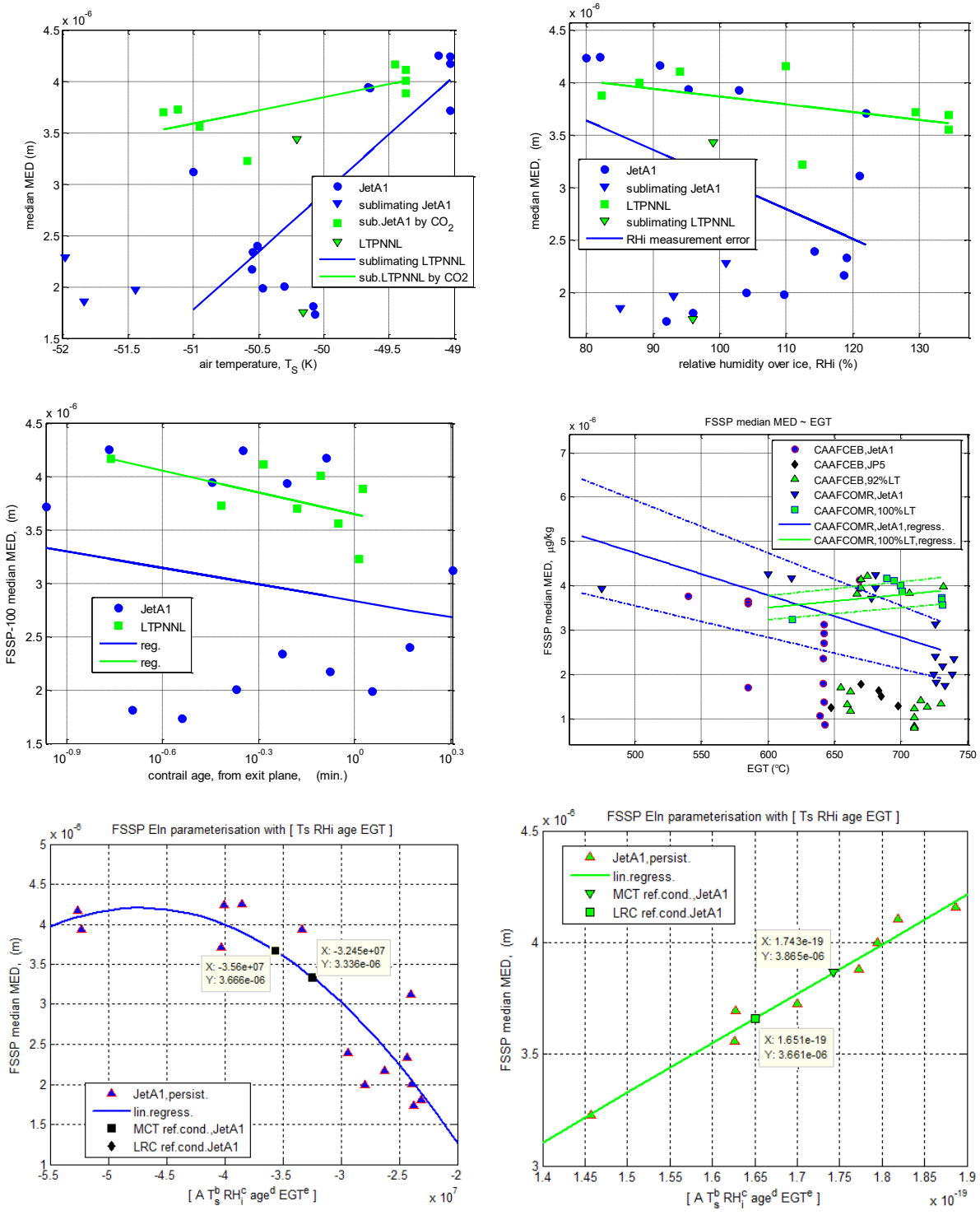

Figure 32 – correlations between cross-sectional median values of spectral MED and Ts, RHi, contrail age and engine EGT, and power-law identifications: (*top left*) Ts, (*top right*) RHi, (*middle left*) contrail age, (*middle right*) engine EGT, (*bottom left*) JetA1 power-law with 2nd order regression, and (*bottom right*) LTPNNL power-law with 1st order regression.

Classification: Unclass
Distribution: UNLIMITED

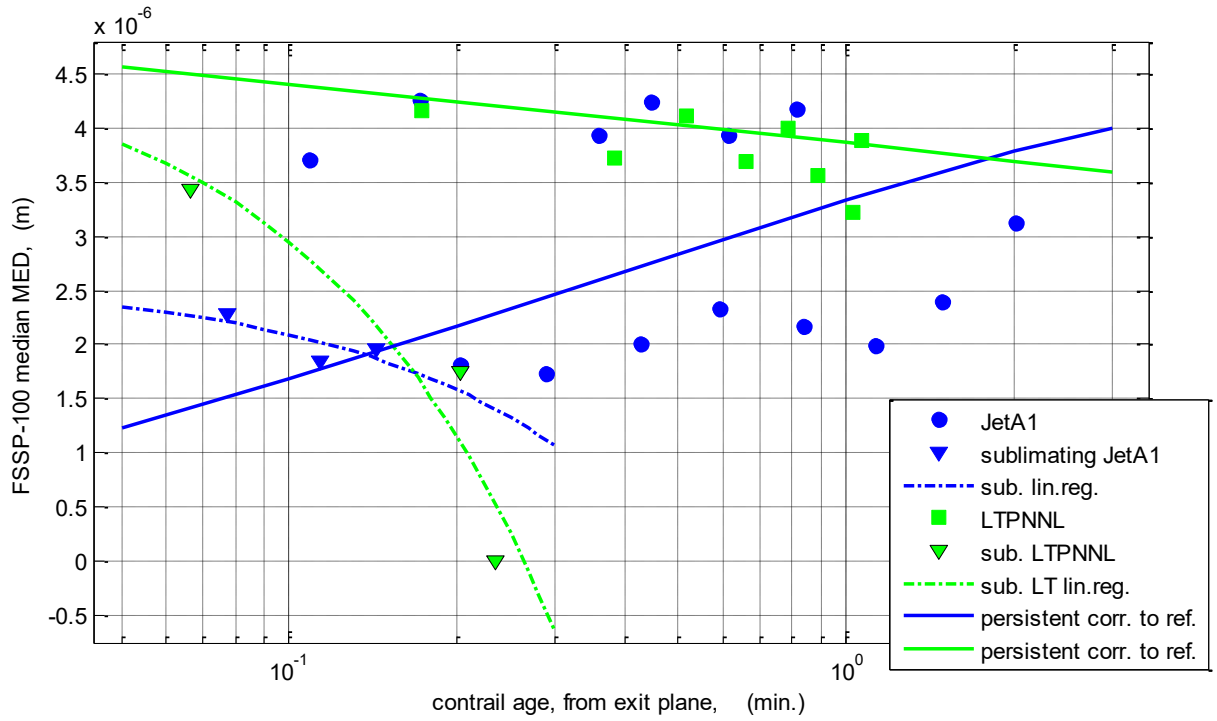

Figure 33 – *t*he power-law smoothed contrail medMED characteristics for MCT, Ts -50°C, RHi ≈100%, with increasing contrail age, for JetA1 (*solid blue line*) and LTPNNL (*solid green line*).

4.6 Ice particle size variation & contrail dynamics

4.6.1 medMED is a bulk ice particle size parameter. As shown in Figure 16 to Figure 22, spectral MED typically varied across the contrail cross-sections – typically for JetA1, but on spatiotemporal occasions, negligibly for LTPNNL (notably, the 12th February flight, Figure 22). To examine this further, the spatiotemporal traces for this flight are presented in Figure 34 for JetA1 and LTPNNL, showing the general trends of size increase and decrease, respectively.

4.6.2 In addition to the general trends, the JetA1 trace displayed typical variation (observed as a waveform 'unsteadiness'), whilst the LTPNNL trace displayed generally, much less variation in value. The maxima and minima values for each plume (shown in Figure 35) highlighted this. For JetA1, maxima and minima frequently covered the full bin size range (from 0.5 to 7.5 µm for the lowest size range, which the FSSP-100 was operated on), indicating registrations in all bins.

4.6.3 For LTPNNL, for age 0.5-0.8 minutes, the maxima MED did not vary and were very close to the median MED values. Little difference between maximum and median MED values, implied spatial homogeneity and temporal stability. This was in accordance with the spatial homogeneity of the MED contour plot for a period of the LTPNNL contour on the 12th February 2020 flight, shown in Figure 22.

Classification: Unclass
Distribution: UNLIMITED

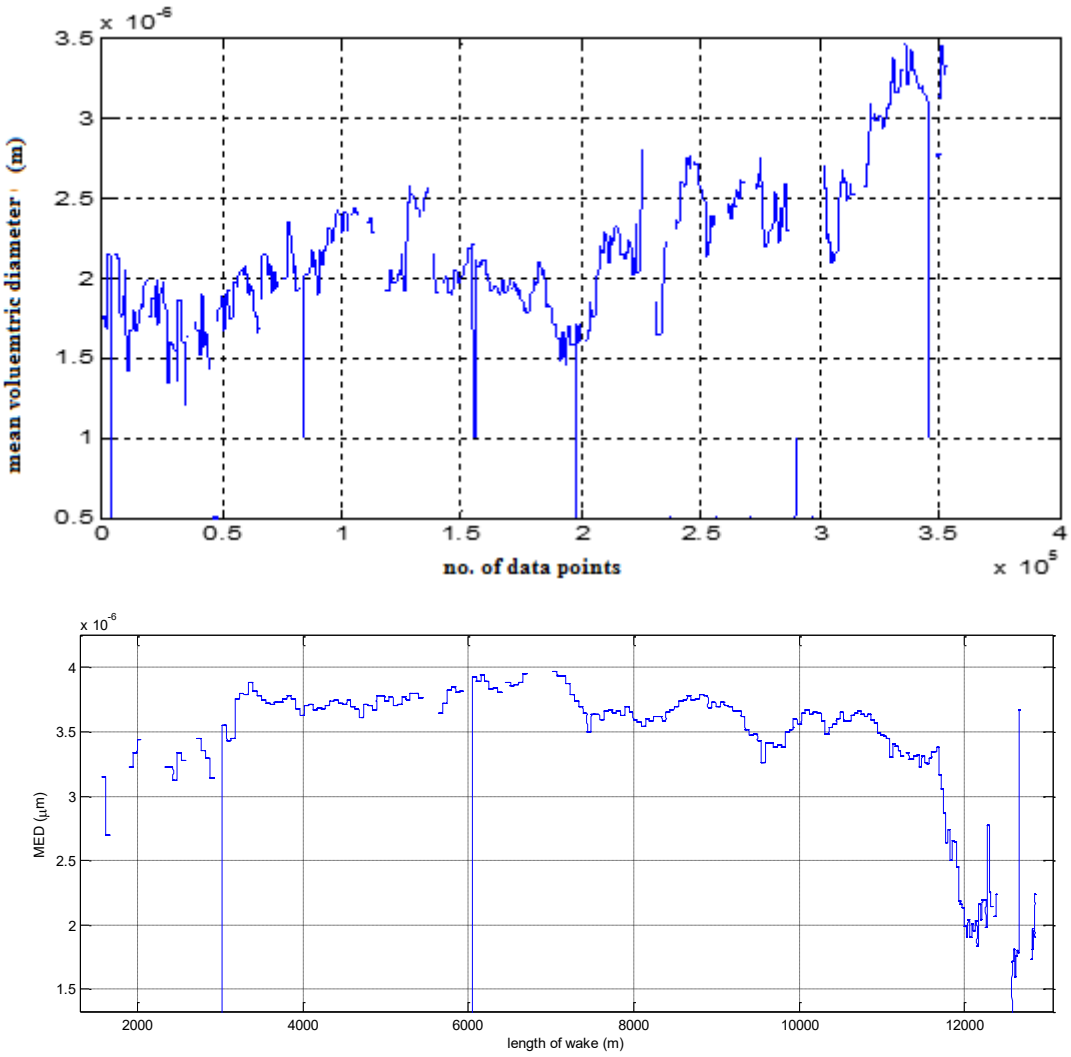

Figure 34 – spatiotemporal traces of FSSP spectral MED (smallest size measurement scale), in 12th February 2020 contrails: (*top*) JetA1, (*bottom*) LTPNNL.

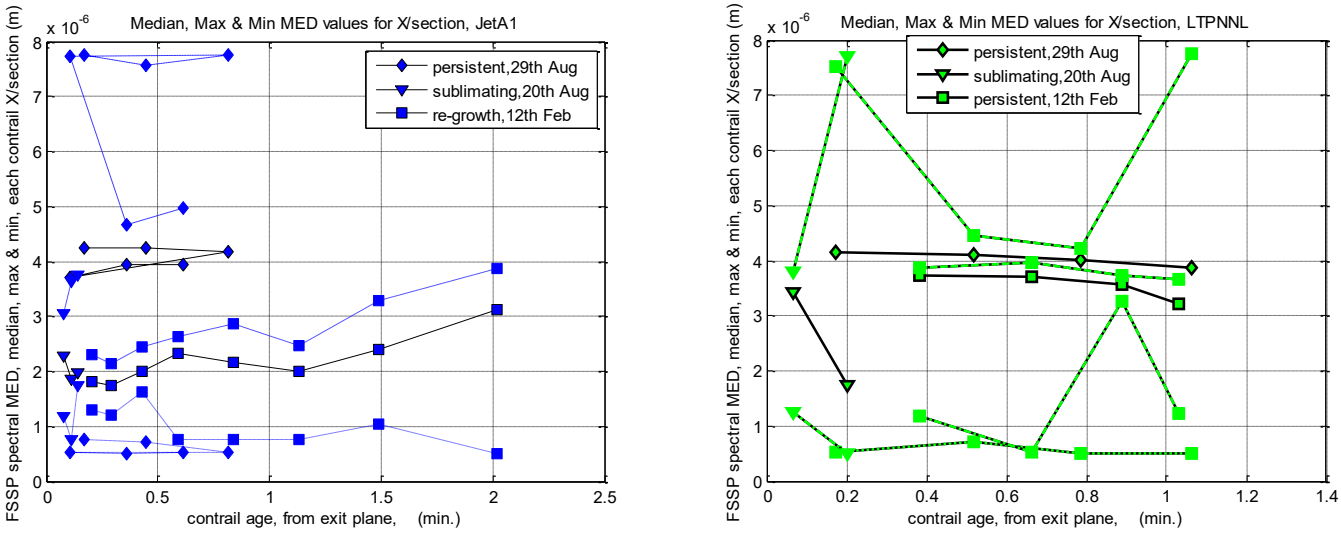

Figure 35 – median MED with maxima and minima included for each cross-section, (*left*) JetA1, (*right*) 100% LTPNNL.

Classification: Unclass
Distribution: UNLIMITED

4.7 Optical depth

4.7.1 Optical extinction has been calculated from FSSP-100 spectra using the method of Ref. **[6].** It differed widely across the contrail cross-section, as did all contrail properties. The contrail cross-sectional plots of extinction contours (see, for example, those contained in Figures 16 to 21), wherein contour values as high as 150 km^{-1} were indicated) were integrated in [y z] directions m^{-1} line of flight (LOF) direction and presented in as optical EIo values. The sublimating contrails thinned rapidly. Persistent contrails increased in optical thickness gradually. For the persistent contrail datasets without corrections, overall mean EIo were, for Jet A1, 2.75e+04 $km^{-1}m^2$ and for LTPNNL, 1.79e+04 $km^{-1}m^2$, a reduction of 35%.

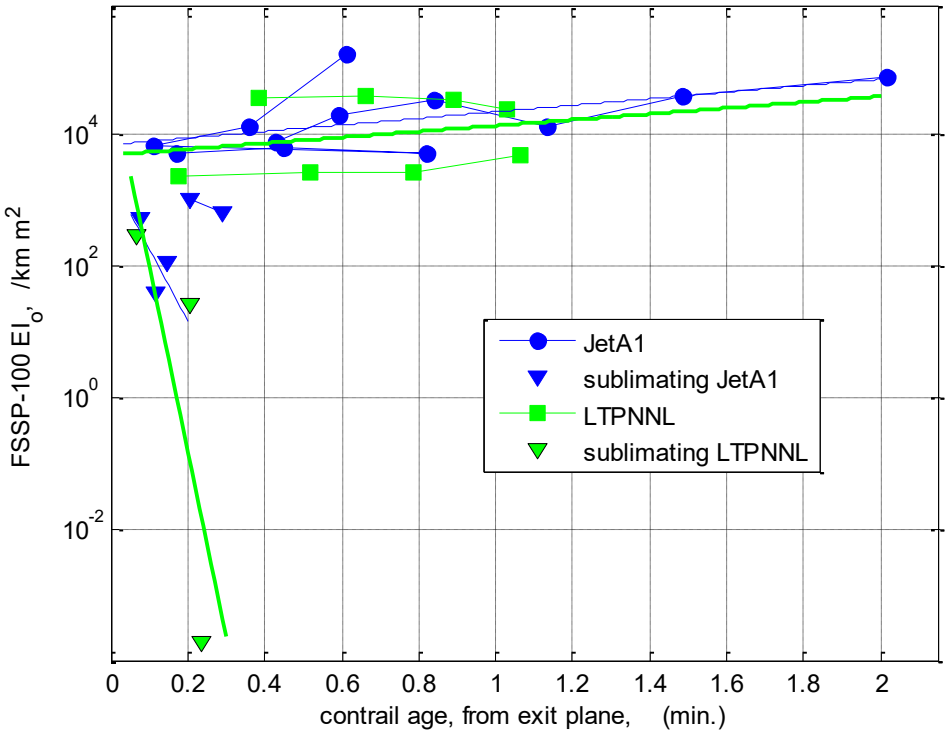

Figure 36 – CAAFCOMR flights, contrail cross-sectional integrated optical extinction coefficient for FSSP-100 spectra, EIo [4].

4.7.2 EIo was corrected to reference conditions, using the same technique as for previous contrail parameters, employing the functional characteristics shown in Figure 37. The optical associations tended to be strong in each case, unlike EIm and medMED, wherefore sensitivity to contrail history, dynamics and probable crystallisation was displayed, resulting in obscure correlations. However, in the case of optical parameters, EIo increased with colder air, increased with RHi, and grew with contrail age.

4.7.3 Identified power-laws were applied to JetA1 and LTPNNL, Figure 38. As previously, linearization for LTPNNL was excellent (a log σ of 1.9%) scatter was greater for JetA1 (a log σ of 9.2%). The two reference power conditions, LRC and MCT were extracted. The corrected contrail age effects for MCT were then plotted for JetA1 and LTPNNL, in Figure 39. At generation, the integrated optical extinction EIo ($km^{-1}m^2/kg$) is seen to have been greater for LTPNNL, but grew little with contrail age, whereas that for JetA1 grew

Classification: Unclass
Distribution: UNLIMITED

significantly, to be greater for contrail age >0.5 minutes. Extrapolated to 3 min. age, LTPNNL EIo was $(1.16\pm0.22)_{10}{}^4/(7.8\pm0.7)_{10}{}^4 = 0.15\pm0.14$ that of Jet A1.

S

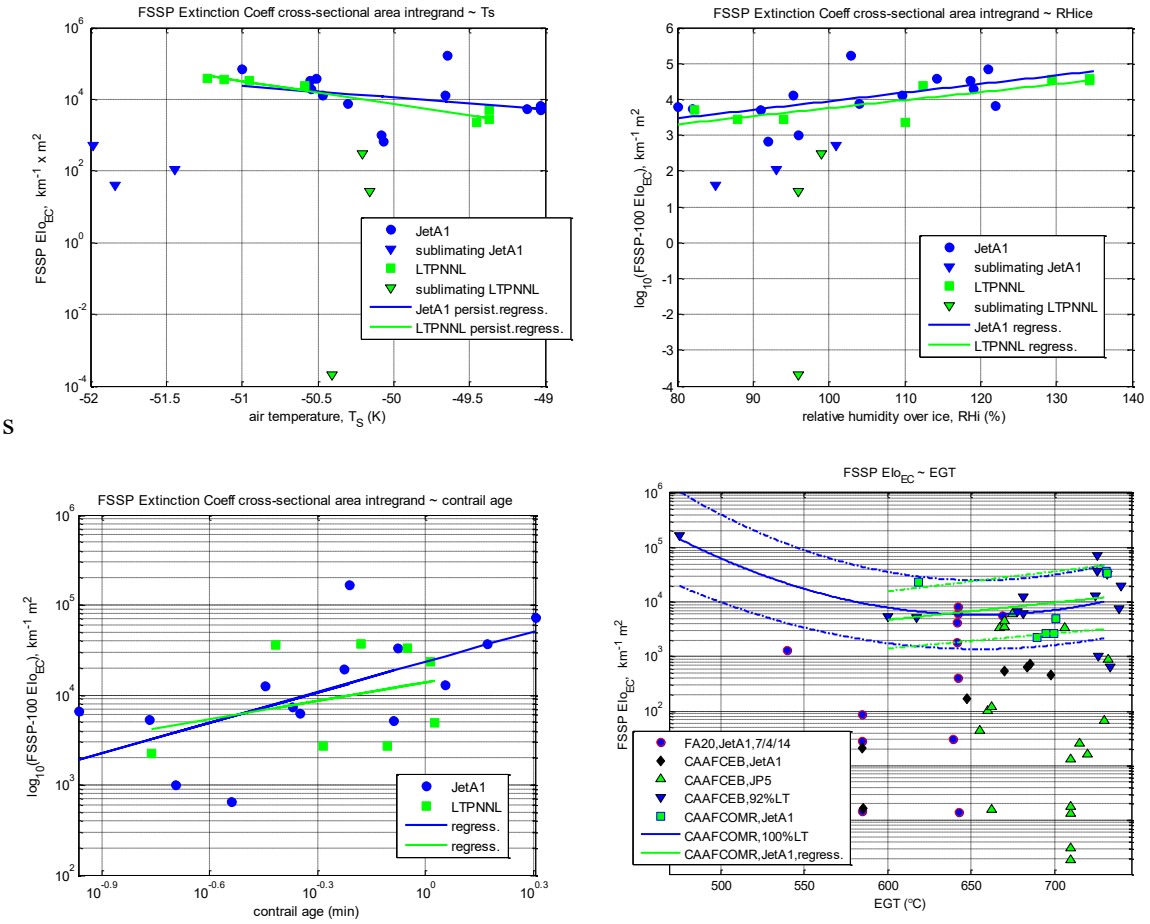

Figure 37 – functional characteristics for EIo, related to (*top left*) Ts, (*top right*) RHi, (*lower left*) contrail age, and (*lower right*) engine EGT.

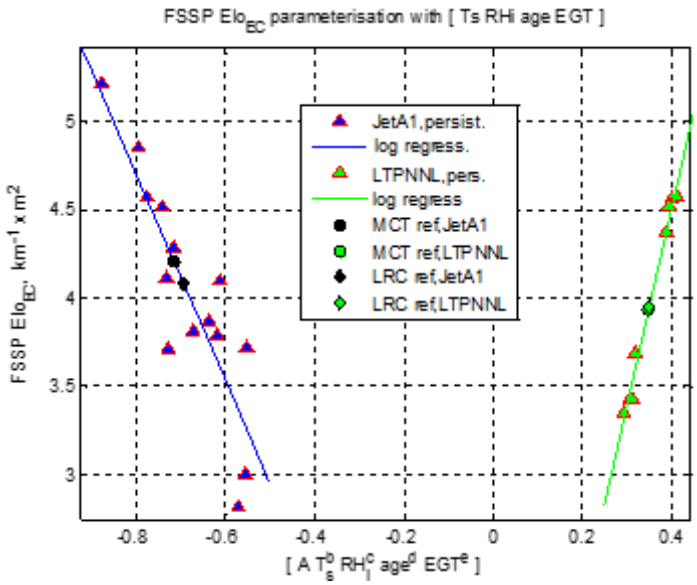

Figure 38 – power-law identifications for EIo, JetA1 and LTPNNL, with LRC and MCT reference conditions shown, for -50°C, ≈100%, 1 minute contrail age.

Classification: Unclass
Distribution: UNLIMITED

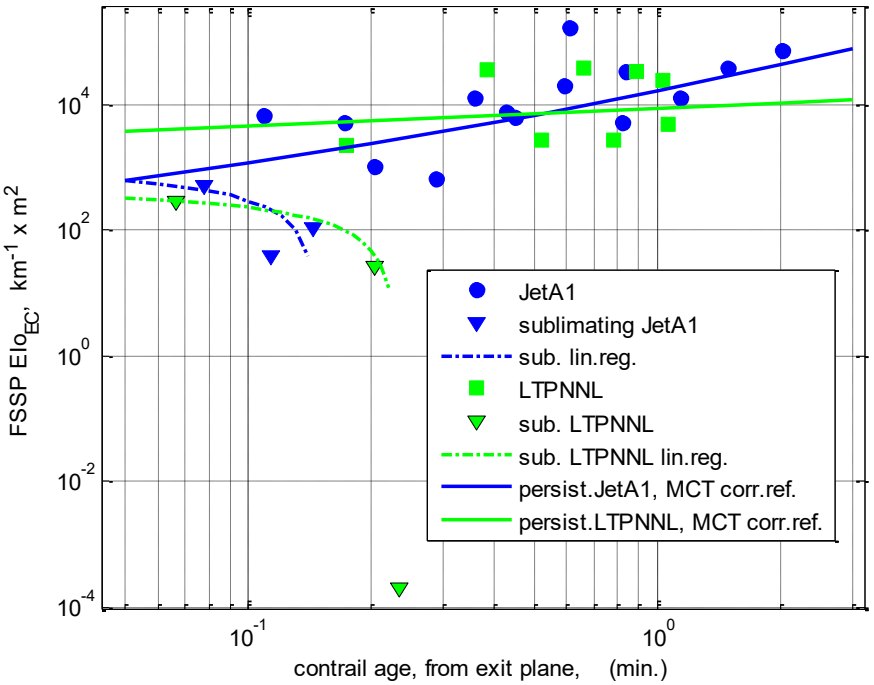

Figure 39 – corrected EIo data for MCT, (*solid blue line*) JetA1, (*solid green line*) LTPNNL.

4.8 Transmissivity, I/Io

4.8.1 Transmissivity, defined in this application as the ratio of the intensity of transmitted visible light, I, divided by the incident intensity of light, Io, *i.e.* I/Io. Conversely therefore, I/Io=1 represents zero obscurity, whilst I/Io=0 represents total obscurity, *i.e.* complete absorption and incident surface reflection of visible light. The minimum value of I/Io is concurrent with maximum obscurity. Conversely, it would be expected for sublimating contrails, that $\lim_{t\to\infty}$ (I/Io) = 1.

4.8.2 Under the influence of trailing vortex downwards induction, the initial contrail develops both vertically and laterally. Close to the aircraft centreline (in zero windshear), the initial vertical development is generally found to be deepest, resulting in the lowest transmissivity, or greatest obscurity, *i.e.* absorption plus incident surface reflection, in the zenithal direction. This is observed in the zenithal transmissivity examples of Figure 40 for JetA1 and Figure 41 for LTPNNL, both on the 12th February 2020 flight. I/Io at 0.3 min. age showed the negligible absorption effect (I/Io ≈ 1) in the sublimating state. Re-growth resulted in rapid growth of obscurity (I/Io ≈ 0.8 at 0.55 min. age).

4.8.3 For the LTPNNL contrail, an ice-mass contour cross-section is shown at 0.4 min. age, with horizontal and zenithal transmissivities at 0.4 min. age. It is seen that the contrail cross-section is slanted, typically indicative of interaction with background atmospheric vertical windshear in the lateral direction. Contrail horizontal and zenithal obscurity maxima were similar to each other, of magnitude I/Io ≈ 0.6, indicative of greater absorption near contrail generation, for LTPNNL.

4.8.4 Parametric plots of minimum X-sectional I/Io are shown in Figure 42. It is seen that these indicated greater obscurity with colder air, increasing humidity and contrail age. An apparent outlier appeared to be associated with low engine thrust (as it did with EIn).

Classification: Unclass
Distribution: UNLIMITED

Compound power-law identification is shown in Figure 43. Corrected I/Io regression lines, to the reference condition (as before) of MCT at Ts = -50°C, RHi ≈ 100%, contrail age of 1 min., are shown in Figure 44. It is seen that following contrail generation, maximum obscurity (*i.e.,* absorption and surface reflection) was greater for the LTPNNL contrail, but the obscuration rate of increase with age was greater for the JetA1 contrail, such that by 3 min. age, obscuration was twice that of LTPNNL.

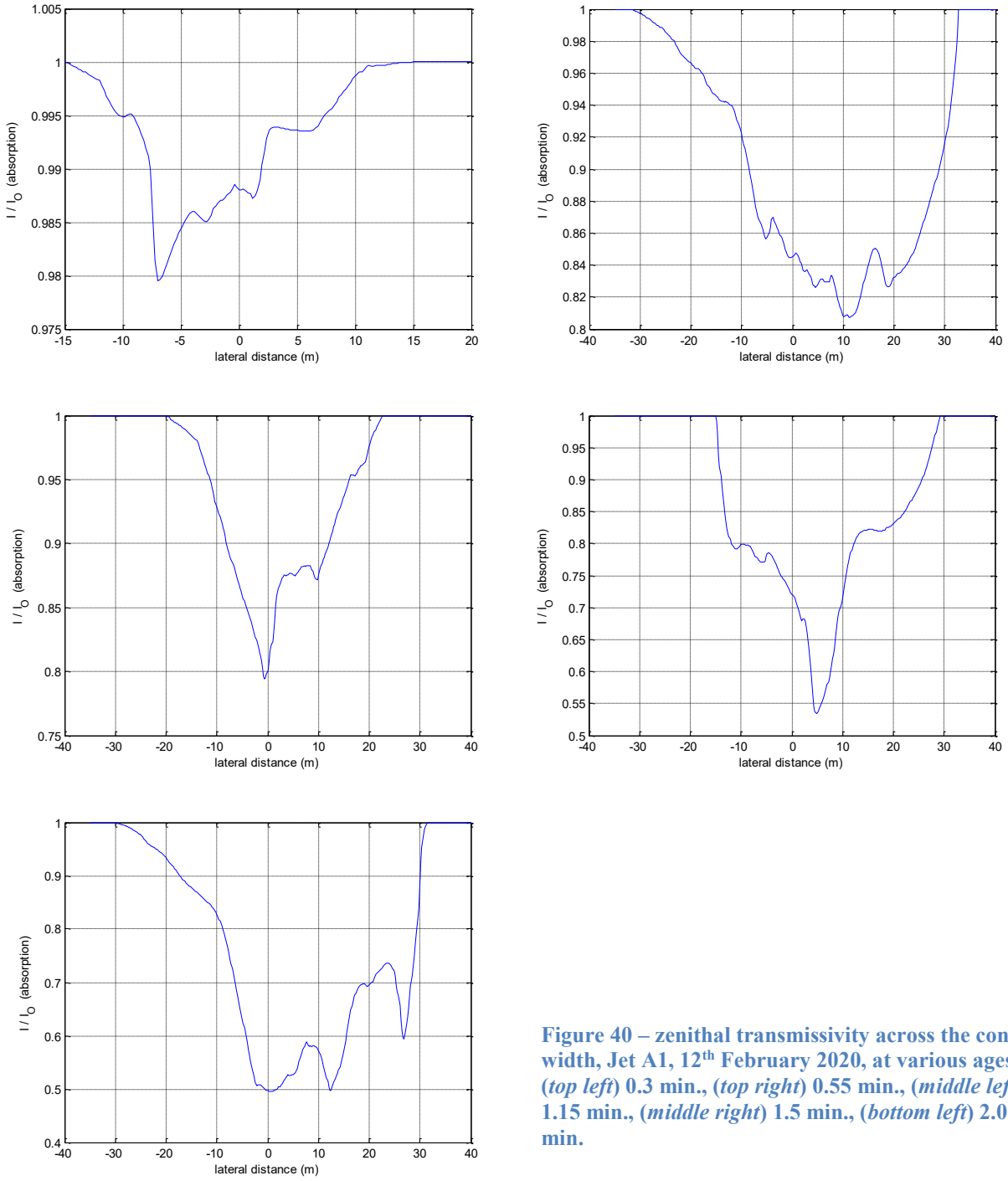

Figure 40 – zenithal transmissivity across the contrail width, Jet A1, 12th February 2020, at various ages: (*top left*) 0.3 min., (*top right*) 0.55 min., (*middle left*) 1.15 min., (*middle right*) 1.5 min., (*bottom left*) 2.0 min.

Classification: Unclass
Distribution: UNLIMITED

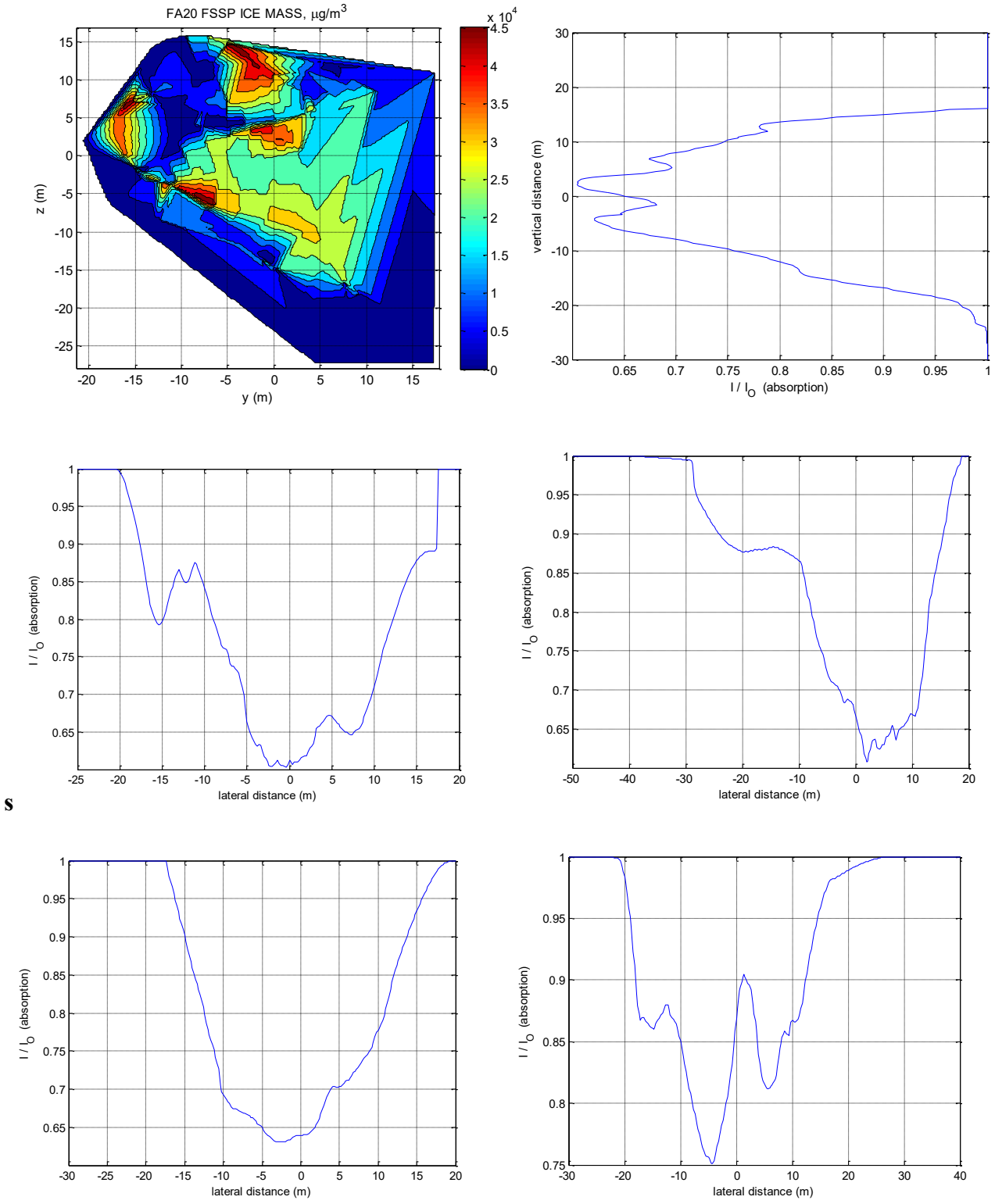

S

Figure 41 – contrail cross-sections at increasing age, lateral distribution of I/Io, LTPNNL, flight of 12th February 2020: (*top left*) ice-mass concentration at 0.4 min., (*top right*) horizon transmissivity, I/Io, 0.4 min., (*middle left*) zenithal I/Io, 0.4 min., (*middle right*) zenithal I/Io, 0.7 min., (*bottom left*) zenithal I/Io, 0.9 min., (*bottom right*) zenithal I/Io, 1.0 min. age.

Classification: Unclass
Distribution: UNLIMITED

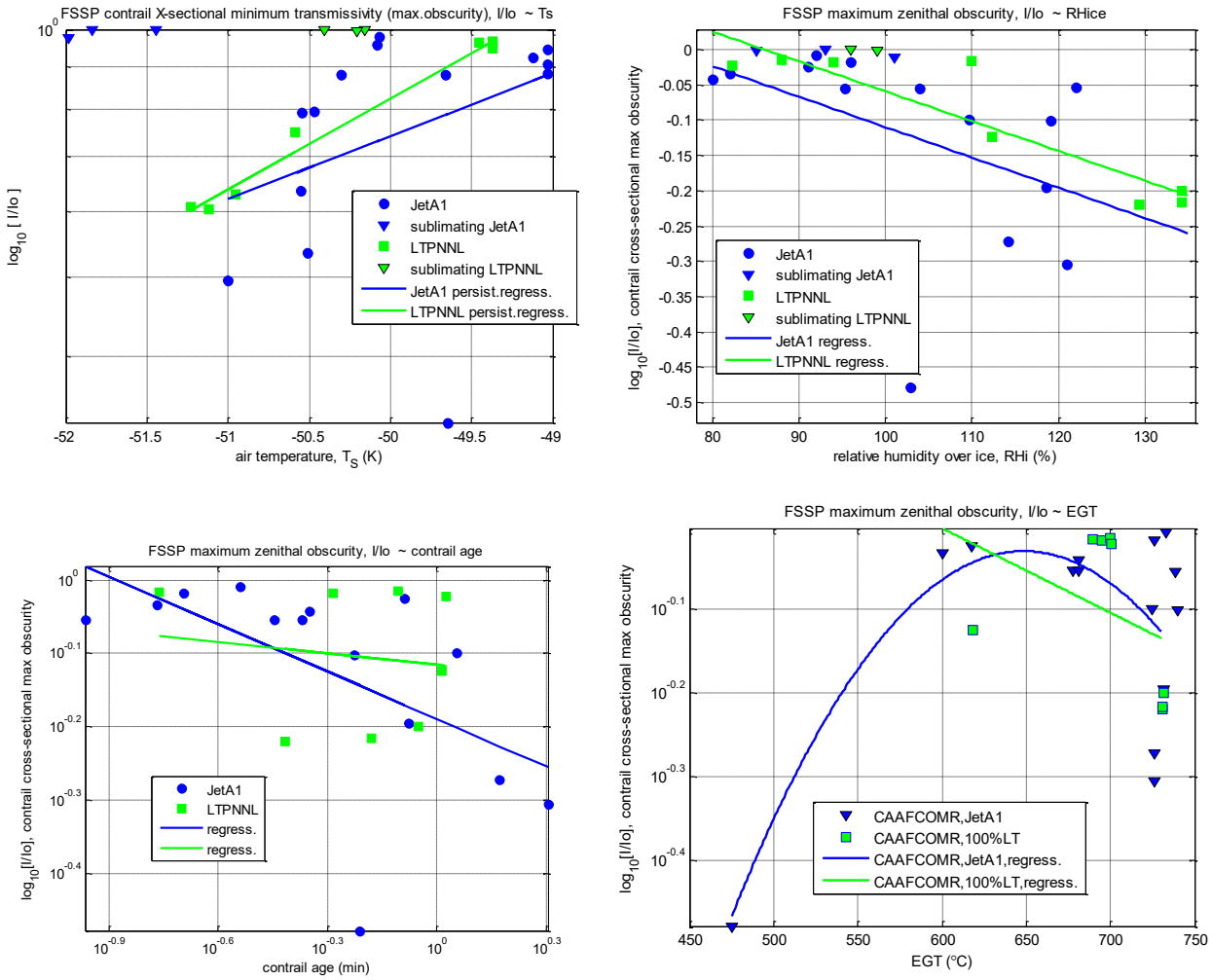

Figure 42 – contrail X-sectional minimum I/Io (maximum obscurity, *i.e.* absorption) univariate log plots against environmental, age and engine state parameters: (*top left*) Ts (°C), (*top right*) RHi (%), (*bottom left*) contrail age (min.), (*bottom right*) engine EGT (°C).

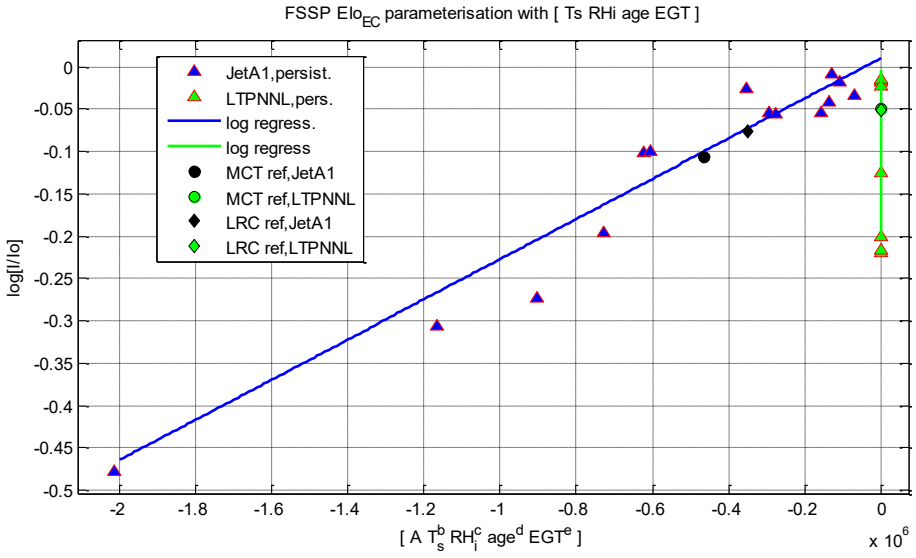

Figure 43 – power-law identification and reference condition [-50°C ≈100% 1 min.] corrected I/Io transmissivity (inverse obscurity) for reference engine thrust conditions of LRC and MCT.

Classification: Unclass
Distribution: UNLIMITED

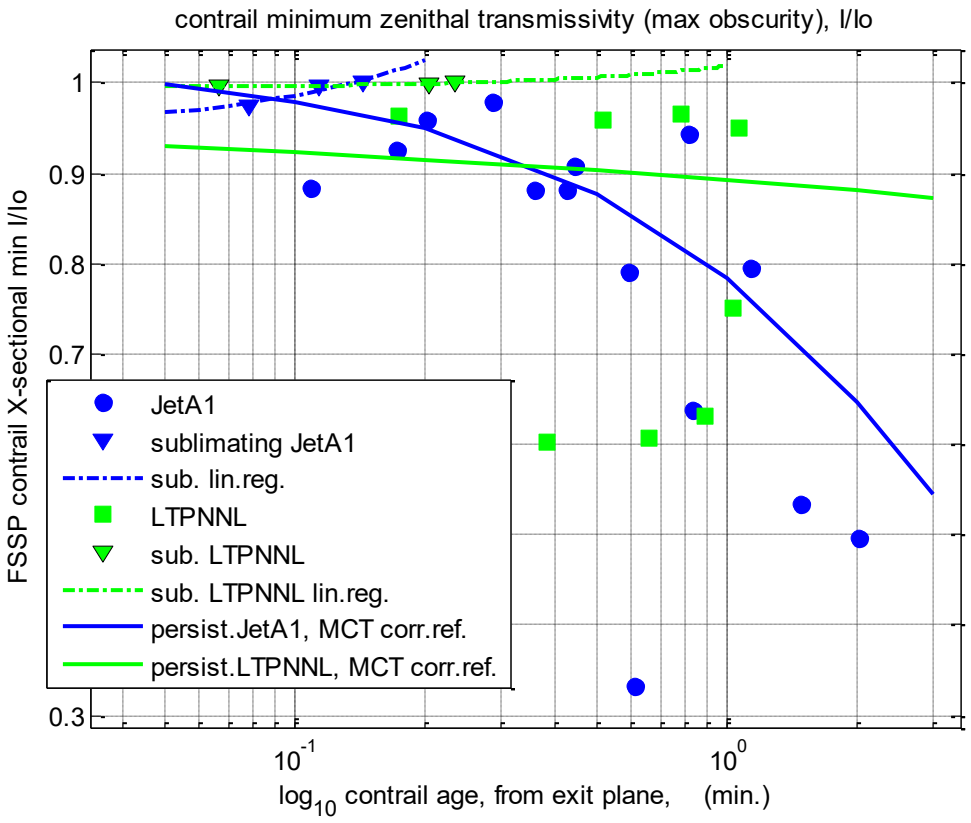

Figure 44 – data point plot of maximum I/Io transmissivity for each contrail X-section, together with regression curves for the corrected reference condition of Ts = -50°C, RHi ≈ 100%, 1 min. age and MCT engine power, (*solid blue line*) JetA1, (*solid green line*) 100% LTPNNL.

4.9 Overall activation of CN

4.9.1 A plot of FSSP-100 contrail ice particle EIn against CN 7610 volatile plus non-volatile CN EIn is presented in Figure 45, for present and previous NRC Falcon data. A least squares regression fit to the present persistent contrail data, combined for both fuels (Jet A1 and 100% LTPNNL), is included in the figure. This indicated a linear log-log association between CN EIn and FSSP EIn. It showed that the ratio [CN EIn]/[FSSP EIn] is greatest for the current project compared to recent projects, thus supportive of the observation of the most-persistent contrails being encountered in CAAFCOMR.

4.9.2 Also included is a 1:1 limit line, wherefore the FSSP EIn and CN EIn would be the same. Anticipating that the non-volatile fraction of total CN for LTPNNL would approach 1.0 (due to the absence of sulphur and aromatics), Figure 45 implied overall activations generally less than 100%. In turn, this has implied additional sizing information. Smallest ice particle sensing by the FSSP was >0.5 μm. Nominally smallest CN particle sizing was 10 nm. However plumbing calibration tests at ISA SL **[19]** indicated that the cut-off for the CN 7610 in the NRC CT-133 HAARC pod configuration was 22 nm. Therefore, any CN count implied a size of ≥22 nm. All CN data plotted in Figure 45 was obtained in contrail conditions. That FSSP EIn << CN EIn generally, was indicative of successful ice removal in the inlet, manifold and distribution plumbing in the HAARC pod heated interior and CN 7610 sensor.

Classification: Unclass
Distribution: UNLIMITED

4.9.3 Thus, that FSSP EIn < CN EIn for LTPNNL would be likely, principally attributed to the existence of an unknown number of smaller ice particle sizes below the FSSP-100 size detection threshold; for JetA1, in addition this would reflect the existence of many non-nucleating particles, including volatile particles of high purity (*e.g.*, **[3]** flight data implied an impure sulphate ice nucleation mode). This rationale was supported by the data of the 12th February 2020 flight, wherefore, the LTPNNL FSSP EIn approached the activation limit line with a value of $5.68_{10}{}^{14}/5.83_{10}{}^{14} = 0.975$ at an age of 0.9 min., implying that essentially all CN were nucleated ice particles > 0.5 μm in size. Furthermore, growth rates were rapid, 0.75 was achieved at an age of 0.4 min. Under similar conditions, the Jet A1 contrail had a maximum [CN EIn]/[FSSP EIn] value of 0.322, implying that 68% of CN registrations consisted of either ice particles ≤0.5 μm in size *or* non-nucleating particles, possibly the majority of volatile particles.

4.9.4 Included in Figure 45 is a plot of FSSP EIn / CN EIn activation ~ contrail age. Apart from the LTPNNL 12th February contrail, which achieved high activation early (0.4 min. age) as mentioned above, the regression line implied a progressive growth rate, as the ice particle percentage >0.5 μm increased with time.

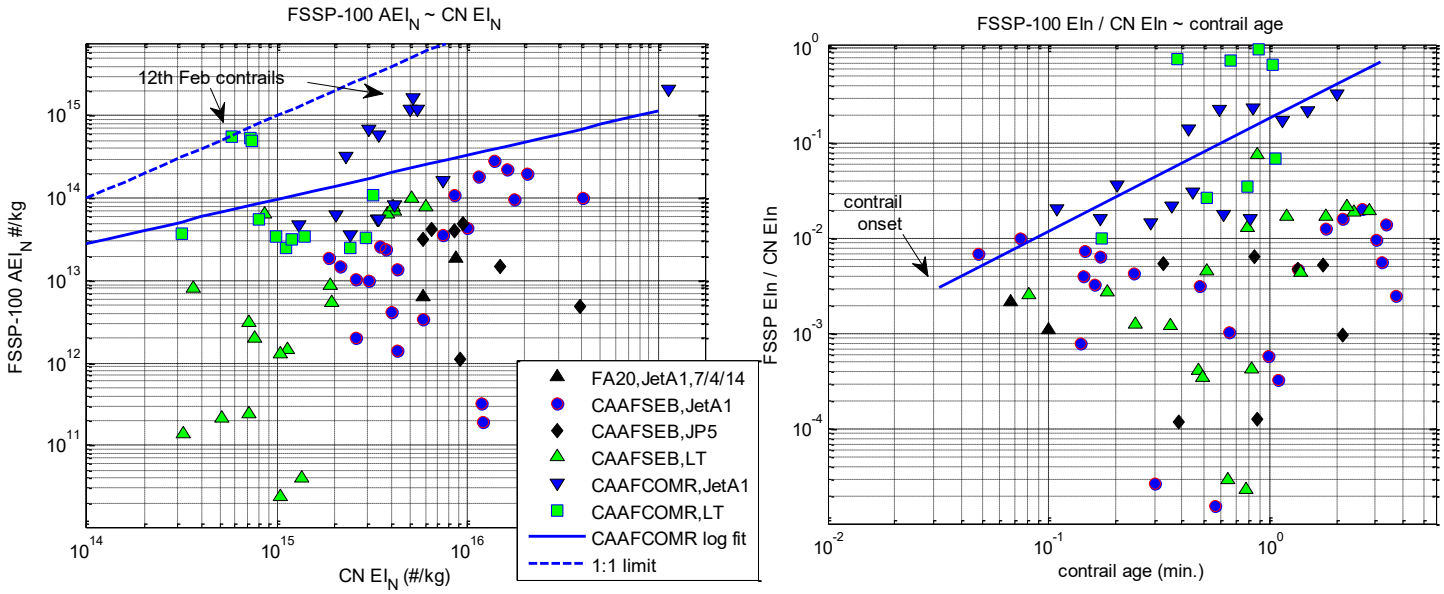

Figure 45 – cross-plots of contrail X-section FSSP EIn / CN EIn (activation) against (*left*) CN EIn, and (*right*) contrail age, for NRC Falcon 20 data form 2014 onwards.

4.9.5 To investigate this further, the activation ratio data [FSSP EIn]/[CN EIn] for each re-constructed contrail cross-section, without corrections for variations in atmospheric parameters, age, or engine state data, was plotted against FSSP EIn data, Figure 46. 1st order log-log regressions were conducted for the following fuels: JetA1 (excluding the low EGT point of present JetA1 data), 100% LTPNNL (adding the $[10^{10}\ 10^{-5}]$ point in order to pivot the data over several decades), and JP-5 (all data points, without addition). Three contrail classifications were approximately quantified by FSSP EIn, namely persistent, sublimating and invisible (the last guided by the observations of **[3]**). Several interesting characteristics were apparent in this presentation

- For all fuels, activation increased with increasing FSSP EIn – primarily caused by two effects, aggregated atmospheric effects (Ts, RHi but not ∂RH/∂z for the Falcon

Classification: Unclass
Distribution: UNLIMITED

because of the lack of downwards induction of condensate with age, due to the aircraft's warm trailing vortex cores) and contrail age;

- The regressed lapse rates of activation with FSSP EIn, for each of the three fuels, were similar (regressed lines approximately parallel);
- For individual data points: for 100% LTPNNL data, ≈100% overall sensed activation (*i.e.* above the FSSP size sensing threshold) of sensed CN (*i.e.* above the cut-off threshold of 22 nano-m) was achieved early in contrail age, as discussed earlier, likely supporting the expectation of a non-volatile (*nv*) fraction of ≈0, given that the fuel had neither sulphur nor aromatics;
- In the similar atmospheric conditions, it was probable that maximum activation was likewise achieved for Jet A1, *albeit* at a later contrail age because of slower initial growth rate; the overall activation figure of ≈30% as achieved, would possibly imply a non-nucleating *nv* fraction of ≈0.3;
- It is unlikely that maximum activation was achieved in the JP-5 data-set **[4]**;
- For any particular FSSP EIn value (principally, the same [Ts RHi] atmospheric state), the 100% LTPNNL and JetA1 regression lines exhibited an approximately constant offset of 0.8±0.02, likewise, between JP-5 and 100% LTPNNL regression lines, there was an approximately constant offset of 0.88±0.02.

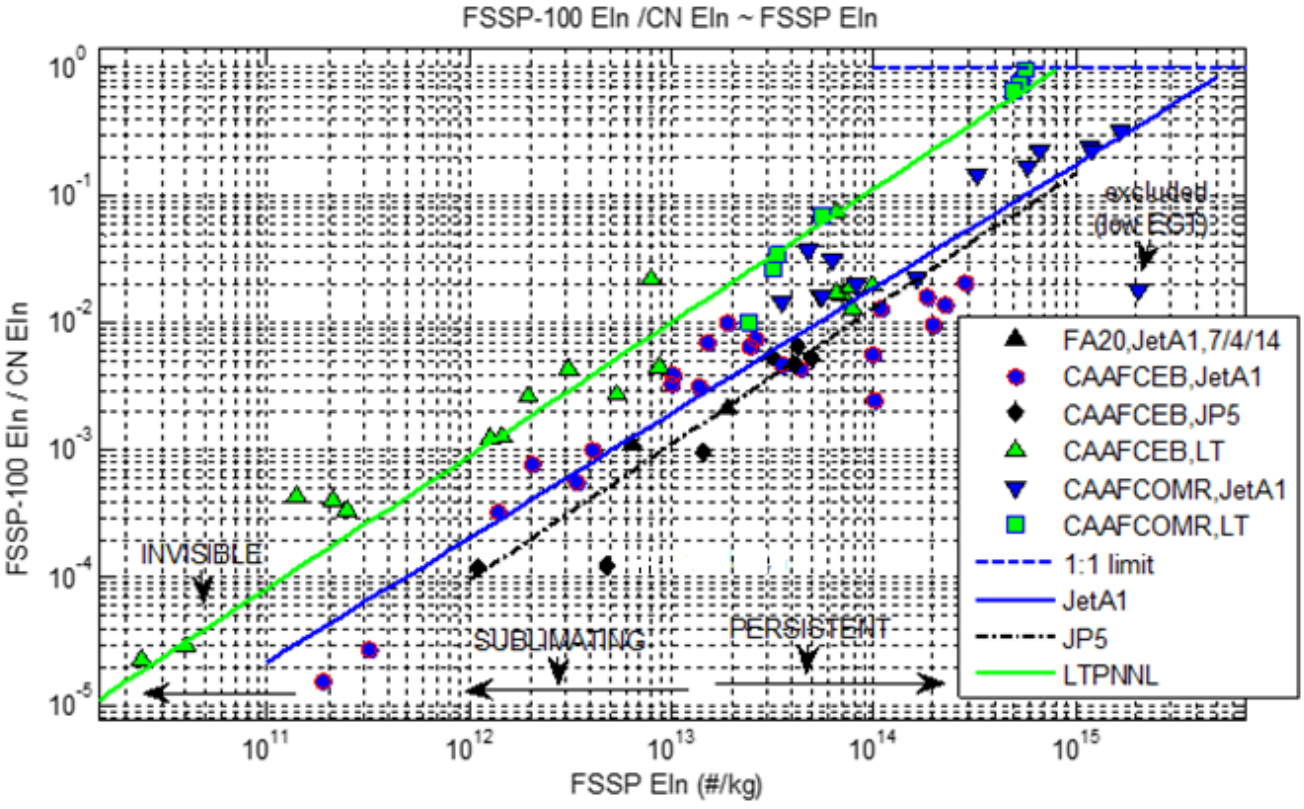

Figure 46 – combined plot of activation, []/[] against FSSP EIn for contrail X-sectional EIn data, uncorrected for atmospheric, age or engine state variations (except the low EGT point of CAAFCOMR JetA1 data has been excluded).

Classification: Unclass
Distribution: UNLIMITED

4.9.6 To explore an analytical basis for the offsets between different fuels, consider the following analysis, under the assumption that ice nucleation fractions were also approximated by the non-volatile (*nv*) fractions of PM. Within experimental error, the 1st order log-log regressions in Figure 46 resulted in similar slopes, *m*, but different intercepts for each fuel type. Consider Jet A1, 100% LTPNNL and JP-5 (the NAJCP 'A-3' fuel, **[12]**). Conduct an initial, comparative investigation between 100% LTPNNL and Jet A1, as follows

$$log\left[\frac{EIn_{FSSP_{LT}}}{EIn_{CN_{LT}}}\right] = m\ log[EIn_{FSSP}] + c_{LT}\ \text{, for 100\% LTPNNL} \quad (1)$$

$$log\left[\frac{EIn_{FSSP_{JA}}}{EIn_{CN_{JA}}}\right] = m\ log[EIn_{FSSP}] + c_{JA}\ \text{, for Jet A1} \quad (2)$$

For Jet A1, break-out EIn_{CN} into the *nv* fraction, thence

eq.(2) becomes $$log\left[\frac{EIn_{FSSP_{JA}}}{EIn_{CN_{JAnv}}} x \frac{EIn_{CN_{JAnv}}}{EIn_{CN_{JA}}}\right] = m\ log[EIn_{FSSP}] + c_{JA} \quad (3)$$

i.e., $$log\left[\frac{EIn_{FSSP_{JA}}}{EIn_{CN_{JAnv}}}\right] + log\left[\frac{EIn_{CN_{JAnv}}}{EIn_{CN_{JA}}}\right] = m\ log[EIn_{FSSP}] + c_{LJAT} \quad (4),$$

so that $$log\left[\frac{EIn_{FSSP_{JA}}}{EIn_{CN_{JAnv}}}\right] = m\ log[EIn_{FSSP}] + c_{JA} - log\left[\frac{EIn_{CN_{JAnv}}}{EIn_{CN_{JA}}}\right] \quad (5)$$

comparing to 100% LTPNNL, for a similar range of EIn_{FSSP}, to which the linearized slope *m* applied,

eq.(1) becomes $$m\ log[EIn_{FSSP}] = log\left[\frac{EIn_{FSSP_{LT}}}{EIn_{CN_{LT}}}\right] - c_{LT} \quad (6)$$

substituting eq.(6) in (5),

$$log\left[\frac{EIn_{FSSP_{JA}}}{EIn_{CN_{JAnv}}}\right] = log\left[\frac{EIn_{FSSP_{LT}}}{EIn_{CN_{LT}}}\right] - c_{LT} + c_{JA} - log\left[\frac{EIn_{CN_{JAnv}}}{EIn_{CN_{JA}}}\right] \quad (7)$$

Therefore, under the condition that

$$c_{JA} - c_{LT} = log\left[\frac{EIn_{CN_{JAnv}}}{EIn_{CN_{JA}}}\right] \quad (8)$$

Then eq.(7) becomes, $$log\left[\frac{EIn_{FSSP_{JA}}}{EIn_{CN_{JAnv}}}\right] = log\left[\frac{EIn_{FSSP_{LT}}}{EIn_{CN_{LT}}}\right] \quad (9)$$

And, with the LHS of eq.(9) now containing the *nv* fraction for CN, *i.e.* $EIn_{CN_{JAnv}} = \frac{EIn_{CN_{JAnv}}}{EIn_{CN_{JA}}}$ x $EIn_{CN_{JA}}$, there will be an overlay of regression lines for Jet A1 and 100% LTPNNL. Figure 46 showed that on average $c_{JA} - c_{LT}$= -0.7 (in log format, *i.e.* part of a log-decade). Solving eq.(8) for this value, *i.e.* $log\left[\frac{EIn_{CN_{JAnv}}}{EIn_{CN_{JA}}}\right] = -0.7$, an *nv* fraction $\frac{EIn_{CN_{JAnv}}}{EIn_{CN_{JA}}} = 0.2$, for which $log\left[\frac{EIn_{FSSP_{JA}}}{EIn_{CN_{JAnv}}}\right]$ has been plotted in Figure 47. It is seen that the above method successfully overlaid data points and 1st order log-log regression lines, for Jet A1 with CN*nv*/CN=0.2 and JP-5 ('A-3' fuel of the NAJCP, **[12]**) with CN*nv*/CN=0.12.

Classification: Unclass
Distribution: UNLIMITED

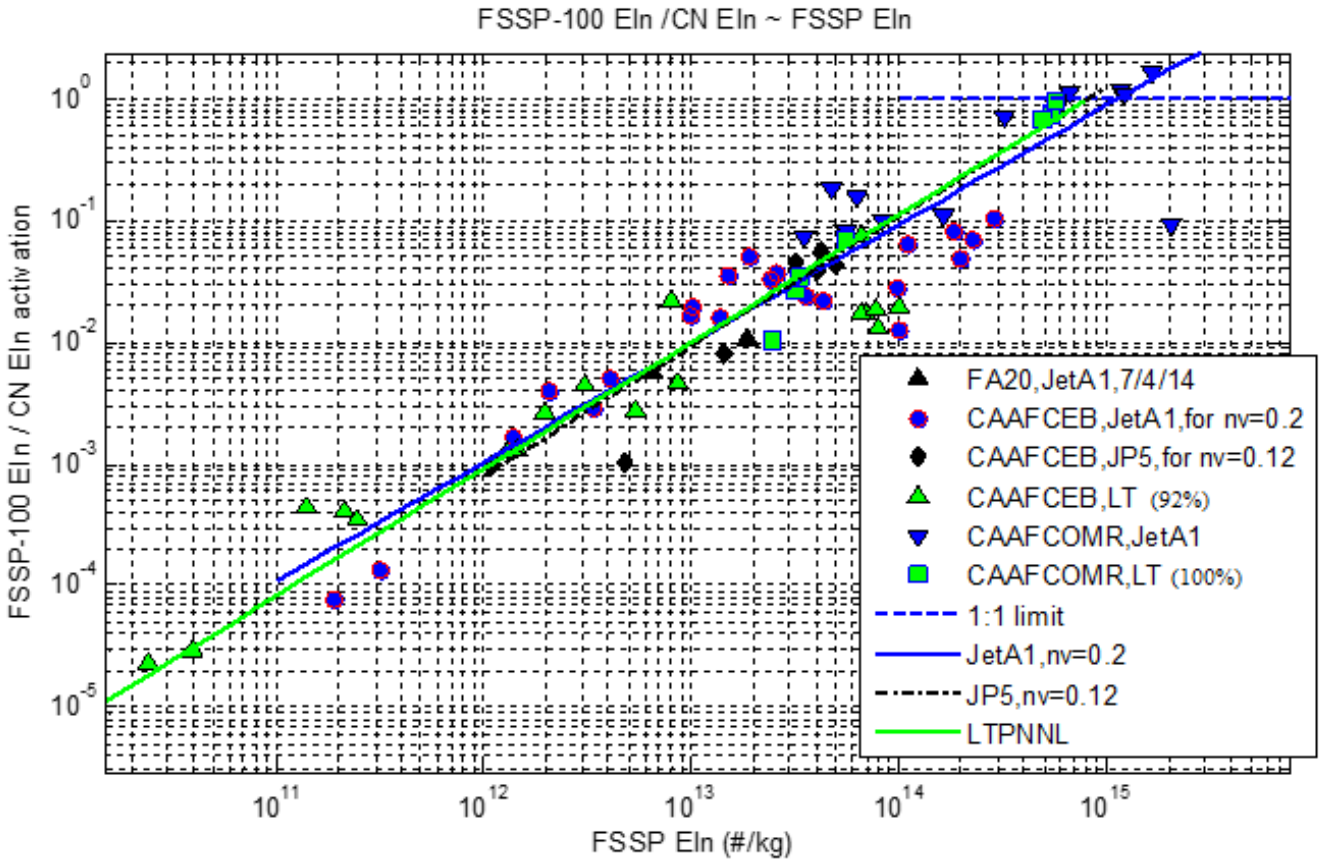

Figure 47 – data points & 1st order log-log regression lines for: (*green data points & solid green line*) [EIn_FSSP/EIn_CN] plot for 100% LTPNNL, (*blue data points & solid blue line*) [EIn_FSSP/EIn_CNnv] for Jet A1 with CNnv/CN=0.2, (*black data points & solid black line*) [EIn_FSSP/EIn_CNnv] for JP-5 ('A-3' fuel of [12]) with CNnv/CN= 0.12.

4.9.7 The *nv* fraction, thus derived, was useful for additional purposes, in comparing emission characteristics between 100% LTPNNL and Jet A1. Table 4 reported a CN EIn mean ratio of 0.13 between the fuels. Under the assumption that *nv*≈1.0 for 100% LTPNNL as rationalised earlier, this, together with the Jet A1 *nv* fraction derived above (essentially *nv* ≡ BC), implied that for particles >22 nano-m cut-off size, the ratio of BC EIn between 100% LTPNNL and Jet A1 was a mean value of approximately 0.13/0.2 = 0.65 at MCT. The BC EIm mean value comparison between the fuels was measured as approximately 0.13, substantially lower, which was therefore indicative of smaller-sized BC particles in the case of 100% LTPNNL, a spherical size comparison of $\sqrt[3]{\left[\frac{0.13}{0.65}\right]} = 0.58$, or the volume-mean size of LTPNNL BC particles were approximately 50% smaller than Jet A1 BC particles.

Classification: Unclass
Distribution: UNLIMITED

4.10 Contrail and emission comparison, Jet A1 and 100% LTPNNL

4.10.1 In summary, within the limitations of flight instrumentation, the 100% LTPNNL contrails were thicker in all measured characteristics at generation, *c.f.* Jet A1. The essential difference appeared to relate to the markedly greater initial ice particle growth rates, to be rapidly sensed by the FSSP-100, with a size threshold > 0.5 μm, at least. Assisting in the higher initial growth rates would likely have been the greater production of water vapour by 100% LTPNNL combustion, with total hydrogen content 15.3% *c.f.* Jet A1 at 13.7%.

4.10.2 However, following generation, LTPNNL contrails grew at slower rates than those of Jet A1. At and beyond 1 min. age, the Jet A1 contrails were thicker, progressively moreso with increasing age. This is reflected in the comparisons in Table 6. Included are uncertainties – for calculated parameters, these have been expressed as a range derived from $[\text{mean}\pm 1\sigma]_{\text{LTPNNL}}$ / $[\text{mean}+1\sigma]_{\text{JetA1}}$, in order to include the ratio of mean values.

4.10.3 These uncertainties were derived from the linearisation scatter of product-power-law modelling, for the variation of contrail parameters, with atmospheric air temperature, approximate RHi, engine thermodynamic state and contrail age. The LTPNNL linearisation, in all cases, resulted in less scatter than Jet A1. It was hypothesised that this reflected the lack of volatile PM from the 100% LTPNNL fuel. Volatile PM could be expected to have greater variability and non-linearity of physical processes in turbulent jet/wake-flow temperature, pressure and shear gradients and magnitudes.

4.10.4 Uncertainties were large in particular for ice-mass EIm and ice particle size, the latter reflecting the dynamics of sublimation and re-growth in RH pooling.

4.10.5 Contrail data was measured over the wake age range of 0.07-2.2 minutes for Jet A1 and 0.05-1.2 minute, for 100% LTPNNL. In Table 6, parameters have been extrapolated to contrail ages of 3 minutes. For LTPNNL, following generation, contrail parameters changed relatively slowly with age, whereas for Jet A1, parameters increased more rapidly with age. Although extrapolated in age, they were interpolated points in the modelled product-power-law formulation.

4.10.6 Additional flight measurements, covering a greater age range, 1 to 10 minutes, would enhance the understanding of parametric trends, given that the comparative benefits from 100% LTPNNL, including optical properties, appeared to increase with contrail age.

Classification: Unclass
Distribution: UNLIMITED

Table 6 – comparison of contrail characteristics from 100% LTPNNL and Jet A1, NRC Falcon 20 with GE CF700 engines, shortly following generation and progressively ageing, measured to 2 min. extrapolated to 3 min. age.

Contrail & or emission parameter	**MCT engine thrust condition; atmospheric conditions Ts = -50°C; RHi ≈ 100%**		
	100% LTPNNL to JetA1 ratio of parameter [mean±1σ] for each fuel		
	Near generation, t=0.05 sec	**At 1 min. age**	**Extrapolated to 3 min. age**
Contrail			
Ice particle EIn	**1.45**(-0.71/+1.35)	**0.26**(-0.14/+0.27)	**0.13**(-0.07/+0.15)
Spherical ice-mass EIm	**1.6** kg/kg, LTPNNL **0.2** kg/kg, Jet A1, inaccurate, due to initial sublimation & regrowth	**0.38**(-0.24/+0.64)	**0.10**(-0.06/+0.18)
EIo, integrated extinction coefficient	**8.0**±1.9	**0.7**±0.5	**0.15**±0.14
Maximum zenithal obscurity	**1.1**±0.25	**0.89**+0.15	**0.64**±0.14
Median MED, for each fuel	**4.5**±0.2 LTPNNL **2.5**±1.0 Jet A1, inaccurate, due to initial sublimation & regrowth	**3.9**±0.3 LTPNNL **3.4**±0.8 Jet A1	**3.5**±0.3 LTPNNL **4.0**±0.5 Jet A1
Emission	**Combined**		
CN EIn (>22nano-m)	**0.13**(-0.06/+0.15)		
BC EIm	**0.17**(-0.10/+0.46)		
BC particle size ratio	**0.5**±0.1 (LTPNNL to Jet A1)		
Activation max. (ice nucleation)	97.5% for LTPNNL; 32% for Jet A1		
Approximate *non-volatile* fraction	Assumed 100% for LTPNNL; comparatively 20% for Jet A1; 12% for JP-5		

Classification: Unclass
Distribution: UNLIMITED

5. CONCLUSIONS

5.1.1 As part of project CAAFCOMR, sublimating and persistent contrails have been measured inflight for petroleum and biofuels, namely Jet A1 and 100% LTPNNL ATJ-derived SPK, respectively, the latter containing no aromatics nor sulphur. Comparative persistent contrails were obtained from the NRC Falcon 20 research jet, with the engines operating at Long Range Cruise (LRC) and Maximum Continuous Thrust (MCT) settings. The latter is more applicable to jet transport aircraft operations, generally.

5.1.2 Contrail characteristics, such as EIn (for sizes > 0.5 μm) and ice particle size, median MED, exhibited strong dependencies upon air temperature and relative humidity, and noticeably for Jet A1, a dependency upon core gas temperature of the engines (*i.e.* thrust). For the persistent contrails, all characteristics showed growth with age. Product power-law modelling of all studied contrail characteristics, using a parametric vector of dependency (four variable, Ts, RHi, engine gas temperature, contrail age) was robust, enabling interpolative corrections in values of EIn, EIm, median MED, and the optical effects important for radiation forcing studies, namely extinction coefficient 'emission index,' EIo, and local zenithal obscurity, to be derived for a reference contrail condition of -50°C, ≈100%RHi, MCT thrust and increasing contrail age. The corrections had low scatter for 100% LTPNNL, but higher scatter for Jet A1. It was hypothesised that this could have been related to ice nucleation and growth processes in the presence of prevalent volatile particulate matter emissions from the latter, compared to the likely elimination of volatile PM emissions from the former (without aromatics nor sulphur).

5.1.3 When studied against contrail age for the reference contrail formation conditions, the following comparative observations were drawn. Shortly (0.03-0.05 minutes) after generation, the 100% LTPNNL contrail exhibited substantially greater (45% to possibly several hundred percent, depending upon the parameter) EIn, EIm, ice particle size (median MED), EIo and local obscurity, than the Jet A1 contrail.

5.1.4 Thereafter, the persistent contrails grew with increasing age. Ice particle number concentrations were calculated to be of the order of 2000 #/cc. However contrail parametric growth rates for 100% LTPNNL were significantly lower than those for Jet A1, while ice particle size reduced with contrail age (whereas, it increased with age, for Jet A1). Extrapolated to 3 minutes contrail age, and margined by a $\pm 1\sigma$ uncertainty, the 100% LTPNNL contrail parameters were between 71-96% lower than those of Jet A1, in ice particle number, mass and overall optical thickness (extinction). Maximum zenithal obscurity was 20-50% lower, and median ice particle size was 0-30% lower.

5.1.5 With similar uncertainty margining, overall PM emissions from LTPNNL were 72-93% lower in number, soot mass was 37-93% lower, soot particle number a mean 35% lower and soot mean size approximately 50% lower.

5.1.6 Although contrail optical extinction was successfully integrated to derive overall optical thickness emission factors, the line-of-flight spatiotemporal variability was high. Furthermore, spatiotemporal gradients and magnitudes of line-of-flight relative humidity variations were likewise large. Optical thickness data highlighted the optical thinning of LTPNNL contrails, *c.f.* Jet A1 contrails. Radiative thermodynamic analyses are needed to quantify the comparative heat entrapment effects in the infra-red spectral range of solar radiation, possibly including the localised radiative effects across the contrail cross-sectional ice particle parametric variations.

Classification: Unclass
Distribution: UNLIMITED

ACKNOWLEDGEMENTS

Project CAAFCOMR, flight research of contrails with 100% ATJ SPK fuel, without aromatics, acknowledges gratefully the sponsorship of Environment & Climate Change Canada, Transport Canada, LanzaTech and the National Research Council Canada.

REFERENCES

1. Brown, A.P., Bastian, M., Alavi, S., Wasey, M., "FLIGHT RESEARCH REPORT: PROJECTS AEAFFR, CAAFER AND NASA ACCESS II JET TRANSPORT EMISSIONS MEASUREMENTS," NRC LTR-FRL-2015-0054, March 2015.
2. Brown, A.P., Bastian, M. and Smallwood, G., "Aviation Emissions Index Derivation Methodologies from Flight Data, including Black Carbon and Aerosols," AIAA 40th Atmospheric and Space Environments Conference, New Orleans, 25-29 June 2012, AIAA-2012-2926.
3. Brown, A.P., Bastian, M., "Civil Aviation Alternate Fuels Contrails and Emissions Research (GARDN CAAFCER) – Contrails Analysis," NRC LTR-FRL-2018-0014, February 2018.
4. Brown, A.P., Bastian, M. and Canteenwalla, P., "Civil Aviation Alternate Fuels Contrails and Emissions from high-Blend Biofuels (CAAFCEB) – Contrails Analysis," LTR-FRL-2018-0029, March 2018, NRC Canada.
5. Environment Branch of the International Civil Aviation Organisation, "ICAO Environmental Report 2016, Aviation and Climate Change."
6. Korolev, A, Shashkov, A. and Barker, H., "Calibrations and Performance of the Airborne Cloud Extinction Probe," J.Atmos. & Ocean Tech., V0l.31, *pp* 326-344, February 2014. DOI10.1175/JTECH-D-13-00020.1.
7. Anon, "Model 7610 Condensation Particle Counter Instruction Manual," Particle Measuring Systems P/N 1933780 Rev B, Boulder, CO, March 1995.
8. Brown, A.P., Bastian, M. Pryor, M. and Smallwood, G., "Flight Test Report:- Flight Emissions from 100% Drop-In Biofuel," ISSUE 4, 4th October 2013.
9. Brown, A.P., Bastian, M, Smallwood, G., (NRC), Rideout, G., Connolly, T. and Radke, J., "FLIGHT TEST REPORT:- PERD AEEM DATA ACQUISITION #9:- PARTICULATES, FLASK, NOx SAMPLING FLIGHT, WAKE CROSSING," 20th November 2011.

10. Poitras, P., “NRC Biofuel Flight Program – Alcohol to Jet Fuel Sample Testing,” QETE 19100-1 (H016517), 17 May 2018, Quality Engineering Test Establishment, DND.
11. LTPNNL fuel analysis test report.
12. Chan, T.W., Canteenwalla, P., Chishty, W. W., “GT2017-63131, Characterisation of Fuel Composition and Altitude Impact on Gaseous and Particle Emissions from a Turbojet Engine,” Proceedings of ASME Turbo Expo 2017, , GT2017, 26-30 June 2017, Charlotte, NC, USA.
13. Miake-Lye, R. C., *et al*, “SO_x oxidation and volatile aerosol in aircraft exhaust plumes depend on fuel sulphur content, G.R.L., Vol.25, No.19, pp 1670-1680, 15 May 1998.
14. Karcher, B., “The importance of contrail ice formation for mitigating the climate impact of aviation,” Journal of Geophysical Research: Atmospheres, 10.1002/2015JD024696, 2016, *pp* 3497-3505.
15. Moore, R.H. *et al*, “Biofuel blending reduces particle emissions from aircraft engines at cruise conditions,” Nature, doi:10.1038/nature21420, 2017.
16. Poitras, P., “NRC Biofuel Flight Program Sample Testing,” QETE 19100-1 (H001917), 21 July 2017, Quality Engineering Test Establishment, DND.
17. P. Jeßberger, C. Voigt, U. Schumann, I. Sölch, H. Schlager, S. Kaufmann, A. Petzold1, D. Schäuble, and J.-F. Gayet, “Aircraft type influence on contrail properties,” Atmos. Chem. Phys., 13, 11965–11984, 2013 www.atmos-chem-phys.net/13/11965/2013/ doi:10.5194/acp-13-11965-2013.
18. Poitras, P., “NRC Biofuel Flight Program – Alcohol to Jet Fuel Sample Testing,” QETE 19100-1 (H016517), 17 May 2018, Quality Engineering Test Establishment, DND.
19. Olfert, J., “Calibration of Particle Counters on the NRC Flight Research Laboratory T-33 Aircraft,” Argonaut Scientific, March 2020.
20. Nichman, L., *et al*, “Intercomparison study and optical asphericity measurements of small ice particles in the CERN CLOUD experiment,” Atmos. Meas. Tech., 10, 3231–3248, 2017, https://doi.org/10.5194/amt-10-3231-2017